KU LEUVEN

ARENBERG DOCTORAL SCHOOL
Faculty of Engineering Science

Experimental analysis of the dynamic characteristics and lubricant film of a ball bearing under combined static and dynamic load

William Jacobs

Dissertation presented in partial
fulfilment of the requirements for the
degree of Doctor in Engineering
Science

May 2014

Experimental analysis of the dynamic characteristics and lubricant film of a ball bearing under combined static and dynamic load

William JACOBS

Supervisory Committee:
Prof. dr. ir. L. Froyen, chair
Prof. dr. ir. D. Moens, supervisor
Prof. dr. ir. P. Sas, co-supervisor
Prof. dr. ir. R. Boonen
Prof. dr. ir. D. Vandepitte
Prof. dr. ir. G. De Roeck
Prof. dr. ir. P. De Baets
(Ghent University)
Dr. ir. H. Van der Auweraer
(LMS International)

Dissertation presented in partial
fulfilment of the requirements for
the degree of Doctor
in Engineering Science

May 2014

Celestijnenlaan 300, B-3001 Heverlee (Belgium)

D/2014/7515/57
ISBN 978-94-6018-833-6

Acknowledgement

Looking back on the last five years of my life, conducting this doctoral study took me on a fascinating journey through the world of academic research. Along the way, I was supported by many enthusiastic people, which I gratefully acknowledge.

First of all, I wish to express my sincere gratitude to my supervisors, Prof. David Moens and Prof. Paul Sas. Throughout the study, David and Paul have given me invaluable guidance, criticism, suggestions and encouragement. Thank you for creating a pleasant work environment, for giving me the freedom to follow my interests and for offering different opportunities to attend conferences and trainings.

I would like to thank the members of the assessor committee, Prof. Dirk Vandepitte, Prof. René Boonen and Prof. Guido De Roeck, for providing valuable feedback during the course of the study. Together with the other members of the jury, Prof. Patrick De Baets and Dr. Herman Van der Auweraer, whose comments have much improved the manuscript. Thank you Prof. Ludo Froyen for chairing the defence.

Financial support was provided by the Agency for Innovation by Science and Technology (IWT). This support allowed building a test rig and conducting the research.

The Department of Mechanical Engineering is driven by an interesting group of highly qualified people. I am especially grateful that some of them became good friends over the years. I will treasure the memories of the cycling trips, lunch breaks, MOD breakfast meetings, PMA weekends and so much more. I thank my office buddies, Brecht, Daniele, Jan, Tommaso and Jasper, for the countless entertaining moments that we shared.

I would like to express my gratitude to the staff of the department, in particular to Lieve, Karin, Regine, Jan, Dirk, Eddy, Hans and Jean-Pierre. On many

occasions, their assistance helped me along the way. Also special thanks to Rudy for his assistance during SEM analyses.

During the design of the test rig, I could count on the expertise of Prof. René Boonen, Dr. Filip De Coninck, Dr. David Vaes and Dr. Tobias Waumans. Their advice was crucial to the development of the rig. René, I truly admire your clear and broad view on the various aspects of mechanics. Thank you for the fruitful and ever agreeable collaboration.

The study was shaped during lively discussions with several experts in the field. It has been a true pleasure working with Prof. Farid Al-Bender, Prof. Eric Van den Bulck, Dr. Jan Peirs, Prof. Robert Randall, Dr. Fábio Nonato, Prof. Katia Cavalca, Ben Marrant, Kurt Engelen, Dr. Kris Smolders, Dr. Steven Devos, Dr. Walter Driesen, Dr. Björn Verrelst, Prof. Jürgen Gegner and Wolfgang Nierlich. Thank you all.

Finally, I am very grateful to my parents and friends. To my parents, for giving me all the opportunities, support and love. To my friends, for regularly providing a much appreciated distraction from work. You were all genuinely great along this journey.

William
May 2014

Abstract

Being particularly critical components, the serviceability of rolling element bearings is usually essential for the machine's operation. They have been the subject of research for more than a 100 years. The work of this manuscript investigates two aspects of rolling element bearings. Firstly, the dynamic behaviour of a rolling element bearing is analysed. The study emphasises the influence of the lubricant film on the bearing dynamics. Secondly, the lifetime of the bearing is analysed. The study discusses the influence of external dynamic loads on the lubricant film formation and wear of the raceway surfaces.

The bearing dynamics and lifetime are experimentally analysed using an innovative and versatile test rig. The first contribution of the current work consists of the development of this test rig. The test rig is designed and constructed in-house and characterised by three unique features. Firstly, the test rig allows easy adjustment to test different types and sizes of rolling element bearings. The test bearing is mounted in a modular structure consisting of an auxiliary shaft and an intermediate sleeve. Secondly, the test rig allows applying a multi-axial static and dynamic load on the test bearing. The bearing load is controlled in both the radial and axial direction and has a static and dynamic component in both directions. Thirdly, the test rig allows simultaneous measurement of the bearing motion, the bearing dynamics and the behaviour of the lubricant film. Relations between the different measurements can be derived experimentally. The radial, axial and tilt motion are measured free from disturbances of the surrounding structure. The bearing dynamics are identified in a frequency range below the resonances of the surrounding structure's flexible modes. The behaviour of the lubricant film is analysed based on the electrical resistance through the bearing.

In the current study, a single row deep groove ball bearing is used as a test bearing. The bearing motion, the behaviour of the lubricant film and cage slip are analysed for different operational conditions of the bearing. The three properties are derived using techniques which can be applied in most rotating machinery: measurement of the radial bearing displacement and the electrical resistance through the bearing. Clear trends w.r.t. the bearing load, temperature and speed are obtained. Clean analysis of the bearing motion and cage slip further proves precise operation of the test rig. The electrical resistance reveals the formation of the lubricant film during a run-up of the bearing speed. Estimation of the lubricant film thickness based on the electrical resistance is validated using an analytical model. Exploring the possibilities to easily and accurately identify the properties is the second contribution of this work.

Accurate knowledge on the bearing dynamic properties is essential during the design of many rotating machinery. They determine the machine's critical speeds, the forces acting on the different components, etc. This work investigates two dynamic properties of the test bearing: the radial stiffness and damping in the direction of the static load. Variation of the bearing temperature reveals the influence of the lubricant's viscosity on the identified stiffness and damping. Variation of the bearing speed reveals the influence of the film formation on the identified stiffness and damping. In the literature, no experimental measurements showing the relations between the behaviour of the lubricant film and the dynamic properties are reported. Revealing these relations is the third contribution of the current study. The results help to evaluate the significance of modelling the lubricant film when numerically analysing the vibrations of a bearing system.

Precise prediction of the lifetime of rolling element bearings is a crucial step towards a reliable design of many rotating machines. For bearings subjected to highly varying loads, a strong reduction of the actual bearing lifetime w.r.t. the classically calculated bearing lifetime is observed. This work investigates the effect of external dynamic loads on the lubricant film formation and surface wear of the test bearing. When introducing a radial or axial excitation on the bearing, the lubricant film thickness follows the imposed variations of the load. An increase of metallic contact or breakdown of the lubricant film is not detected. Under axial excitation, sliding motion between asperities of the contacting surfaces in the bearing does occur. Accelerated lifetime tests under high axial dynamic load reveal polishing of the raceway honing structure. This polishing is clearly observed on SEM images of the inner raceway after a test duration of only 0.5% of the calculated L_{10} life. Analysis of the lubricant film behaviour under dynamic load is not described in the current literature and is considered to be the fourth contribution of this work. Finally, the study promotes further research to analyse surface wear due to external dynamic loads.

Samenvatting

Als een van de meest kritische componenten in de machinebouw, is de goede werking van wentellagers meestal essentieel voor het functioneren van machines. Wentellagers maken dan ook al meer dan 100 jaar het onderwerp van vele studies uit. Dit werk onderzoekt twee aspecten. Vooreerst wordt het dynamisch gedrag bestudeerd. De studie benadrukt de invloed van de smeerfilm op de lagerdynamica. Vervolgens wordt de levensduur bestudeerd. De studie bespreekt de invloed van een externe dynamische belasting op de vorming van de smeerfilm en op slijtage van de loopvlakken.

Het dynamisch gedrag en de levensduur van een lager worden experimenteel onderzocht met een innovatieve en veelzijdige testopstelling. De eerste bijdrage van het voorgestelde werk bestaat uit de ontwikkeling van deze opstelling. De testopstelling is binnenshuis ontworpen en gebouwd, en wordt gekenmerkt door drie unieke eigenschappen. Ten eerste, verschillende types en groottes van lagers kunnen worden getest. Hiervoor wordt het testlager gemonteerd in een modulaire structuur bestaande uit een hulpas en een bus. Ten tweede, een multi-axiale statische en dynamische belasting kan worden uitgeoefend op het lager. De lagerkracht wordt gecontroleerd in de radiale en axiale richting en heeft een statische en dynamische component in beide richtingen. Ten derde, de opstelling laat simultane meting van de lagerbeweging, de lagerdynamica en het gedrag van de smeerfilm toe. Relaties tussen de verschillende metingen kunnen experimenteel worden afgeleid. De lagerbeweging wordt gemeten in de radiale, axiale en tilt richting, vrij van storingen door de omringende structuur. De lagerdynamica wordt geïdentificeerd in een frequentiegebied beneden de resonanties van de structurele flexibele modes. Het gedrag van de smeerfilm wordt bestudeerd op basis van de elektrische weerstand van het lager.

Voor de studie wordt een enkelrijig groefkogellager als testlager gebruikt. De lagerbeweging, het gedrag van de smeerfilm en de kooislip worden onderzocht bij verschillende operationele condities van het lager. Dit gebeurt op basis van technieken die in de meeste machines toegepast kunnen worden: meting van de

radiale lagerverplaatsing en de elektrische weerstand van het lager. Duidelijke trends met betrekking tot de lagerkracht, de temperatuur en de snelheid worden bekomen. Zuivere analyse van de lagerbeweging en de kooislip bewijst de precieze werking van de testopstelling. De meting van de elektrische weerstand toont de vorming van de smeerfilm bij toename van de lagersnelheid. Schatting van de smeerfilmdikte op basis van de elektrische weerstand wordt gevalideerd met behulp van een analytisch model. Het verkennen van de mogelijkheden om eenvoudig en nauwkeurig de lagerbeweging, de kooislip en het gedrag van de smeerfilm te bestuderen is de tweede bijdrage van dit werk.

Accurate kennis van de dynamische lagereigenschappen is essentieel tijdens het ontwerp van vele roterende machines. Ze bepalen ondermeer de kritische snelheden en de krachten doorheen de verschillende componenten. Dit werk onderzoekt twee dynamische eigenschappen van het testlager: de radiale stijfheid en demping in de richting van de statische kracht. Variatie van de lagertemperatuur toont de invloed van de viscositeit van de smeerfilm op de geïdentificeerde stijfheid en demping. Variatie van de lagersnelheid toont de invloed van de vorming van de smeerfilm op de geïdentificeerde stijfheid en demping. In de literatuur worden zulke relaties tussen het gedrag van de smeerfilm en de dynamische eigenschappen niet beschreven. Het aantonen van deze relaties wordt gezien als de derde bijdrage van deze studie. Bij numerieke analyse van lagersystemen helpen de resultaten om het belang in te schatten van het modelleren van de smeerfilm.

Precieze voorspelling van de levensduur van wentellagers is een cruciale stap naar een betrouwbaar ontwerp van vele roterende machines. Bij sterk wisselend belaste lagers wordt een significante reductie van de werkelijke levensduur ten opzichte van de klassiek berekende levensduur waargenomen. Dit werk onderzoekt het effect van een externe dynamische belasting op de vorming van de smeerfilm en op slijtage van de loopringen. Bij introductie van een radiale of axiale excitatie op het testlager volgt de smeerfilmdikte de opgelegde veranderingen van de kracht. Verhoging van het metallisch contact of het openbreken van de smeerfilm wordt niet gedetecteerd. Bij axiale excitatie vindt er wel een afschuiving tussen oneffenheden van de rakende oppervlakken plaats. Versnelde levensduurtesten onder hoge axiale dynamische belasting vertonen polijsting van de hoonstructuur van de loopringen. Dit wordt reeds gezien na 0.5% van de L_{10} levensduur. Het effect van dynamische excitaties op de smeerfilm is niet beschreven in de literatuur, zodat het aantonen ervan wordt beschouwd als de vierde bijdrage van dit werk. Tot slot promoot de studie verder onderzoek naar slijtage van de loopvlakken door een externe dynamische belasting.

Abbreviations

1D	One-dimensional
2D	Two-dimensional
3D	Three-dimensional
AC	Alternating current
BPF	Ball pass frequency
BSF	Ball spin frequency
CAD	Computer aided design
COG	Centre of gravity
CPB	Constant percentage bandwidth
DC	Direct current
DEH	Distortion energy hypothesis
DER	Dark etching region
DGBB	Deep groove ball bearing
DOF(s)	Degree(s) of freedom
EHL	Elastohydrodynamic lubrication
FE	Finite element
FRF(s)	Frequency response function(s)
RCF	Rolling contact fatigue
RMS	Root mean square
SEM	Scanning electron microscope
TRB	Tapered roller bearing
WEC	White etching cracks
XRD	X-ray diffraction

Symbols

Hertzian contact

A	Contact surface area
A_i	Contact surface area at inner raceway
A_o	Contact surface area at outer raceway
a	Semi-major axis of the elliptical contact
b	Semi-minor axis of the elliptical contact
δ	Mutual approach of the contacting bodies
ϵ	Ellipticity parameter
E'	Reduced modulus of elasticity
E_I	Modulus of elasticity of body I
E_{II}	Modulus of elasticity of body II
ν_I	Poisson's ratio of body I
ν_{II}	Poisson's ratio of body II
κ	Complete elliptic integrals of the first kind
ε	Complete elliptic integrals of the second kind
p	Pressure
p_0	Maximum contact pressure
r	Reduced radius of curvature
$r_{1(I)}$	Radius of curvature in principal plane 1 of body I
$r_{1(II)}$	Radius of curvature in principal plane 1 of body II
$r_{2(I)}$	Radius of curvature in principal plane 2 of body I
$r_{2(II)}$	Radius of curvature in principal plane 2 of body II
σ_n	Normal stress at the surface
σ_x	Principal stress in the x-direction
σ_y	Principal stress in the y-direction
σ_z	Principal stress in the z-direction
τ_{max}	Maximum shear stress
w	Rolling element load

Bearing lifetime

C	Dynamic load rating
C_0	Static load rating
L_{10}	Rating life
n	Rotational speed
n_m	Mean rotational speed
p	Life exponent
P	Equivalent dynamic load

Bearing geometry

α	Contact angle
α_0	Contact angle resulting from internal clearance
D	Rolling element diameter
d_i	Inner raceway diameter
d_o	Outer raceway diameter
d_m	Pitch diameter
f_i	Osculation of inner raceway
f_o	Osculation of outer raceway
P_d	Radial internal clearance
P_e	Axial internal clearance
r_i	Inner raceway radius of curvature
r_o	Outer raceway radius of curvature
Z	Number of rolling elements

Spindle geometry

H	Distance between the pressure cone apices
R	Roller cone apex
S	Pressure cone apex

Electrical resistance

C_{TB}	Electrical capacitance of the test bearing
ρ	Lubricant film resistivity
R_K	Known resistance of the electrical circuit
R_{TB}	Electrical resistance of the test bearing
V_{in}	Voltage source of the electrical circuit
V_{out}	Voltage drop over the test bearing
Z_{TB}	Electrical impedance of the test bearing

Film thickness

α_{pv}	Pressure-viscosity index of the lubricant
η	Viscosity of the lubricant
η_0	Viscosity of the lubricant at 40 °C and low gauge pressure
h	Lubricant film thickness
h_0	Minimum lubricant film thickness
h_{0i}	Minimum lubricant film thickness at inner raceway
h_{0o}	Minimum lubricant film thickness at outer raceway
h_c	Central lubricant film thickness
h_{ci}	Central lubricant film thickness at inner raceway
h_{co}	Central lubricant film thickness at outer raceway
Λ	Film thickness parameter
Λ_i	Film thickness parameter at inner raceway
Λ_o	Film thickness parameter at outer raceway
R_a	Average surface roughness
s_i	RMS roughness of the inner raceway surface
s_o	RMS roughness of the outer raceway surface
s_r	RMS roughness of the rolling element surface
T_l	Temperature of the lubricant

Kinematic model

f_c	Frequency of the cage rotation
f_e	Frequency of the sine excitation
f_s	Frequency of the shaft rotation
ω_c	Angular velocity of the cage
ω_i	Angular velocity of the inner ring
ω_r	Angular velocity of the rolling elements
s_i	Slip at inner ring contact
s_o	Slip at outer ring contact
v	Velocity
v_c	Moving frame velocity of the cage
v_{ci}	Moving frame velocity of the inner ring contact
v_{co}	Moving frame velocity of the outer ring contact
v'_e	Entrainment velocity
v'_{ei}	Entrainment velocity at inner ring contact
v'_{eo}	Entrainment velocity at outer ring contact
v_i	Absolute velocity of the inner ring contact
v_o	Absolute velocity of the outer ring contact
v'_i	Relative velocity of the inner ring contact
v'_o	Relative velocity of the outer ring contact

v'_{ri}	Relative velocity of the rolling element at inner ring location
v'_{ro}	Relative velocity of the rolling element at outer ring location

Dynamic model

$\underline{\underline{C}}$	Damping matrix
c_{AS}	Combined damping of the air springs
c_B	Combined damping of the bushings
c_{MS}	Damping of the mounting system
c_S	Equivalent damping of the spindle
c_{TB}	Damping of the test bearing
c_{TB+MS}	Damping of the test bearing and mounting system in series
$\underline{F}$	Force vector
F	Force
F_a	Axial bearing load
$F_{a,d}$	Axial dynamic bearing load
$F_{a,s}$	Axial static bearing load
F_r	Radial bearing load
$F_{r,d}$	Radial dynamic bearing load
$F_{r,s}$	Radial static bearing load
$\underline{\underline{K}}$	Stiffness matrix
k_{AS}	Combined stiffness of the air springs
k_B	Combined stiffness of the bushings
k_{MS}	Stiffness of the mounting system
k_S	Bending stiffness of the spindle
k_{TB}	Stiffness of the test bearing
k_{TB+MS}	Stiffness of the test bearing and mounting system in series
$\underline{\underline{M}}$	Mass matrix
m_F	Equivalent mass of the frame
m_H	Mass of the test bearing housing
m_S	Equivalent mass of the spindle
$\underline{X}$	Displacement vector
x	Displacement
x_1	Displacement of the bearing housing
x_2	Displacement of the spindle
x_3	Displacement of the frame

Thermal model

$\dot{Q}$	Power loss
$\dot{Q}_c$	Power loss due to Coulomb friction
$\dot{Q}_v$	Power loss due to viscous friction
$R_{cond,o}$	Conduction resistance of the outer ring
$R_{cond,h}$	Conduction resistance of the housing
R_{conv}	Convection resistance
T_{1o}	Temperature of the outer ring at location 1
T_{2o}	Temperature of the outer ring at location 2
T_s	Temperature of the housing surface
T_∞	Temperature of the environment

Dynamic excitation

A_d	Displacement amplitude of the sine excitation
F_n	Normal load
μ	Coefficient of friction
v_{eff}	Effective velocity

Contents

List of Figures

List of Tables

Chapter 1

Introduction

The concept of rolling motion is known and used for thousands of years. The Assyrians (ca. 1100 BC) employed rollers under the sledges to carry massive stones. Simple forms of rolling element bearings were first used during the Roman civilisation. Leonardo da Vinci (1452-1519 AD) realised that the balls or rollers should be kept at a distance from each other to reduce friction. He presented the basic construction of modern rolling element bearings in his Codex Madrid. The general use did not occur until the Industrial revolution [46].

Nowadays, rolling element bearings are one of the most used components in mechanical applications. Across various industries, they play a crucial and effective role. A normal household contains about 150 rolling element bearings in different kinds of machinery [105]. A regular car contains over a 100 rolling element bearings.

A common rolling element bearing consists of an inner and outer ring and a number of rolling elements. Both rings have grooves or raceways to guide the rolling elements. The rolling elements are separated from each other by a cage. A small amount of clearance between the inner and outer ring is generally provided. To reduce the friction and wear in the rolling contacts, the bearing is lubricated [118].

Being particularly critical components, the serviceability of rolling element bearings is usually essential for the machine's operation. They have been the subject of research for more than a 100 years. This research focuses on the bearing materials, manufacturing, failure, lubrication, dynamics, etc. The knowledge is partly available in the open literature and partly protected by the bearing manufacturers.

1.1 Research motivation and objectives

The work of this manuscript investigates two aspects of rolling element bearings. Firstly, the dynamic behaviour of a rolling element bearing is analysed. The study emphasises the influence of the lubricant film on the bearing dynamics. Secondly, the lifetime of the bearing is analysed. The study discusses the influence of external dynamic loads on the lubricant film formation and wear of the raceway surfaces.

1.1.1 Influence of the lubricant film on the bearing dynamics

The need to reduce vibrations of rotating machinery has stimulated researchers for many years to analyse the dynamic behaviour of rolling element bearings. As the bearings are in the transmission path of vibrations between the shaft and bearing housing, they play a key role in the resulting vibrations. They determine for instance the machine's critical speeds and the forces acting on the different components. Subsequently, they influence the noise emanating from the machine and component stresses and wear.

Modelling and simulation methods provide an increasingly accurate approach for predicting the dynamic performance of mechanical systems. The bearing models evolved from analytical formulations of a nonlinear spring to complex multibody simulations. Nevertheless, models of rolling element bearings are typically the most inaccurate when compared with those of other machine components [102]. Experimental validation of the current models is one of the main concerns related to the research involving bearing modelling. More realistic data regarding stiffness and damping properties of bearings is required [19].

During rotation of a rolling element bearing, a lubricant film between the rolling elements and raceways forms. While the influence of the bearing's internal geometry and its loading conditions on the static stiffness is well understood, little information about the influence of the lubricant film is provided. Due to the high pressure in the lubricated rolling contacts, a strong interaction between the lubricant film and the deformation of the contacting surfaces exists. Experimental studies analysing the relations between the lubricant film behaviour and the bearing dynamics are lacking in the current literature. The study of this manuscript aims to fill this gap. The stiffness and damping characteristics of a commonly used deep groove ball bearing (DGBB) are experimentally analysed. The results are linked to the measured behaviour of the lubricant film inside the bearing. The study helps to understand whether the lubricant film should be modelled when numerically analysing the vibrations of a bearing system.

1.1.2 Influence of external dynamic loads on the bearing lifetime

The importance of research related to failure and damage detection of bearings is self-explanatory. Rolling element bearing failure is one of the foremost causes of breakdown in rotating machinery [67]. Bearings fail prematurely in service due to contamination, poor lubrication, poor fits, misalignments, etc. Motor bearing faults account for more than 40% of the induction motor's failure [85]. Gearbox bearing failure is the top contributor of the wind turbine's downtime [68]. Bearings are cheap, but bearing failure is not. A 4000 € wind turbine bearing replacement can turn into a 200000 € project, even without including the cost of downtime [47].

Lifetime calculations of bearings are based on the ISO 281 [56] standard. For bearings subjected to highly varying loads, recent research emphasises a strong reduction of the actual bearing lifetime w.r.t. the calculated bearing lifetime. Failure rates of wind turbines approximating three times the failure rate of conventional generators are observed [124]. This is partly due to the unique operational conditions of the bearings, resulting from widely varying wind loads and high vibration levels [96].

The study of this manuscript aims to understand the effect of externally applied dynamic loads on the bearing lifetime. The test object is a commonly used deep groove ball bearing. Firstly, the behaviour of the lubricant film during strong external excitation is analysed. Secondly, damage of the raceway surfaces is investigated after the bearing is dynamically loaded for a long period of time.

1.2 Main contributions and manuscript outline

The main contributions of this study are arranged according to the four main chapters of the manuscript (Chapter 3 to 6). The state-of-the-art related to the study is reviewed in Chapter 2.

1.2.1 Bearing test rig

To experimentally analyse the dynamic behaviour and lifetime of a rolling element bearing, a novel test rig is developed. The test rig is designed and constructed in-house. The first contribution of the current work consists of the development of this test rig. A full description of the design is given in Chapter 3. The test rig has three unique features:

1. Easy adjustment to test different types and sizes of rolling element bearings.

   The test rig allows easy adjustment to test different types of bearings (i.e. deep groove ball bearings, angular contact ball bearings and tapered roller bearings) with an outer diameter varying from 20 to 52 mm. The test bearing is mounted in a modular structure adapted to the specifications provided by the bearing manufacturer.

2. Multi-axial static and dynamic loading of the test bearing.

   The test rig allows multi-axial static and dynamic loading of the test bearing. The bearing load is controlled in both the radial and axial direction, independent of each other. The load has a static and dynamic component in both directions. Real-life conditions, where i.e. gear meshing forces are acting on the bearing, are simulated.

3. Simultaneous measurement of the bearing motion, the bearing dynamics and the behaviour of the lubricant film.

   The test rig allows simultaneous measurement of the bearing motion, the bearing dynamics and the behaviour of the lubricant film. Relations between the different measurements can be derived experimentally. The bearing motion is measured free from disturbances of the surrounding structure. The bearing dynamics are identified in a frequency range below the resonances of the surrounding structure's flexible modes. The behaviour of the lubricant film is analysed based on the electrical resistance through the bearing.

1.2.2 Operational behaviour of the test bearing

In the work of this manuscript, the most common type of bearing and lubricant are analysed. The test bearing is a single row deep groove ball bearing. Lubrication of the bearing is done with grease. Three operational properties, namely the bearing motion, the behaviour of the lubricant film and cage slip, are analysed. The bearing motion is considered as any motion deviating from pure rotation. The behaviour of the lubricant film is characterised by the lubricant film thickness between the rolling elements and raceways. The cage slip is defined as a deviation of the cage speed from its theoretical value. Understanding these properties is needed when discussing the bearing dynamics and lifetime. Chapter 4 describes the results.

The study shows that the bearing motion, the behaviour of the lubricant film and cage slip are accurately identified. This, based on techniques which can be applied in most rotating machinery: measurement of the radial bearing displacement and the electrical resistance through the bearing. The three properties are analysed for different operational conditions of the bearing. Clear trends w.r.t. the bearing load, temperature and speed are obtained. Exploring the possibilities to easily and accurately identify the three operational properties is the second contribution of this work.

1.2.3 Dynamic behaviour of the test bearing

The dynamic properties of the test bearing are experimentally analysed. Two properties of the bearing, both its stiffness and damping value in the direction of the radial static bearing load, are identified. The influence of the static bearing load, temperature and speed on these properties is investigated. The results are discussed in Chapter 5.

Identification of the bearing stiffness and damping is based on the dynamic response of the test rig. The test rig is dynamically excited using an electrodynamic shaker while its response is measured using an accelerometer. Fitting a spring-mass-damper model of the test rig to the measured response allows identifying the bearing dynamic properties. The behaviour of the lubricant film between the rolling elements and raceways is simultaneously measured based on the electrical resistance through the bearing.

When varying the bearing operational temperature and rotational speed, a clear link between the lubricant film behaviour and changes of the bearing dynamics is observed. Until now, these relations are unreported in the open literature. Revealing the relations is the third contribution of the current study.

1.2.4 Dynamic loading of the test bearing

The effect of external dynamic loads on the lifetime of the test bearing is analysed. Two separate investigations are conducted. The behaviour of the lubricant film during dynamic excitation is analysed using the electrical resistance through the bearing and the measured bearing motion. Wear of the raceway surfaces due to external dynamic loads is analysed after a series of accelerated lifetime tests. Chapter 6 reviews the results.

Electrodynamic shakers introduce a sine excitation in the radial and axial direction of the bearing. The shakers simulate the excitation resulting from a structural resonance or gear meshing. When applying a radial or axial excitation on the bearing, the lubricant film thickness follows the imposed variations of the load. An increase of metallic contact or breakdown of the lubricant film is not detected. Under axial excitation, sliding motion between surface peaks, also called asperities, of the contacting surfaces in the bearing does occur. Accelerated lifetime tests under high axial dynamic load reveal polishing of the raceway honing structure. This polishing is clearly observed on microscope images of the inner raceway after a test duration of only 0.5% of the calculated L_{10} life.

Analysis of the lubricant film behaviour under dynamic load is not described in the current literature and is considered to be the fourth contribution of this work. Also, the study promotes further research to analyse surface wear due to external dynamic loads.

Chapter 2

Literature review

Before discussing the test rig and its measurements, the state-of-the-art on different topics of this manuscript is reviewed:

- Sect. 2.1 introduces the surface and subsurface stresses in rolling contacts. The analysis is limited to rolling contacts of ball bearings, as the study of this manuscript focuses on ball bearings.
- Sect. 2.2 discusses the lubrication of rolling element bearings. The formation of a lubricant film between the non-conformal contacts in rolling element bearings is described. Also, the different methods for measuring the lubricant film thickness and the different types of lubricants are reviewed. The lubrication mechanism of grease lubrication is finally introduced.
- Sect. 2.3 reviews the current literature on the dynamics of rolling element bearings. Most of the experimental studies conducted in the past focused on the dynamics of spindles. The state-of-the-art concerning the relation between the lubricant film and the bearing dynamics is further discussed.
- Sect. 2.4 describes the common fatigue failure modes and the general lifetime calculations of bearings. Gegner and Nierlich analyse the influence of external dynamic loads on the bearing lifetime. A short overview of their work is provided.

2.1 Stresses in rolling contacts

This section introduces the surface and subsurface stresses in rolling contacts of ball bearings. It is based on Refs. [7, 46].

2.1.1 Surface stresses

When two elastic solids contact under a load w, a contact area develops. In many engineering applications such as rolling element bearings, gears and cams, the contact area is small and the resulting pressure is high. The deformation and stresses are determined from analytical formulas, based on the theory of elasticity and derived by Hertz. Hertz developed this theory during his Christmas vacation in 1880 when he was 23 years old [104].

Hertz's contact model is based on the following assumptions [7, 118]:

- The material deformation is elastically.
- The load is directed normal to the contacting surfaces, such that surface shear stresses can be neglected.
- The dimensions of the contact area are small compared to the radii of curvature of the contacting bodies.
- The deformation of the contact area is small compared to the dimensions of the contact area.
- The effect of surface roughness is negligible.

For a point contact in ball bearings, an elliptical shape of the contact area is assumed. Fig. 2.1**a** shows the contact geometry and the definition of the coordinate system used in this manuscript. The rolling element load w is oriented in the x-direction, the rolling direction equals the y-direction and the bearing's rotation axis is oriented in the z-direction. The contact is characterised by its radii of curvature in two principal planes, perpendicular to each other. The first principal plane (xz-plane) contains the bearing's rotation axis and a rolling element centre. The semi-major axis of the elliptical contact a is located in this plane. The second principal plane (xy-plane) is perpendicular to the rotation axis and contains a rolling element centre. The semi-minor axis of the elliptical contact b is located in this plane.

Table 2.1 summarises the different radii of curvature of the inner and outer raceway contacts in ball bearings. The radii are positive when the curvature is

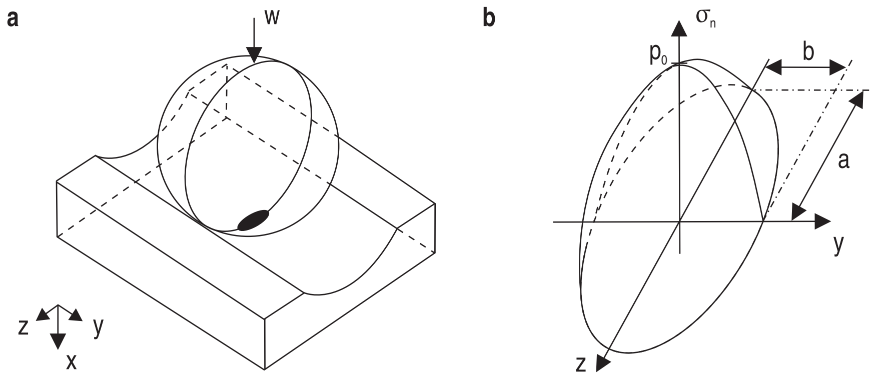

Figure 2.1: Formation of an elliptical contact area (black area) (**a**) and the corresponding surface stress distribution (**b**) (adapted from Ref. [46]).

convex and negative when the curvature is concave. In the first principal plane, the osculation of the inner raceway f_i and the outer raceway f_o defines the relation between the radius of curvature of the rolling element and the raceway. In the second principal plane, the rolling element diameter D, the inner raceway diameter d_i and the outer raceway diameter d_o (Fig. 4.1**b**) define the radii of curvature.

The ellipticity parameter ϵ of the elliptical contact is given by:

$$\epsilon = \frac{a}{b} \tag{2.1}$$

The contact problem is reduced to the problem of a paraboloid shaped surface approaching a flat surface [118]. The reduced radius of curvature r of the paraboloid is derived from the radii of curvature of both body I and body II in the following way:

$$\frac{1}{r_1} = \frac{1}{r_{1(I)}} + \frac{1}{r_{1(II)}} \tag{2.2}$$

$$\frac{1}{r_2} = \frac{1}{r_{2(I)}} + \frac{1}{r_{2(II)}} \tag{2.3}$$

$$\frac{1}{r} = \frac{1}{r_1} + \frac{1}{r_2} \tag{2.4}$$

Table 2.1: Geometry defining the Hertzian contact.

Body	Principal plane 1	Principal plane 2
Outer ring (I)	$r_{1(I)} = -f_o \, \frac{D}{2}$	$r_{2(I)} = -\frac{d_o}{2}$
Rolling element (II)	$r_{1(II)} = \frac{D}{2}$	$r_{2(II)} = \frac{D}{2}$
Rolling element (II)	$r_{1(II)} = \frac{D}{2}$	$r_{2(II)} = \frac{D}{2}$
Inner ring (I)	$r_{1(I)} = -f_i \, \frac{D}{2}$	$r_{2(I)} = \frac{d_i}{2}$

The reduced modulus of elasticity E' takes into account the moduli of elasticity E_I and E_{II} and the Poisson's ratios ν_I and ν_{II} of the materials of both contacting bodies:

$$\frac{2}{E'} = \frac{1-\nu_I^2}{E_I} + \frac{1-\nu_{II}^2}{E_{II}} \tag{2.5}$$

The complete elliptic integrals of the first kind κ and second kind ε are respectively:

$$\kappa = \int_0^{\pi/2} \left(1 - \left(1 - \frac{1}{\epsilon^2}\right) \sin^2\phi\right)^{-1/2} \mathrm{d}\phi \tag{2.6}$$

$$\varepsilon = \int_0^{\pi/2} \left(1 - \left(1 - \frac{1}{\epsilon^2}\right) \sin^2\phi\right)^{1/2} \mathrm{d}\phi \tag{2.7}$$

Numerical integration is avoided when applying approximations for the elliptic integrals and the ellipticity parameter. Brewe and Hamrock [8] obtained these approximations using a least squares method of linear regression:

$$\epsilon \approx 1.0339 \left(\frac{r_2}{r_1}\right)^{0.636} \tag{2.8}$$

$$\kappa \approx 1.5277 + 0.6023 \ \ln \left(\frac{r_2}{r_1}\right) \tag{2.9}$$

$$\varepsilon \approx 1.0003 + \frac{0.5968}{\left(\frac{r_2}{r_1}\right)} \tag{2.10}$$

For $1 \leq \epsilon \leq 10$, the error in the calculation of ϵ is less than 3%. The error on κ is nil except at $\epsilon = 1$, where it is less than 2.6%. The error on ε is nil except at $\epsilon = 1$, where it is less than 2% [46]. The simplified approximations for the elliptic integrals and the ellipticity parameter are used to derive the semi-major and semi-minor axis of the elliptical contact:

$$a = \left(\frac{6 \ \epsilon^2 \ \varepsilon \ r \ w}{\pi \ E'}\right)^{1/3} \tag{2.11}$$

$$b = \left(\frac{6 \ \varepsilon \ r \ w}{\pi \ E' \ \epsilon}\right)^{1/3} \tag{2.12}$$

The contact surface area A is given by:

$$A = \pi \ a \ b \tag{2.13}$$

The mutual approach δ of remote points in the contacting bodies is derived from:

$$\delta = \frac{\kappa}{\pi \ r} \left(\frac{3 \ \ \pi \ r \ w}{2 \ E' \ \epsilon^2 \ \varepsilon}\right)^{2/3} \tag{2.14}$$

The normal stress is distributed over the contact area in the form of a semi-ellipsoid, as shown in Fig. 2.1**b**. The maximum normal stress at the surface p_0 occurs at the geometrical centre of the contact area and thus amounts 1.5 times the evenly distributed pressure:

$$p_0 = 1.5 \ \frac{w}{A} \tag{2.15}$$

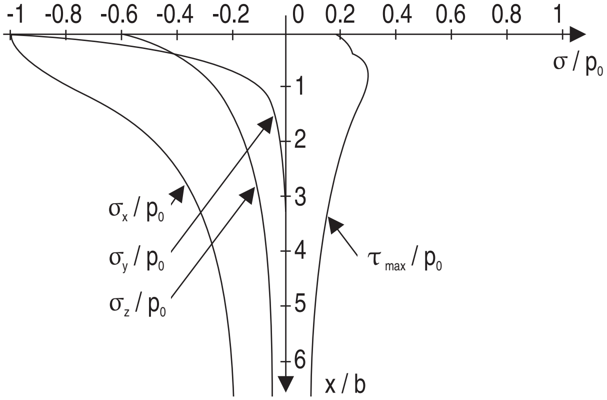

Figure 2.2: Subsurface stresses below the centre of the contact area with increasing depth x (adapted from Ref. [7]).

This maximum stress is also called maximum Hertzian contact pressure. The normal stress σ_n at all other points within the contact area is given by:

$$\sigma_n = p_0 \left(1 - \left(\frac{z}{a}\right)^2 - \left(\frac{y}{b}\right)^2\right)^{1/2} \tag{2.16}$$

2.1.2 Subsurface stresses

Hertz's analysis pertained only to the surface stresses caused by a concentrated force applied perpendicular to the surface. The principal stresses occurring below the centre of the contact area were calculated by Jones [58]. Based on Mohr's circle, the maximum shear stress is derived as well. Fig. 2.2 shows the principal stresses σ_x, σ_y and σ_z and the maximum shear stress τ_{max}. The principal axes coincide with the coordinate axes of Fig. 2.1**a**. While the principal stresses are maximal at the surface, the shear stress τ_{max} reaches a maximum at a point below the surface.

Due to friction between the rolling elements and raceways, tangential forces are introduced on the surface. The effect of the resulting surface shear stress on the subsurface stresses was analysed by Zwirlein and Schlicht [127]. The von Mises equivalent stress below the surface was calculated for different ratios between the surface shear stress and the applied normal stress. The ratio between the surface shear stress and the normal stress equals the coefficient of friction μ.

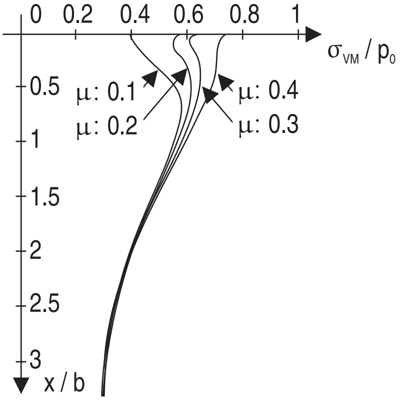

Figure 2.3: Distribution of the von Mises equivalent stress below the surface for different values of the coefficient of friction (adapted from Ref. [127]).

Fig. 2.3 visualises the von Mises equivalent stress below the surface for different values of the coefficient of friction. As the coefficient of friction increases, the maximum equivalent stress increases and moves closer to the surface. The maximum equivalent stress occurs at the surface when the coefficient of friction exceeds 0.3.

2.2 Lubricant film

This section gives some general considerations on the elastohydrodynamic lubricant film formed in rolling element bearings. It is based on Refs. [46, 104].

2.2.1 Viscosity of the lubricant film

The behaviour of a lubricant film is mainly determined by its viscosity. The viscosity η defines the proportionality between the shear stress acting on the lubricant and the shear rate. Consider two flat surfaces with surface area A, separated by a layer of lubricant with a thickness h (Fig. 2.4). The relative velocity between both plates v defines the shear rate v/h. The shear force F is given by:

$$\frac{F}{A} = \eta \, \frac{v}{h} \tag{2.17}$$

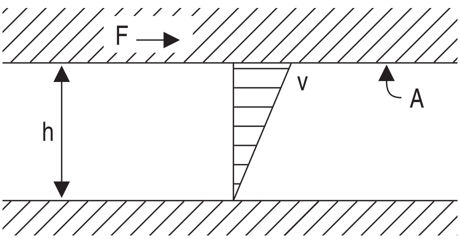

Figure 2.4: Two flat surfaces separated by a layer of lubricant (adapted from Ref. [104]).

The relation between the shear rate and the viscosity depends on the structural complexity of the lubricant. Liquids such as water and benzene have a loose molecular structure which is not affected by shearing action. The viscosity of these Newtonian liquids is independent of the shear rate. Pure mineral oils exhibit this behaviour up to relatively large shear rates of 10^5 to 10^6 s^{-1}. Liquids in which the suspended molecules form a structure that interferes with the shearing of the suspension medium are considered to be non-Newtonian. The viscosity is no longer independent of the shear rate. Greases exhibit non-Newtonian behaviour.

The viscosity not only depends on the shear rate (when non-Newtonian), but also the lubricant's temperature. An exponential decrease of the lubricant's viscosity with increasing temperature is observed. Among several empirically and theoretically derived expressions, the viscosity-temperature relation is most accurately described by the Vogel equation. With T_l being the absolute temperature and a, b and c being constants, the Vogel equation states:

$$\eta = a\ \mathrm{e}^{\left(\dfrac{b}{T_l - c}\right)} \tag{2.18}$$

Finally, the viscosity changes w.r.t. the pressure acting on the lubricant film. A strong increase of the lubricant's viscosity with increasing pressure is observed. The viscosity-pressure relationship is commonly described by the Barus law, showing an exponential increase of the viscosity η with rising pressure p:

$$\eta = \eta_0 \mathrm{e}^{\alpha_{pv} p} \tag{2.19}$$

Here, η_0 is the base viscosity at low gauge pressure and the constant α_{pv} is known as the pressure-viscosity index. At pressures above 500 MPa, other formulations have been proven more accurate. An overview of the different viscosity-pressure relationships available in the literature is given in Refs. [101, 114]. The viscosity of mineral oil increases by a factor 10^6 when applying a contact pressure of 1000 MPa [15].

2.2.2 Elastohydrodynamic lubrication

The existence of a lubricant film inside rolling element bearings was suspected long before it could be proven or described using specific scientific concepts. The lubrication mechanisms in conformal contacts, where the surfaces fit snugly into each other with a high degree of geometrical conformity, were well understood. These conformal contacts are encountered in hydrodynamic and hydrostatic bearings. The mechanism of lubrication operating in highly loaded non-conformal contacts, such as those found in gears and rolling element bearings, was poorly understood. The wear rates of these devices are very low. This implies the existence of films, sufficiently thick to separate the opposing surfaces. The calculated values of the hydrodynamic film thicknesses were so low that it was inconceivable for the contacting surfaces to be separated by a viscous liquid film. The calculations suggested that the surfaces were lubricated by films having a thickness of only one molecule. In experiments specifically designed to permit lubrication by monomolecular films, much higher wear rates and friction coefficients were observed. This apparent contradiction between the empirical observation of effective lubrication and the limits of known lubrication mechanisms could not be explained for a considerable period of time.

In the 1940s, a substantial amount of work was devoted to resolving lubrication in non-conformal contacts. The first realistic model which provided an approximate solution for the film thickness was proposed by Ertel and Grubin [33]. It was found that the combination of three effects are instrumental to this mechanism: hydrodynamic lubrication, elastic deformation of the metal surfaces and the increase in viscosity of oil under extreme pressures. It was shown theoretically that under the condition of intense contact stress, a lubricating oil film can be formed. This elastohydrodynamic lubrication (EHL) film is very thin (0.1 to 1 μm), but manages to separate the interacting surfaces.

The non-conformal geometry of the contacting surfaces causes an intense concentration of load over a small area for almost all Hertzian contacts of practical use. Lubricant pressures from 1000 to 4000 MPa are found in typical machine elements. Dowson [24] and Gohar [32] investigated the formation of the lubricant film by simultaneous solution of the Reynolds equation, the equations of elasticity and the viscosity-pressure relationship of the lubricant. General

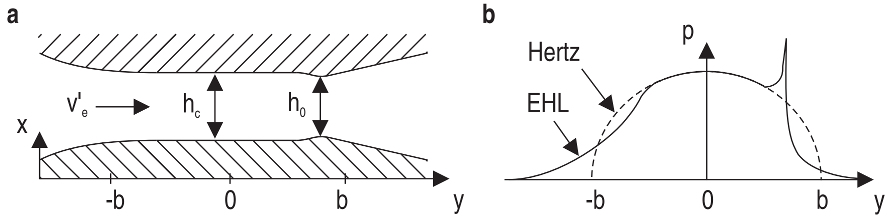

Figure 2.5: Profile of the lubricant film (**a**) and the corresponding pressure distribution (**b**) (adapted from Ref. [104]).

formulations of the EHL film thickness under fully flooded isothermal conditions were derived. These formulations are routinely used to this day.

2.2.3 Thickness of the lubricant film

In a stationary contact between a ball and raceway, the pressure distribution is ellipsoidal according to the classical Hertzian theory (Fig. 2.1**b**). The pressure field changes when the lubricant is dragged into the contact with a mean velocity v'_e. An EHL film is generated, which modifies the pressure distribution at the entry and exit regions of the contact. Fig. 2.5 shows the profile of the lubricant film and the pressure distribution along the minor axis of the elliptical contact. The combined effect of relative movement and film formation results in a slightly increased contact area. At the entry region, the hydrodynamic pressure is therefore lower than in case of a dry Hertzian contact. The opposing surfaces within the contact are almost parallel and planar. The film is described by the central lubricant film thickness h_c in this region. The lubricant experiences precipitous rise of viscosity as it enters the contact followed by an equally sharp decline to ambient viscosity levels at the exit of the contact. To maintain continuity of flow and compensate for the loss of lubricant viscosity at the contact exit, a constriction close to the exit is formed. The minimum lubricant film thickness h_0 is found at the constriction. The minimum lubricant film thickness is an important parameter since it controls the likelihood of asperity interaction between the surfaces. A pressure peak is generated at the constriction, especially at high speed and light load.

The elastohydrodynamic film in rolling element bearings is very thin. To prevent asperity contacts between the rolling surfaces, it should be of a magnitude comparable to the mean surface roughness. The extent by which the film thickness exceeds the surface roughnesses is conventionally indicated by the film thickness parameter Λ. This ratio of the minimum lubricant film thickness

h_0 to the mean component surface roughness reflects the severity of asperity contact between the rolling surfaces. For the inner ring contact having an RMS roughness of the raceway surface s_i and an RMS roughness of the rolling element surface s_r, the film thickness parameter equals:

$$\Lambda_i = \frac{h_{0i}}{\sqrt{s_i^2 + s_r^2}} \tag{2.20}$$

For the outer ring contact having an RMS roughness of the raceway surface s_o, a similar expression is used:

$$\Lambda_o = \frac{h_{0o}}{\sqrt{s_o^2 + s_r^2}} \tag{2.21}$$

In general, the RMS roughness values are considered being 1.25 times the average surface roughness values R_a. Three lubrication regimes are distinguished based on the film thickness parameter [122]:

- $\Lambda \geq 3$: full-film lubrication.

  Full separation is achieved. The contact load is carried entirely by the lubricant film. The overall performance is predicted by the classical EHL theory considering smooth surfaces.

- $1 \leq \Lambda < 3$: mixed lubrication.

  A considerable amount of contact between asperities occurs. The local lubricant film can be interrupted at the tip of tall asperities. The contact load is shared between the lubricant film and contacting asperities.

- $\Lambda < 1$: boundary lubrication.

  Asperity contact predominates and severe surface distress is expected.

2.2.4 Measurement of the EHL film behaviour

To measure the EHL film behaviour, different methods have been developed over the years. They are based on:

- The electrical resistance of the lubricant film.

  This method is primarily used in detecting lubricant films and possible breakdown of lubricant films.

- The electrical capacitance of the lubricant film.

  This method was pioneered by Crook [17] who measured the film thickness between steel rollers. Later, the method was refined by Dyson [25]. The film thickness can be estimated with reasonable accuracy.

- Differences in strain caused by the EHL film.

  This method was developed by Meyer and Wilson [74]. A bearing with negative internal clearance (preload) is used. As the lubricant film is formed, the internal clearance of the bearing further reduces. Strain gauges measure a subsequent change of the deformation of the outer ring.

- X-ray beams passing through the lubricated contact between two surfaces.

  This technique was originally developed by Sibley [97, 98]. Since the lubricant scarcely absorbs X-rays in comparison to the metallic contacting bodies, differences in film thickness can be detected. In the experiments conducted, the X-ray beam was oriented along the tangent plane between two lubricated rolling discs and the film thickness was evaluated from the radiation intensity measurements of the emerging beam.

- Optical interferometry.

  This method was first pioneered by Kirk [64] and Cameron and Gohar [10]. In its original form, a steel ball is driven by a chromium coated glass disk. An EHL film is formed between the ball and the disk. White light is shone through the contact between the glass disc and the steel ball. The semi-reflecting chromium layer reflects some of the light while some of the light passes through the lubricant and is reflected of the steel ball. The two reflected beams will either constructively or destructively interfere to produce an interference pattern, resulting in a graduation of colours depending on the film thickness.

Only the first three methods can be used to analyse the lubricant film in unmodified rolling element bearings. When metallic contact appears in the bearing contacts, determining the lubricant film thickness with the resistance and capacitance method is hampered [25, 81]. Zhang [81] proposes the R-C oscillation technique to improve the estimation in mixed lubrication conditions. The bearing is part of a Wien's oscillator circuit. The lubricant film thickness is derived from the resonance frequency of this circuit.

2.2.5 Types of lubricants

Different types of lubricants are used to lubricate rolling element bearings. The choice depends on the operational temperature, cooling requirements, accessibility for maintenance, cost, etc. The following three types are commonly used:

- Liquid lubricants.

  Both mineral oils and synthetic oils are employed to lubricate bearings. Mineral oils have a wide range of molecular constituents and molecular chain lengths, giving rise to a large variation in flow properties and chemical performance. They are generally enhanced with additives to improve both the mechanical and chemical performance.

- Grease.

  Grease consists of an oil that is physically retained in a thickener by capillary action. The thickener is generally a soap or another material composed of very long, twisted or contorted molecules that both physically interlock and have a large surface area to retain the oil. The grease behaves as a soft solid, capable of bleeding oil at controlled rates to meet the consumption demands of the bearing.

- Solid lubricants.

  Solid lubricants are used when extreme operating environments such as very high temperature, very high pressure or hard vacuum preclude the use of liquid lubricants or greases. As compared to the film forming capability of liquid lubricants and greases, solid lubricants perform as boundary lubricants, consisting of thin layers of lower shear strength than the bearing materials. The use of solid lubricants results in higher bearing friction, higher bearing temperatures and wear if they are not replenished appropriately.

2.2.6 Lubrication mechanism of grease

Several publications focus on the mechanism of grease lubrication in rolling element bearings.

During the initial phase of the bearing operation, most of the grease is pushed out of the bearing and no longer actively participates in the lubrication process. This only leaves a limited quantity available, which is stored inside the bearing geometry and on the bearing shoulders. The stored volume strongly determines the remaining lubrication process in the bearing [69].

The lubricated contacts are replenished by side flow. The rolling elements partly push the lubricant to the side of the contacts after which the reflow will provide fresh lubricant for the next rolling element. The reflow is driven by surface tension and restricted by the viscosity. Thick oils and greases may yield problems, which is generally observed in practice [31].

Different viewpoints exist concerning the exact mechanism of grease operation. Until recently, grease was considered as merely a sponge holding oil near the working contacts. As these contacts consumed oil by way of evaporation and oxidation, a replenishment flow maintained equilibrium as long as the supply lasted. Research using optical EHL and microflow lubrication assessment techniques has shown that the thickener phase plays rather complex roles in both the development of the film and in the modulation of the replenishing flows. How the thickener controls oil outflow, reabsorbs fluid thrown from the contacts and acts as a trap for debris are little understood at this time.

2.3 Dynamic behaviour of rolling element bearings

The dynamics of rolling element bearings are being studied for more than 40 years. A small review of this research is given in the current section.

2.3.1 Spindle dynamics

The first experimental research on the stiffness and damping characteristics of rolling element bearings aimed to understand the dynamics of spindles. To improve the accuracy of the spindle operation, the dynamics of machine tool spindles were analysed [65]. Ref. [107] summarises this early work. Snoeys [26] focused on the tilt damping of tapered roller bearings. Stone [116] and Weck [117] analysed the radial stiffness and damping of two axially preloaded bearings. Both pairs of tapered roller bearings and angular contact bearings were investigated.

Later research investigated the effect of the temperature-dependent preload on the spindle dynamics. Gunduz [34] gives an overview of both numerical and experimental studies on this subject. The calculations were based on two to five degrees of freedom models of the bearings, allowing a relative motion between the inner and outer ring in two to five directions. The radial and axial preload were related to the stiffness coefficients of the models [92]. Nonlinear effects [119], high speed effects [59] and variable elastic compliance [3] were discussed. Experimental studies analysed the resonance frequencies of shaft-bearing systems at various preloads and speeds. In most studies, special rigs were built for excitation and response measurement of the rotor. The stiffness and damping characteristics of the spindle bearings were derived from these input-output relations.

2.3.2 Influence of the lubricant film

Due to the strong interaction between the EHL film and the deformation of the contacting surfaces, the lubricant film affects the stiffness and damping characteristics of the bearing. The influence of the lubricant film is analysed both numerically and experimentally.

One of the most up-to-date analyses of the stiffness and damping evaluation for elastohydrodynamic contacts is based on the assessment of the dynamic response through a full dynamic simulation of the contact forces. It was first published by Wijnant [120] and later extended by Wensing [118] and Nonato [79, 80]. Owing to the formation of a lubricant film, an increasing stiffness of each contact in comparison to a dry contact is observed. Also, the effective internal bearing clearance is reduced. The formation of a lubricant film consequently leads to an increased bearing stiffness.

Experimental studies analyse the variations of the bearing dynamics for different values of the load, speed and lubricant's viscosity. Dietl [19] measures the damping capabilities of two rolling element bearings supporting a rigid shaft. Mitsuya [75] investigates the damping characteristics of a single deep groove ball bearing. A higher damping of the lubricated bearing in comparison to a dry bearing is observed in each publication. The difficulty of performing sufficiently accurate measurements and the multitude of parameters influencing the results (type of bearings, radial and axial preload, speed, loose/interference fits of the bearing seats, lubricant properties, temperature, etc.) is emphasised in most of these publications.

2.4 Lifetime of rolling element bearings

This section reviews the common fatigue failure modes and the general lifetime calculations of steel bearings. The influence of external dynamic loads on the bearing lifetime is also discussed. It is based on Refs. [7, 28].

2.4.1 Common fatigue failure modes

Every rolling element bearing rotating under load above the endurance strength limit has a definite fatigue life. The bearing approaches the end of its life when the rolling surfaces are damaged by rolling contact fatigue (RCF). Two mechanisms of fatigue damage initiation can be distinguished [76]:

- The subsurface failure mode.

  In most applications, the lubrication of the rolling contacts is at least adequate and the friction between the rolling elements and raceways is negligible. The von Mises equivalent stress reaches its maximum at a point below the surface (Fig. 2.3). The stress can locally exceed the yield strength of the bearing steel (between 1400 and 1800 MPa) such that plastic deformation occurs.

  Marked alterations of the microstructure of endurance tested bearings have been reported since 1946. The alterations are concentrated at a depth corresponding to the maximum von Mises equivalent stress. The distortion energy hypothesis (DEH), also known as the von Mises criterion, is therefore considered the best criterion for subsurface RCF. A microscope image of the microstructural alterations is shown in Fig. 2.6**a**. A dark etching region (DER) below the rolling surface is formed. The DER contains plastically deformed bands, 80 ° inclined w.r.t. the rolling direction [109].

  During cyclic loading, residual stresses build up and minute cracks are formed below the surface. This is often observed in the region of material inhomogeneities, where the stresses are maximal. The subsurface cracks eventually progress towards the surface. Surface material can break loose such that deep spalls are formed. An example is given in Fig. 2.6**b**. During the remaining bearing lifetime, the damage spreads rapidly since torn-off particles are rolled over causing local overloading. A detrimentally preloaded bearing, for instance due to poor fits or misalignment, fails prematurely due to RCF initiated below the surface.

- The surface failure mode.

  Ceramic or metallic foreign solid particles contaminate the lubricant in the contacts. The solid particles originate for instance from the grinding process of the bearing and/or its surrounding structure (carbide cluster). Due to overrolling during the bearing operation, indentations on the raceway surfaces are formed. Fig. 2.7**a** shows these indentations on a raceway surface of a contaminated bearing. The Hertzian microcontacts between the surfaces and the solid particles are subjected to cyclic loading. This results in increasing residual stresses near the surface up to a depth related to the size distribution of the indentations.

  Strain hardening by severe plastic deformation leads to material embrittlement and subsequent crack initiation on the surface. Further failure development produces shallow V-shaped pits of originally only several micrometers deep. The pits are formed behind the indentations. An example is given in Fig. 2.7**b**. Chips of surface material flake off causing

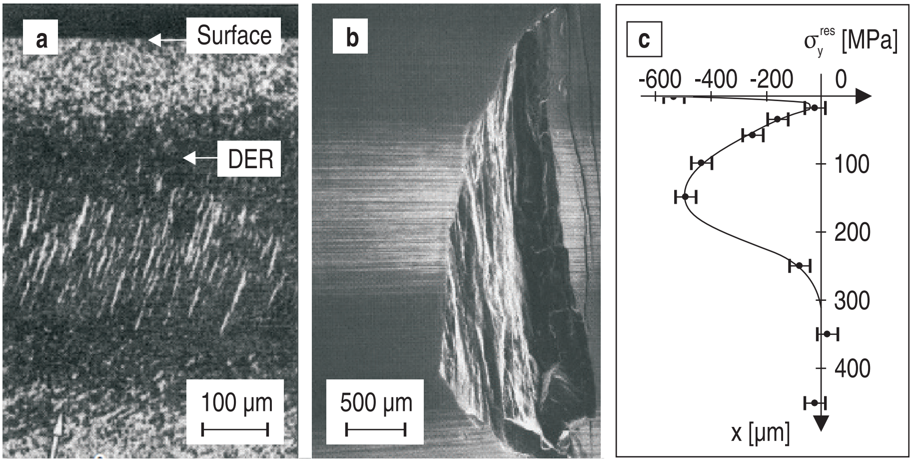

Figure 2.6: Subsurface failure mode (overrolling from left to right): alterations of the microstructure below the raceway surface (**a**), a spall on the raceway surface (**b**) and XRD analysis of the residual stresses below the raceway surface (**c**) (adapted from Ref. [28]).

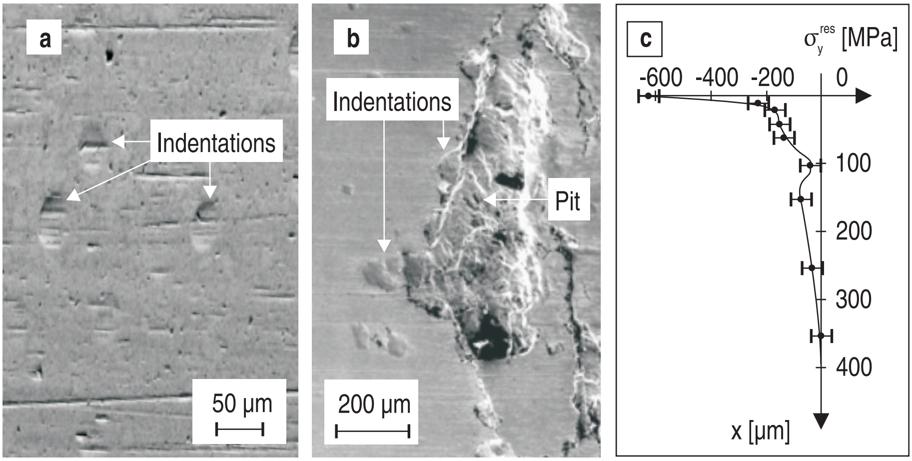

Figure 2.7: Surface failure mode (overrolling from left to right): indentations on the raceway surface (**a**), a V-shaped pit on the raceway surface (**b**) and XRD analysis of the residual stresses below the raceway surface (**c**) (adapted from Ref. [28]).

accelerated wear. While a small amount of wear is natural and unavoidable in most bearing arrangements, inadequate sealing and defective lubrication lead to severe wear. The bearing fails prematurely due to RCF initiated at the surface.

X-ray diffraction (XRD) allows measuring the material residual stresses based on the material strain. Changes in the width of the α-Fe{211} diffraction line reveal the material strain. To analyse the residual stresses at different depths below the raceway surface of a bearing, thin layers are removed with high precision through electrochemical polishing. The residual stresses are measured in parallel planes below the surface, in both the rolling direction (y-direction) and the axial direction (z-direction). These directions correspond to principal axes (Sect. 2.1.2). Similar depth distributions of the residual stresses in the rolling and axial direction are generally observed and the residual stresses are always negative [115].

After the bearing has failed, the damage initiation mechanism can be identified. Firstly, microscope images reveal damage of the raceway surfaces. Secondly, XRD analyses reveal the residual stress distribution below the raceway surfaces. The maximum residual stresses are found at a depth where most of the material aging occurred.

The subsurface failure mode is characterised by deep spalls on the raceway surface (Fig. 2.6**b**). Also, the maximum residual stress is measured below the surface. Fig. 2.6**c** shows an example of the residual stresses measured in the rolling direction σ_y^{res} after subsurface initiated bearing failure [28].

The surface failure mode is characterised by V-shaped pits behind indentations on the raceway surface (Fig. 2.7**b**). Also, the maximum residual stress is measured at the surface. Fig. 2.7**c** shows an example of the residual stresses measured in the rolling direction σ_y^{res} after surface initiated bearing failure [28].

2.4.2 Lifetime calculation

Accurate prediction of the lifetime of rolling element bearings is a crucial step towards a reliable design of many rotating machines. The general lifetime calculations are based on the assumption that the rolling surfaces flake sooner or later due to RCF initiated below the surface (subsurface failure mode). According to the classical fatigue theory, the first cracks usually emanate from inhomogeneities in the material, such as microscopically small inclusions or metallurgical dislocations. In recent years, inhomogeneities in the bearing material became less important as a cause of fatigue damage, owing to the constant improvement of the material cleanliness. Today, most cracks emanate from indentations caused by solid particles (surface failure mode). The inhomogeneities are randomly distributed in the material and vary in size and type. The solid particles vary in size and may enter rolling contact areas at an earlier or later time. With identical bearings and operating conditions, fatigue damage therefore occurs after different periods of operation. Ref. [7] describes a series of lifetime tests. Thirty bearings of the same batch are loaded in the same way till failure. Differences in lifetime up to a factor 20 are observed.

The wide scatter of running times explains the impossibility to accurately predict the lifetime of an individual bearing. Predictions can only be made for a large group of nominally identical bearings stressed in the same manner. The rating life L_{10} is defined as the running time at which 10% of the bearings have failed. The ISO 281 [56] standard gives the general equation for lifetime calculations, used for bearing dimensioning:

$$L_{10} = \left(\frac{C}{P}\right)^p \tag{2.22}$$

In this equation, P is the equivalent dynamic load which takes into account both the radial and axial bearing load. The dynamic load rating C corresponds to a pure radial constant load at which the L_{10} life equals 1 million revolutions. The exponent p equals 3 for ball bearings. The rating life L_{10} is expressed in million revolutions.

When a bearing is not stressed beyond its endurance strength limit and the operating conditions meet certain prerequisites with regard to the lubricant film thickness and cleanliness of the lubricating gap, it does not fail. Also, the bearing life not only depends on the load. Other influences, such as the lubrication condition, have a significant effect. These aspects are not taken into account by Eq. 2.22. However, the equation remains the basis of bearing dimensioning and the starting point for adjusted calculation methods. Since the 1970s, empirical factors are added to the equation, considering the endurance strength limit, the lubrication condition, etc.

In many bearing arrangements, the load and rotational speed change either randomly or according to a work cycle. An equivalent dynamic load is then calculated based on a series of individual loads and speeds of a certain duration q_i. This calculation is derived from the Palmgren-Miner rule of variable amplitude loading in the classical fatigue theory. With the rotational speed n_i when the load P_i is acting on the bearing and the mean rotational speed n_m, the equivalent dynamic load equals:

$$P = \left(\frac{\sum_{i=1}^{k} n_i q_i P_i^p}{n_m} \right)^{1/p} \tag{2.23}$$

2.4.3 Effect of external dynamic loads

In a number of bearing applications, failure analyses point to external machine vibrations as a cause of service life reduction. For instance in wind turbines, fans and paper making machines, the rolling element bearings are susceptible to this kind of failure. Elaborate research on this effect has been conducted by Gegner and Nierlich [28, 29, 30, 77]. The influence of external dynamic loads is analysed using a novel bearing test rig.

The test rig of Gegner and Nierlich allows applying controlled uni- to triaxial vibrations in the radial, axial and tangential direction. Eccentric drives generate the pure sinusoidal load. The test bearing is a cylindrical roller bearing. The static load introduces Hertzian contact pressures up to 2000 MPa on the outer ring, representing a realistic and common loading condition of the bearing. Axial vibrations at 100 Hz are applied while the bearing rotates at 600 r/min. The excitation represents typical engine vibrations acting on an operational bearing, e.g. from adjacent machines. The lipless outer ring of the test bearing is axially displaced and experiences high vibrational loads via the sliding contact of the rollers. The outer ring thus becomes the specimen. The raceway surface of the outer ring is analysed after 10^7 inner ring revolutions of this accelerated lifetime test.

The axial vibrations of the outer ring lead to sliding motion between the asperities of the bodies in contact. Here, the coefficient of friction μ between both bodies can locally exceed 0.3. As the coefficient of friction is much lower in the other subareas of the contact, this effect is also referred to as mixed friction. Due to the sliding motion, additional tangential loads are introduced on the surface. The tangential loads shift the maximum von Mises equivalent stress either closer to or directly on the surface, as shown in Fig. 2.3. Material aging is shifted towards the surface despite almost indentation-free raceways. Also, the von Mises equivalent stresses increase and material aging is accelerated.

Four indicators of failure due to external dynamic loads are investigated:

- A peak of the residual stresses near the surface is detected using XRD analysis. Material aging is shifted towards the surface. Fig. 2.8**b** shows an example of the residual stresses measured in the rolling direction σ_y^{res} after 10^7 inner ring revolutions of an accelerated lifetime test [77].

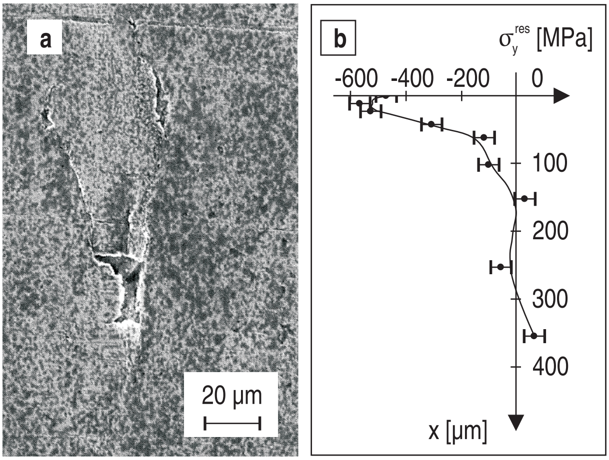

Figure 2.8: Effect of external dynamic loads: first surface cracks on a smoothed raceway surface (**a**) and XRD analysis of the residual stresses below the raceway surface (**b**) (adapted from Ref. [77]).

- A smoothed honing structure and polishing wear are observed using a microscope. While material aging is shifted towards the surface as in case of the surface failure mode, no indentations and pits are detected. Instead, polishing wear shows up as surface induced cracks and material delamination. The first surface cracks and material delamination occur after 10^7 inner ring revolutions of an accelerated lifetime test. Fig. 2.8**a** shows a smoothed raceway surface revealing the first surface cracks [77].
- An increasing temperature of the outer ring reflects frictional power loss due to vibrational loads.
- Acidification (oxidation) of the lubricant due to aging is observed [66].

The L_{10} calculated bearing life (Sect. 2.4.2) does not incorporate polishing wear due to external dynamic loads. As XRD analysis allows accurate estimation of the stage of material aging, the reduction of the bearing life due to external dynamic loads can be evaluated. A decrease of the L_{10} bearing life of 80% is estimated by Gegner.

In other accelerated lifetime tests, a radial dynamic load is added to the axial excitation. Radial vibrations such as oscillating changes of the Hertzian contact pressure can enhance the damaging effect significantly. Rolling element bearings in wind turbine gearboxes normally operate under moderate contact pressures

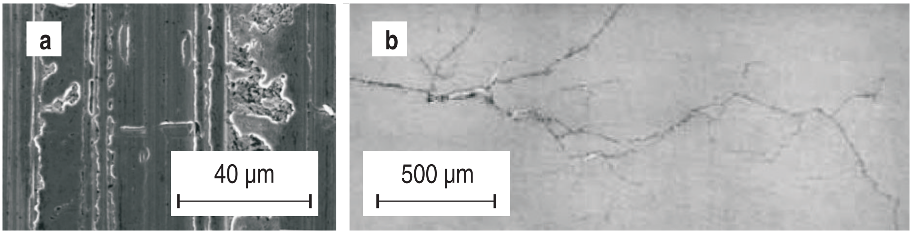

Figure 2.9: Example of grey staining (**a**) and a white etching crack (**b**) (adapted from Ref. [28]).

from 1200 to 1600 MPa. Impact events (starting and braking, emergency stops, etc.) introduce short-time peak loads of the Hertzian contact pressure up to 2500 MPa [30]. The stronger effect of these multi-dimensional vibrations is observed using XRD analysis.

Gegner relates the applied external dynamic loads to different other observations of surface damage. Two dominant effects are:

- Grey staining (Fig. 2.9**a**).

  Grey staining is well-known as surface damage on tooth flanks of gears. This type of dense micropitting occurs under mixed lubrication where the EHL film thickness is of the same order as the average surface roughness. Collisions between asperities on opposing surfaces cause elastic or plastic deformation, depending on the severity of the local loads. In addition to the contact stresses caused by normal loading, sliding between gear teeth causes tractive forces that subject asperities to shear stresses. During cyclic loading, plastic deformation accumulates and micropits are formed. The accuracy of the gear tooth geometry degrades, causing noisy gears and creating dynamic loads which can lead to gear tooth failure [96].

  Mixed friction in the contacts of a rolling element bearing can also cause grey staining. This micropitting typically initiates along the honing marks and along small cracks on the surface, as a further damage evolution of the polishing wear. Shallow material fractures of only a few micrometers in depth cover substantial parts of the affected raceway, resulting in a grey surface. An example is given in Fig. 2.9**a**.

- White etching cracks (Fig. 2.9**b**).

  The premature bearing failure mode known as white etching cracks (WEC) is characterised by the formation of heavily branching systems of cracks with borders partly decorated by a white etched microstructure. This failure mode is also called brittle, short-life, early, abnormal or white structured flaking [106].

Premature failure is observed within a considerably reduced running time of 1% to 20% of the L_{10} bearing life. Rolling contact fatigue is thus excluded as a potential root cause. After failure, cracks with a length of 1 to 20 mm have formed along the raceways. WEC is mostly observed in wind turbine applications. Occasionally, it is seen in industrial applications such as paper mills, continuous variable drives, marine propulsion systems, crusher mill gearboxes or lifting gear drives. An example is given in Fig. 2.9**b**.

The causes of WEC are heavily discussed and independently investigated by wind turbine manufacturers, gearbox manufacturers, bearing suppliers and universities. To this day, a consistent theory does not exist. The influencing factors are listed by Holweger [52]:

- Material: microstructure, heat treatment, natural hydrogen content, cleanliness, residual stresses, etc.
- Load: overloads, peak loads, impact loads, torque reversals, vibrations, slip, structural stresses, electric currents, etc.
- Environment: lubricant, additives, corrosion, tribochemical effects, hydrogen generation, temperature gradients, contamination, etc.
- Other: mounting, transport, quality aspects, etc.

The fact that most factors are correlated further increases the complexity. Gegner argues that mixed friction in sliding contacts induces this type of cracking. A full description of his reasoning is given in Ref. [28]. Wind turbine gearboxes are susceptible to WEC, as the operational conditions (load, speed and lubrication) are highly varying.

2.5 Conclusion

While the dynamics of spindles are widely discussed in the literature, the influence of the lubricant film on the bearing dynamics is not. A few studies compare the dynamic behaviour of dry and lubricated bearings. Wijnant establishes the first numerical formulations for stiffness and damping evaluation of EHL contacts. An increase of stiffness due to the formation of a lubricant film is observed. Dietl and Mitsuya experimentally analyse the bearing damping using specific test rigs. An increase of damping due to the formation of a lubricant film is observed.

Relations between the lubricant film behaviour and the bearing dynamics under varying speeds and temperatures are lacking in the current literature. In the work of this manuscript, the lubricant film behaviour and bearing dynamics are simultaneously identified using a novel test rig. Clear relations between both are revealed.

The influence of external dynamic loads on the lifetime of bearings is elaborately analysed by Gegner and Nierlich. Cylindrical roller bearings are tested under high dynamic load. Due to axial vibrations, asperities of the contacting bodies experience strong sliding motion. Material aging is shifted towards the surface. This type of damage is not covered by the classical bearing lifetime calculations. Reductions of the actual lifetime of 80% w.r.t. the calculated lifetime are estimated.

In the work of this manuscript, the effect of external dynamic loads is further investigated using a novel test rig. The behaviour of the lubricant film under high dynamic load is revealed. This behaviour is not described in the current literature. Also, surface wear due to external dynamic loads is analysed.

Chapter 3

Bearing test rig

To experimentally analyse the dynamic behaviour and lifetime of a rolling element bearing, a test rig is required.

The test rig should allow testing different types and sizes of bearings. The test bearings are small bearings with an outer diameter up to 52 mm. This, to limit the extent of the test rig and to restrict the duration of lifetime tests.

The test rig should allow applying a combined multi-axial static and dynamic load on the test bearing. In this way, real-life conditions can be simulated. The aim to apply a load as if the bearing is built into a real machine dictates the boundaries for the static and dynamic load. A static load up to 10 kN should be generated in both the radial and axial bearing direction. A dynamic load from 25 to 500 Hz with an amplitude up to 10% of the static bearing load should be generated in each direction. As bearings are mostly excited between 25 and 500 Hz in practice, this frequency range is of particular interest [49].

The test rig should allow measuring the bearing behaviour. The following sensors should be mounted:

- Five accelerometers for identification of the bearing dynamic behaviour.
- Three proximity probes for identification of the bearing motion.
- One thermocouple for measurement of the bearing temperature.
- Two ICP load cells for measurement of the applied dynamic load.
- An electrical circuit for measurement of the electrical resistance through the bearing.

To obtain clean measurement with maximum repeatability, noise from other components (i.e. support bearings and motor) and external influences (i.e. temperature effects and structural resonances) should be reduced as much as possible. Since bearings are very precise machine components, their behaviour can only be measured in an accurately controlled environment. Otherwise, noise from other components and external influences dominate the measurements [72].

Sect. 3.1 first presents the three unique features, the concept and the overview of the test rig. The test rig operation is described in Sect. 3.2. Sect. 3.3 discusses the identification of the bearing motion, the bearing dynamics and the lubricant film behaviour. Sect. 3.4 reviews the acquisition of the sensor data and the control of the actuators and motor.

The specifications of the different components are listed in the following appendices:

- Appendix A: Specifications of the actuators and motor;
- Appendix B: Specifications of the sensors;
- Appendix C: Specifications of the mechanical components.

3.1 General description

This section introduces the bearing test rig. The features, concept and overview are discussed.

3.1.1 Unique features

The test rig is characterised by three unique features:

1. Easy adjustment to test different types and sizes of rolling element bearings.

   The test rig allows easy adjustment to test rolling element bearings of different types, such as deep groove ball bearings and tapered roller bearings. They are also bearings of different sizes, with:

   - an inner bore diameter varying from 10 to 19 mm;
   - an outer diameter varying from 20 to 52 mm;
   - a width varying from 5 to 15 mm.

In this way, commonly used rolling element bearings, for example from electric motors and gearboxes, can be tested.

Depending on the selected bearing, the bearing manufacturer states a set of guidelines to determine the appropriate fits of the shaft and housing seat. Also, the required dimensional tolerances, tolerances for the cylindrical form of the seats and tolerances for perpendicularity of the abutments are provided. Using the test rig, each different bearing is mounted in a modular structure adapted to the specifications provided by the bearing manufacturer.

Precise alignment of the bearing mounting is guaranteed and replacement of the test bearing is easily done. The housing of the bearing is sealed, ensuring proper lubrication and relubrication with grease. Allowing easy mounting of different types and sizes of rolling element bearings makes this test rig unique in a first way.

2. Multi-axial static and dynamic loading of the test bearing.

   The test rig allows multi-axial static and dynamic loading of the test bearing. The bearing load is applied in both the radial and axial direction, and has a static and dynamic component in both directions. All components of the load are controlled separately. In this way, it is possible to simulate different real-life conditions where i.e. gear meshing forces are acting on the bearing.

   In the literature, many different designs of bearing test rigs have been proposed. Most of these set-ups are able to apply a static load on a bearing using for example hydraulics or springs. Some excite the bearing in its radial direction [71, 78, 111], some in its axial direction [53] and some in both directions [14, 108]. Bearing manufacturers even offer these types of test rigs allowing the costumers to test the quality of the grease they are using. Other types of test rigs load the bearing using an unbalance weight on a shaft [9] or through a set of gears using a gearbox [90, 94]. The latter rigs can be used to validate techniques developed to detect bearing damage in signals dominated by gear meshing noise. For the sake of completeness, the four-ball [60, 91] and five-ball [126] rolling contact fatigue test rigs are mentioned here as well. These rigs are commonly used to investigate friction and surface wear in the contact area. Only one rolling element of the bearing is being examined. The results are afterwards extended to the system level of an entire bearing.

   Two bearing test rigs are particularly interesting in the context of this work. At the National Renewable Energy Laboratory (NREL) [4], a test apparatus allowing experimental identification of the full 6x6 stiffness matrix of the test bearing is being developed. This research is driven by the lack of knowledge concerning the full stiffness matrix in the pubic domain. Secondly, Nierlich and Gegner [77] present a novel test rig allowing to introduce radial, axial and tangential vibrations on a test bearing. Accelerated lifetime tests under high dynamic load are performed, as discussed in Sect. 2.4.3.

Although many research projects conducted in the past use bearing test rigs, none of the rigs are able to apply a fully controlled multi-axial static and dynamic load on the bearing. The test rig proposed in this work is therefore unique in a second way.

3. Simultaneous measurement of the bearing motion, the bearing dynamics and the behaviour of the lubricant film.

   The test rig allows simultaneous measurement of the bearing motion, the bearing dynamics and the behaviour of the lubricant film. The bearing motion is measured using capacitive proximity probes, free from disturbances of the surrounding structure. The bearing is mounted on a smoothly running spindle and decoupled from the environment through bushings supporting the test rig. The bearing dynamics are measured using accelerometers, in a frequency range below the resonances of the surrounding structure's flexible modes. The structure is designed to be free of resonances in the frequency range of interest, from 25 to 500 Hz. The behaviour of the lubricant film is analysed based on the electrical resistance through the bearing. The bearing is electrically isolated from its environment such that its resistance can be measured.

   In the literature, test rigs for studying one of these properties are well described. For instance, Refs. [34, 107] present rigs used to analyse the dynamics of a bearing, while Refs. [48, 81] describe rigs developed to analyse the lubricant film of an isolated bearing. Monitoring the bearing motion is a commonly used technique for bearing diagnostics. Allowing simultaneous measurement of the different properties makes the current test rig unique in a third way. Relations between the bearing motion, the bearing dynamics and the behaviour of the lubricant film can be derived experimentally.

3.1.2 Concept and overview

The general principle of a bearing test rig is fairly simple. A load is applied on a test bearing, which is mounted on a shaft and driven by an electric motor. To counteract the load, at least two other bearings support the shaft. The load can be directly applied on the stationary outer ring or indirectly applied on the rotating inner ring. These two possibilities can be chosen for the radial and axial

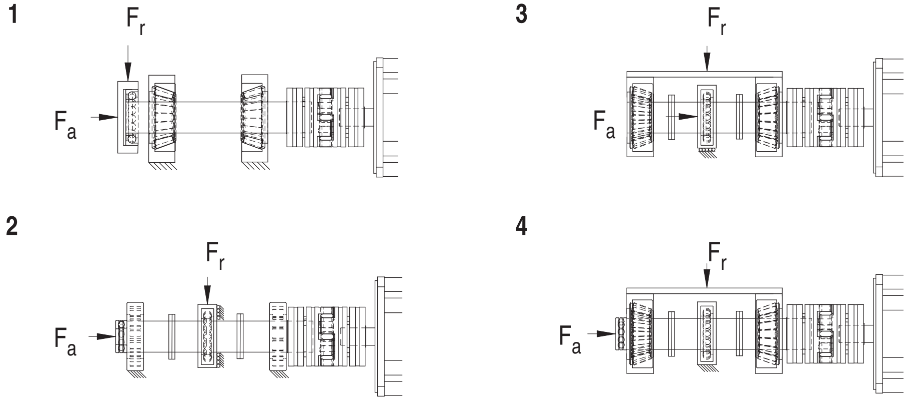

Figure 3.1: Concepts of a bearing test rig. The radial load F_r and axial load F_a can be directly applied on the stationary outer ring or indirectly applied on the rotating inner ring.

component of the load separately, resulting in four different concepts. Fig. 3.1 shows these concepts schematically. In concept 1, both radial and axial load are applied directly on the outer ring of the test bearing. The test bearing is located at the end of a cantilever shaft supported by two bearings. In the other concepts, the test bearing is located between two support bearings. Concept 2 uses a thrust bearing to transfer the axial load on the inner ring, whereas concept 3 shows how the radial load can be indirectly introduced. Finally, concept 4 combines the previous two concepts.

Concept 1 has four advantages compared to the others:

- The static and dynamic component of the load on the test bearing can be measured at the point where they are introduced. This in contrast with the other concepts, where the radial and/or axial load is indirectly applied on the inner ring through other bearings. The transferred dynamic load is influenced by the dynamics of these intermediate bearings and cannot be measured.
- Mounting and dismounting of the test bearing are easily done. The test bearing is simply slid of the shaft. In concept 2 to 4, the test bearing is located between two support bearings. A mechanism to dismount the middle part of the shaft is required.

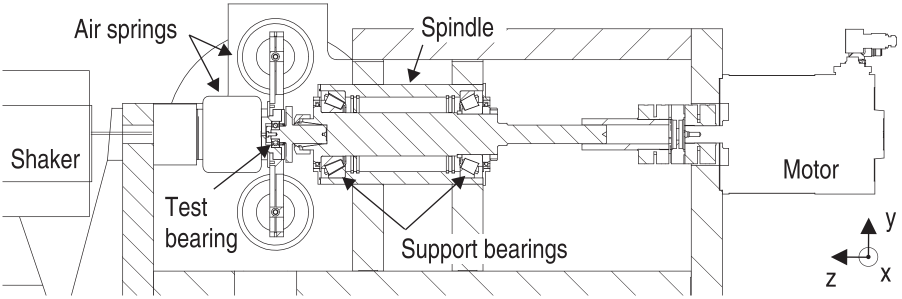

Figure 3.2: Cross-section of the test rig.

- No guiding system to restrict certain movements of the test bearing is necessary. In concept 2, the axial movement of the outer ring is restricted in order to apply an axial load. In concept 3, the radial movement of the outer ring is restricted. These guiding systems complicate the design. Also, a small amount of friction in their guiding direction leads to coupling between the radial and axial load.
- Using a set of axially preloaded support bearings, a stiff and smoothly running construction is obtained. The other concepts do not allow building such a construction, as the middle part of the shaft is removable. Also, concept 2 to 4 require an additional thrust bearing and/or guiding system. These sources of mechanical noise disturb the test bearing measurements.

Based on these advantages, the presented test rig is derived from concept 1. Fig. 3.2 shows a cross-section of the test rig. The support bearings are mounted in a cylindrical housing, forming a spindle similar to the spindle of milling machines. The test bearing is located at the end of the shaft and mounted in a housing. Air springs directly apply a radial and axial static load on the test bearing housing. Electrodynamic shakers provide the dynamic load in the radial and axial direction.

One particular concern arises when adopting concept 1. The radial bearing load is imposed on a cantilever shaft, introducing a possible tilt angle between the inner and outer ring of the test bearing. This tilt angle influences both the dynamics and the lifetime of the test bearing. To reduce bending of the shaft, the spindle is optimised for maximum bending stiffness. The shaft is supported by two tapered roller bearings (TRB) mounted in O-arrangement and preloaded in the axial direction (Sect. 3.2.1). Furthermore, the housing of the test bearing is flexibly connected to the environment through air springs and shaker stingers. Even when the cantilever shaft bends, the radial actuators

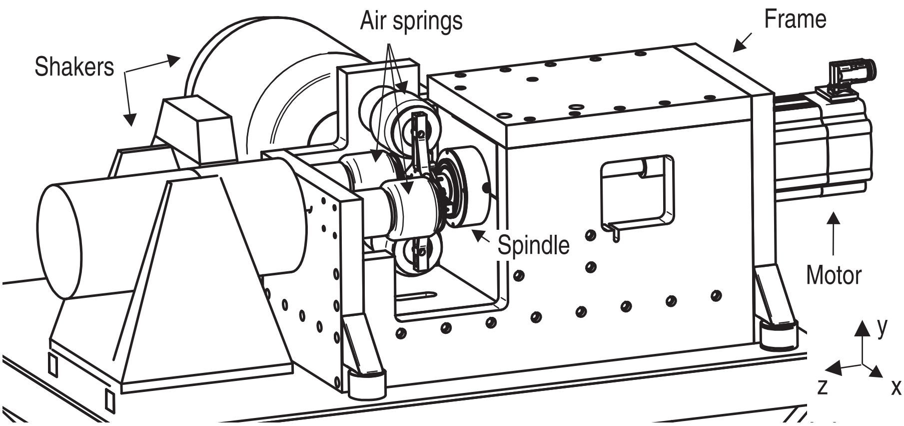

Figure 3.3: Overview of the test rig.

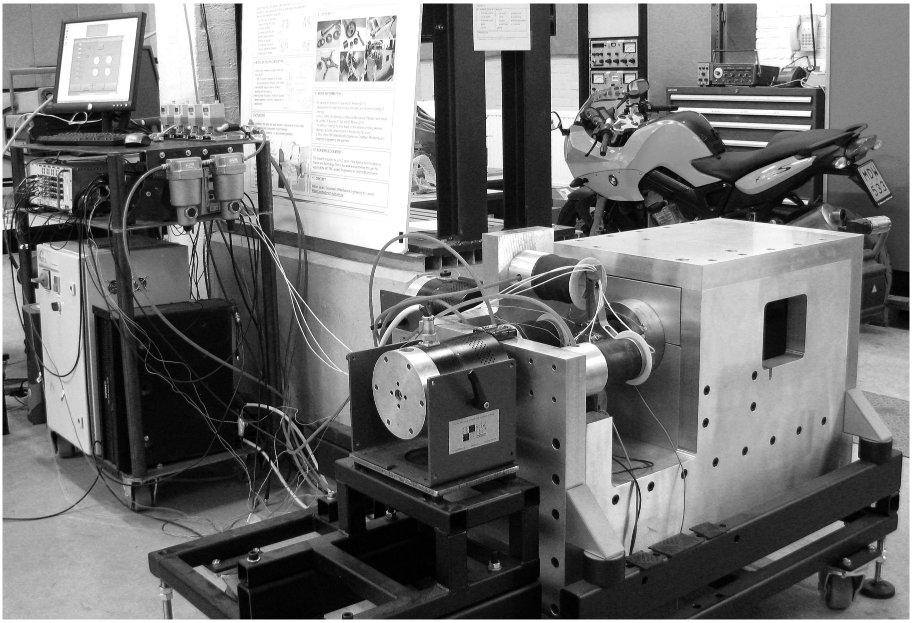

Figure 3.4: Picture of the test rig and its control unit.

apply a pure radial bearing load while the axial actuators apply a pure axial bearing load (Sect. 3.2.3). A possible tilt moment acting on the test bearing is negligible and accurate alignment of the outer ring w.r.t. the inner ring is guaranteed.

Fig. 3.3 and 3.4 give an overview of the test rig. The remainder of this chapter further reviews the design and implementation of the test rig.

3.2 Test rig operation

In this section, the test rig operation is extensively discussed. The bearing is mounted on a precisely running spindle. A modular mounting system surrounds the bearing and allows testing different types and sizes of bearings. The multi-axial static and dynamic load are precisely controlled.

3.2.1 Precise spindle motion

An ideal spindle allows motion in only one degree of freedom (DOF): pure rotation. Any movement in the remaining five degrees of freedom is undesired and may be classified as either an error or a response to an external influence. The error can result from the spindle's design and manufacturing, while the external influence can be thermal gradients or external vibrations. This section discusses the design of the spindle and the different techniques applied to limit both errors and external influences.

O versus X-arrangement

To support the main shaft of the test rig, two tapered roller bearings are mounted in opposition to each other and axially preloaded. Two types of adjustable bearing arrangements are considered: the O-arrangement (back-to-back) and the X-arrangement (face-to-face). Fig. 3.5 compares both arrangements.

Following Fig. 3.5, the contact lines of the rolling element forces intersect in the pressure cone apex S. The roller cone apex R is the point where the bearing centre line intersects the projection of the inclined outer ring raceway. The spread H defines the distance between the pressure cone apices S of the two bearings forming the O or X-arrangement. In the O-arrangement, the spread H is larger than in the X-arrangement. This results in a higher bending stiffness of the spindle when the O-arrangement is adopted.

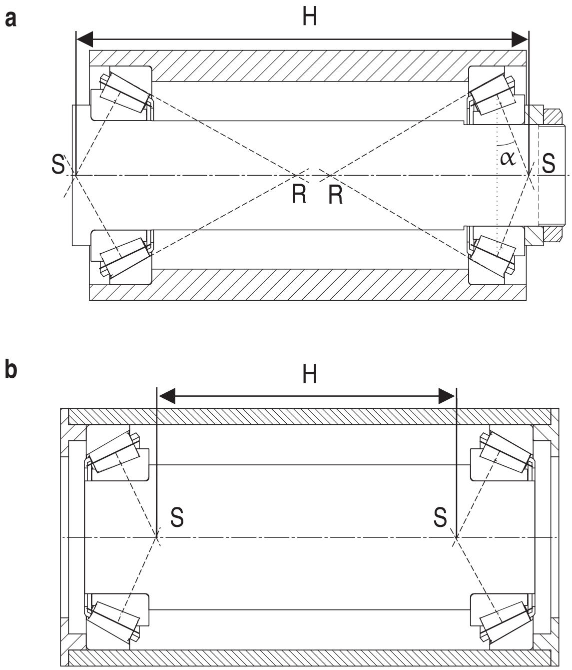

Figure 3.5: Two types of adjustable bearing arrangements: O-arrangement (**a**) and X-arrangement (**b**).

Heat, generated by friction in the rolling contacts of the bearings, is dissipated more easily through the housing than through the shaft. When the temperature of the bearings increases during operation, the shaft heats up and expands more than the housing in both radial and axial direction. In an O-arrangement, the radial preload increases while the axial preload decreases. If the roller cone apices R of both bearings coincide at one point, the resulting preload is unaffected. The adjusted preload is independent of the temperature. In an X-arrangement, both radial and axial preload increase when the temperature increases. The adjusted preload rises and possibly reaches a critical value.

As a higher bending stiffness and a preload which is independent of the operational temperature can be obtained, the O-arrangement is adopted in the spindle design of presented test rig.

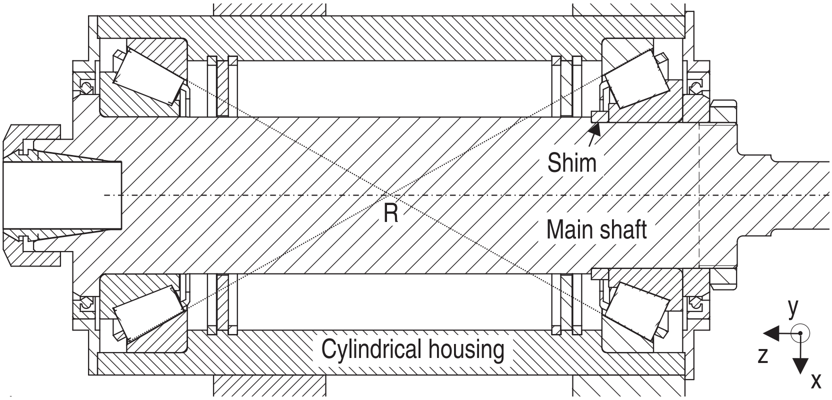

Figure 3.6: Cross-section of the spindle. Both bearings are mounted in the same cylindrical housing. The roller cone apices R of the two bearings coincide at one point. The preload is set based on the thickness of a shim.

Spindle design

Fig. 3.6 presents the design of the spindle. The tapered roller bearings are mounted in a cylindrical housing. The bearing seats are milled during the same operation to ensure a precise alignment between both bearings.

The contact angle of a tapered roller bearing α defines its axial load carrying capacity w.r.t. its radial load carrying capacity. As the bearings in this set-up are heavily loaded both in the radial and axial direction, a high contact angle of $30\,^{\circ}$ is chosen. Robust bearings with an outer diameter of 140 mm are selected. This is advantageous when a high bending stiffness of the spindle is desired. In Fig. 3.6, the left bearing is of the type TRB T7FC 070 and the right bearing is of the type TRB 31313 J2.

The distance between the two bearings is determined based on the condition that the preload is independent of the temperature. The roller cone apices R of both bearings coincide at one point when the distance between the two bearings equals 270 mm. Choosing this large distance between both bearings is advantageous in two additional ways. Firstly, the radial force on the bearings (due to a radial load on the test bearing) reduces such that the lifetime of the bearings increases. Secondly, the error angle of the shaft due to imperfect alignment of both bearings reduces.

Tapered roller bearings offer high load carrying capacity and high stiffness because of the line contact between the rollers and raceways. The tradeoff in performance is that these bearings typically have relatively large error motions. Geometrical errors in the rollers or raceways affect the rotation by the same internal stiffness that provides the favourable load capacity [72]. In comparison, air bearing spindles and hydrostatic spindles run with higher accuracy. A substantial increase in expense should be expected if a high load carrying capacity of these spindles is required. Ref. [18] shows an interesting implementation of a bearing test rig using wave journal bearings to support the shaft.

Setting the optimal preload

During mounting, an axial preload is introduced between both spindle bearings. The preload is set with a shim which accurately determines the distance between the inner rings of both bearings. Mounting the bearings with the right amount of preload has three advantages:

- The clearance in the bearings is removed. This ensures smooth running with high running accuracy [7].
- The stiffness of the support system increases [46]. Due to the preload force, all rolling elements are now loaded forming a stiffer structure.
- The lifetime of the bearings increases. The preload serves to provide a minimum load on the bearing and prevent bearing damage as a result of sliding motion of the rolling elements [99].

When increasing the preload, the clearance in each bearing is reduced. At a certain point, the clearance is removed and all rolling elements are loaded. Further increase of the preload would only reduce the bearing lifetime. The optimal preload is determined in cooperation with the bearing manufacturer. Deriving the optimal preload and the optimal thickness of the shim is done in the following way:

1. The minimum preload force is determined based on the minimum bearing load which guarantees an operation without sliding. The TRB T7FC and TRB 31313 require a minimum preload force of respectively 2.6 kN and 2.3 kN to avoid sliding of the rolling elements.
2. The maximum preload force is set based on the required lifetime of each bearing. A preload force up to 15 kN on each bearing ensures continuous running of the bearings below their fatigue load limit (endurance strength limit).

3. Based on the minimum and maximum force, a desired preload force of 10 to 15 kN is chosen. An analytical relation between the axial load on the bearing and the resulting axial displacement allows converting the preload force to a required displacement of the inner ring relative to the outer ring. Using this relation for each bearing, a total desired preload of 30 to 40 µm is obtained.
4. The deformation of the cylindrical housing and the shaft due to the preload force is determined using a static finite element (FE) analysis of these components. When introducing a preload force of 10 to 15 kN, the distance between the outer ring seats reduces 1.3 to 1.9 µm. Analogously, the distance between the inner ring seats increases 5.6 to 8.4 µm.
5. The real geometry of the shaft and housing is measured with a coordinate measuring machine.
6. The thickness of the shim is given by the thickness resulting in zero preload (from step 5), subtracting the desired preload (from step 3) and subtracting a compensation for the deformation of the housing and shaft (from step 4).

Spindle lubrication

The bearings are lubricated with grease injected through grease nipples. The grease is contained in a compartment around each bearing, formed by a plate clamped between snap rings and a cover panel with a radial shaft seal.

Two thermocouples measure the temperature of the outer ring of each bearing during operation. The steady-state temperature at different speeds is summarised in Fig. 3.7. General purpose grease, consisting of mineral base oil and lithium soap, was initially used to lubricate the bearings. The grease failed to provide proper lubrication at high speeds. At 2400 r/min, the outer ring temperature of TRB T7FC reached the maximum allowed temperature of the lubricant. The temperature of the inner ring and lubricant exceeded this maximum. Replacement of the grease with high performance grease allows operation up to 3000 r/min. The polyurea (di-urea) thickener of this grease improves lubrication at high speed and high temperature.

Spindle motor

A synchronous servo motor is connected to the main shaft using a backlash-free jaw-type coupling. The rotational speed of the motor ranges from 0 to

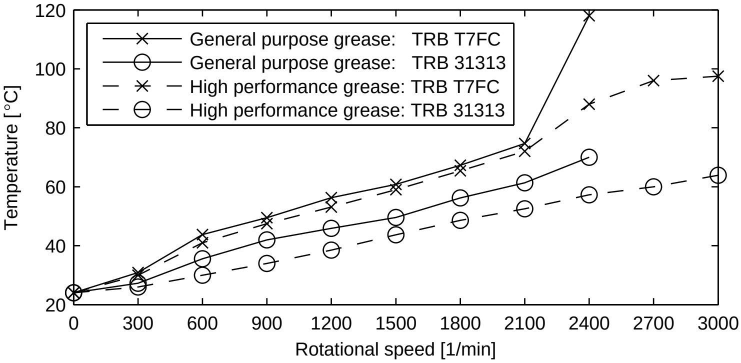

Figure 3.7: Temperature of the outer ring of the spindle bearings for two types of grease.

3000 r/min. The speed is precisely controlled in a feedback loop implemented in the motor controller. Run-up and run-down events can be simulated.

The coupling isolates the spindle from torsional vibrations generated by the motor. Also, the spindle shaft and motor are dynamically decoupled in the radial and axial direction. The rotor of the motor does not influence the dynamics of the shaft. The dynamics of the main shaft are further discussed in Sect. 3.3.2.

3.2.2 Modular mounting of the test bearing

In most cases, modularity and accuracy are opposing factors during a design. As the modularity increases, more parts are used and the stiffness of the structure decreases. Aligning all components becomes more difficult. This test rig allows mounting different types and sizes of bearings while precise alignment with the spindle is guaranteed. The test bearing is mounted in a modular structure consisting of an auxiliary shaft and an intermediate sleeve. A cross-section is given in Fig. 3.8.

The test bearing is mounted on the auxiliary shaft adapted to its bore diameter. The auxiliary shaft is clamped in the spindle of the test rig using a mechanism called collet chuck. After inserting this auxiliary shaft, the locknut is tightened. In milling machines, the same principle is used to clamp the tool into the spindle. Since bending of the spindle in response to radial cutting forces is inadmissible, the collet chuck is designed to form a stiff connection between the spindle and the tool. Both shafts are precisely aligned because of the tapered shape of

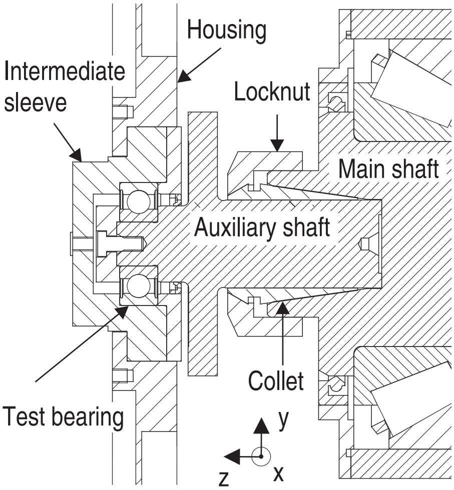

Figure 3.8: Components of the modular mounting system of the test bearing. The test bearing is mounted on an auxiliary shaft and mounted in an intermediate sleeve, adapted to its dimensions.

the mating parts. The test rig uses DIN 6499 ER-40 collets to clamp shafts with an outer diameter up to 30 mm. The tapered cavity in the main shaft is manufactured according to DIN 69871 [21] specifications. This standard specifies the geometry of the cavity and the required manufacturing tolerances.

The housing of the test bearing is adapted to the test bearing using an intermediate sleeve. The bore diameter of the sleeve is adjusted to the outer diameter of the test bearing. A different sleeve is installed when a different bearing is tested.

The bearing manufacturer states a set of guidelines to determine the appropriate fits of the shaft and housing seat depending on the selected bearing. Also, the required dimensional tolerances, tolerances for the cylindrical form of the seats and tolerances for perpendicularity of the abutments are provided. All of these conditions can be taken into account for each bearing, as the auxiliary shaft and intermediate sleeve are tailored to a specific test bearing. Both the auxiliary shaft and intermediate sleeve are made of steel and regular fits of the shaft and housing seat are used. The fits are unaffected by variations of the temperature during operation of the bearing as the shaft, the sleeve and the bearing rings have the same coefficient of thermal expansion.

3.2.3 Multi-axial static and dynamic loading

The test rig allows applying an independently controlled load in the radial and axial direction. No coupling between the radial and axial force is allowed. The load has a static and dynamic component in both directions. In this way, it is possible to simulate different real-life conditions where i.e. gear meshing forces are acting on the bearing. This section presents the actuator configuration.

Actuator selection

The static actuators should provide a high static force with a limited stroke. Most of the test rigs discussed in the literature use hydraulics to generate the static force. The presented test rig uses a pneumatic circuit instead, with sleeve type air springs to provide the force and electro-pneumatic regulators to control the force. A sleeve type air spring consists of two parallel plastic disks, connected through a rubber sleeve. The range of the force is determined by the static load rating of a series of possible test bearings. The maximum enforced radial and axial static load are set at 10 kN.

The dynamic actuators should provide a broadband dynamic force. The presented test rig uses electrodynamic shakers to generate the dynamic force in a frequency range from 0 to 5000 Hz. The maximum enforced dynamic load is set at 10% of the applied static load. This makes it possible to simulate a load on the bearing as if it were built into a real machine.

Actuator configuration

Fig. 3.9**a** gives an overview of the actuator configuration. In Fig. 3.9**b**, the actuators are replaced by force vectors, providing a clear view on the design of the bearing housing. The bearing is radially loaded in the x-direction and axially loaded in the minus z-direction. The static load is applied by four air springs transferring their force to the bearing. Two air springs generate the axial force $F_{a,st}$ and two air springs generate the radial force $F_{r,st}$. The dynamic load is directly introduced on the bearing housing through stingers, connecting the electrodynamic shakers to the housing. One shaker generates the axial force $F_{a,d}$ and one shaker generates the radial force $F_{r,d}$.

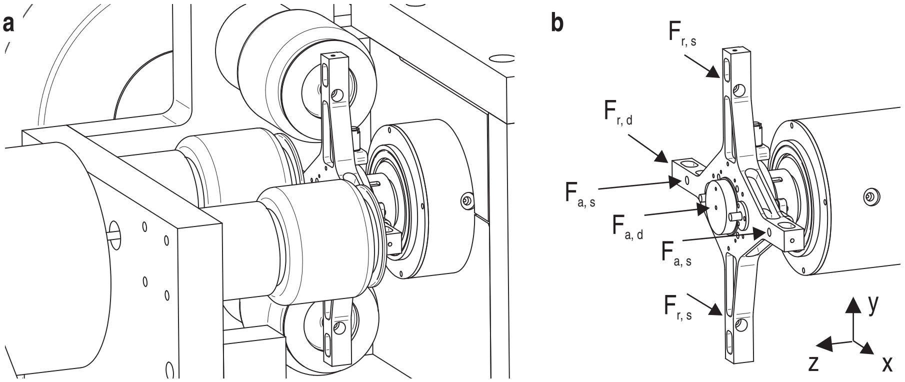

Figure 3.9: Actuators (**a**) and their corresponding force vectors (**b**) of the test rig.

Magnitude of the load

The air spring pressure is controlled in a feedback loop implemented in the electro-pneumatic regulator. The spring is initially calibrated to determine the relation between the air pressure and the delivered load. It is mounted in a stiff structure and connected to a load cell. The set-up is presented in Fig. 3.10**a**. Fig. 3.10**b** shows the relation between the air pressure and the delivered load for two different springs. This relation is used to set the air pressure based on the requested bearing load. Accurate control of the bearing load is guaranteed, as only differences up to 0.5% of the delivered load are measured when repeating the same calibration test. Variations up to 4% of the delivered load are measured when comparing the different springs. Each spring is controlled with a separate regulator and a different relation is used for the different springs. A scheme of the air circuit is given in Fig. 3.21.

The shakers are driven by control signals, generated by the test rig control unit and sent to the shaker amplifiers. The actual dynamic load applied on the test bearing is measured with ICP load cells. They are mounted between each shaker stinger and the test bearing housing. Based on the actual dynamic load, the control signals are adjusted to obtain a desired dynamic bearing load.

Point of action of the load

To avoid an uncontrolled and unwanted tilt moment on the test bearing, the applied load acts through the centre of the bearing. The static actuators are

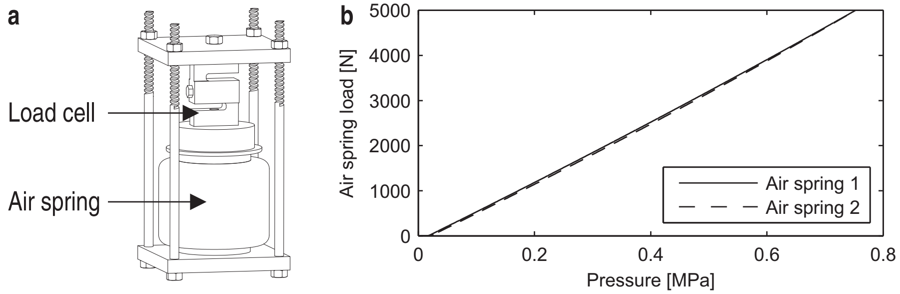

Figure 3.10: Set-up for calibration (**a**) and the relation between the air pressure and the air spring load of two different air springs (**b**).

positioned such that the resulting force vector in each direction acts through the centre of the bearing. The dynamic force acts in the centre of gravity (COG) of the excited structure surrounding the test bearing. The excited structure consists mainly of the housing and sleeve of the test bearing and the upper part of the air springs (Fig. 3.14**a**). During the design of the housing, computer aided design (CAD) software is used to balance the structure, such that its COG coincides with the centre of the bearing.

Full decoupling of the force components

The different components of the bearing load are fully decoupled and independently controlled:

- The static and dynamic load are decoupled.

  The longitudinal stiffness of the springs is small w.r.t. the test bearing stiffness. A mean value of 325x10^3 N/m is provided by the air spring manufacturer. In comparison, the average stiffness value of possible test bearings is 35x10^6 N/m in the radial direction and 3.5x10^6 N/m in the axial direction. The shaker excitation is transferred through the test bearing instead of the air springs.

- The radial and axial static load are decoupled.

  The lateral stiffness of the springs is negligible w.r.t. the longitudinal stiffness, with an upper limit of only 1% of the longitudinal stiffness. Consequently, the radial static load does not affect the axial static load and vice versa. This avoids a complex structure where the load is transferred through steel balls. Using steel balls is a commonly applied decoupling technique in test set-ups, since a ball located between two parallel plates can only pass a load acting through its centre.

- The radial and axial dynamic load are decoupled.

  The electrodynamic shakers are connected to the bearing housing through stingers. A stinger is a thin metal rod, stiff in its longitudinal direction and flexible in its lateral direction. Consequently, the radial dynamic load does not affect the axial dynamic load and vice versa.

Additional advantages of the actuator configuration

Besides decoupling of the force components, using air springs and shakers in the presented configuration to apply the load has three additional advantages:

- The small longitudinal and lateral stiffness of the air springs and the small lateral stiffness of the stingers lead to a floating configuration of the bearing housing. Even when the cantilever shaft bends, the radial actuators apply a pure radial bearing load while the axial actuators apply a pure axial bearing load. A possible tilt moment acting on the test bearing is negligible, such that accurate alignment of its outer ring w.r.t. its inner ring is guaranteed.
- To minimise the inertial forces during dynamic excitation, the total mass excited by the shaker should be small. The structure excited by the shaker is shown in Fig. 3.14**a**. The part of the air spring connected to the housing is included in this structure. The mass of the air spring part is limited to 0.12 kg, making this type of actuators more interesting than for example hydraulic actuators.
- During operation of the test rig, the test bearing and spindle bearings heat up and the shaft expands. The force delivered by the air springs only depends on the air pressure in the circuit. This air pressure is controlled by regulators and is independent of thermal expansion of the shaft. The coil of the shakers is free to move longitudinally in its armature. The force delivered by the shakers is independent of thermal expansion of the shaft.

3.3 Test rig measurements

The test rig allows analysing the bearing motion, the bearing dynamics and the behaviour of the lubricant film. This section discusses the precise identification of these bearing properties using the presented test rig.

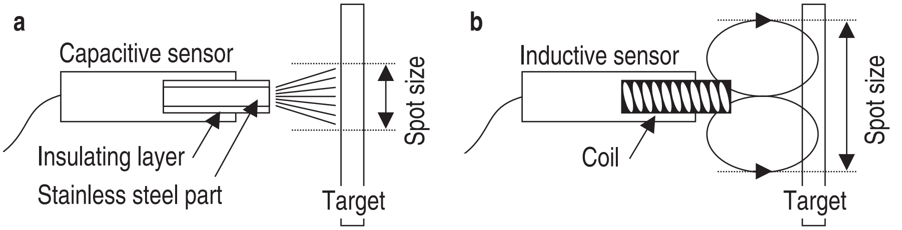

Figure 3.11: Comparison between a capacitive (**a**) and inductive (**b**) sensor.

3.3.1 Bearing motion

The radial, axial and tilt motion of the bearing are derived from three proximity probes. The probes measure the relative displacement between the inner and outer ring of the bearing at three different locations. After selecting the appropriate type of proximity probe, this section explains the precise mounting and use of the sensors in the test rig.

Inductive versus capacitive proximity probes

The two most important proximity probes applied in rotating machinery are capacitive and inductive sensors (Fig. 3.11). In order to choose the right type, the differences between both types are analysed:

- Principle.

  A capacitive probe consists of a small stainless steel part used to generate an alternating electric field between this steel part and a conducting target. An insulating layer around the steel part focuses the electric field on the target. The amount of current flowing in the electric field is determined by the capacitance between the sensing area of the probe and the target. As this capacitance is related to the distance between the two conductors, the current is a measure for the distance between both conductors.

  An inductive probe contains a small coil. Alternating current, passing through this coil, generates an alternating magnetic field. This magnetic field penetrates the target and induces eddy currents in the material. The eddy currents generate their own magnetic field which opposes the field of the sensor. The interaction between both fields is measured by the electronics of the sensor. As this interaction depends on the distance between the sensor and the target, the distance can be derived.

- Target size.

  The sensing field of the probe covers a certain area of the target, called the spot size. The electric field of a capacitive probe typically generates a spot size having a diameter which is 30% larger than the probe's diameter. The magnetic field of the inductive probe covers an area having a diameter which is typically three times larger than the probe's diameter. The magnetic field is more difficult to focus than the electric field of a capacitive probe. Good detection of the target requires that the target is larger than the spot size. Capacitive probes are thus best suited for a distance measurement relative to a small target [123].

- Target material.

  The electric field of a capacitive sensor uses the target as a conductive path to the ground. All conductive materials generate this path equally well, so the sensor output is independent of the target material. The strength of the eddy currents and the resulting magnetic field depend on the permeability and resistivity of the material. These properties are different for different materials. Inductive sensors should be recalibrated when measuring a different target material.

- Rotating targets.

  Inductive sensors generate a magnetic field which penetrates into the target material. If the target is a rotating shaft, the sensor output changes due to the variation of the imperfections in the material below the surface. Even with a perfectly round and centred shaft, this electrical runout is measured. This introduces an error of the order of 1 μm [123]. Capacitive sensors generate an electric field that does not penetrate the material. No electrical runout is present in the measured signals.

- Multiple sensors.

  When several capacitive sensors measure the same target, the electric field of one probe may try to add charge to the target while another sensor is trying to remove the charge. This creates an error, which should be avoided by synchronising the sensors. Synchronised sensors are driven with signals having the same phase. All probes add and remove charge at the same time. When the magnetic field of inductive sensors interact, an error is introduced which cannot be avoided.

- Gap contamination.

  Capacitive sensors measure the movement of a target based on a change in the capacitance between the sensor and the target. This capacitance depends on the dielectric constant of the medium between both conductors, which is assumed to be air. Contamination of the air gap changes the dielectric constant and introduces an error. Capacitive sensors can only be used in a clean environment. Measurements with inductive sensors are unaffected by nonconductive contaminants [123].

Mounting of the capacitive probes

Inductive sensors are often used for condition monitoring of industrial machines because of their lower price and their robustness in hostile environments. For precision measurements with the presented test rig, capacitive sensors are required. The space around the sensors is limited and the target size is small. If inductive sensors were used, the magnetic field of each sensor would interact with the magnetic field of other sensors and the surrounding structure. Also, the error due to electrical runout is unacceptable. The displacements measured by the sensors are very small due to a high bearing stiffness of the test bearing. Assuming a bearing with a radial stiffness of 10^8 N/m, a force of 100 N is required for a measured displacement of 1 μm. Since the electrical runout introduces errors of 1 μm, a variation of the bearing load of less than 100 N cannot be detected in the signals of inductive sensors.

Fig. 3.12 shows the positioning of the capacitive probes in the test rig. Three synchronised probes are mounted on the housing of the test bearing and pointed at a flange of the auxiliary shaft. One probe measures the radial bearing motion in the direction of the radial load (x-direction). The axial motion is given by the mean displacement of the two axial probes (z-direction). The tilt motion of the bearing around the y-axis is derived from the difference between the displacement of the two axial probes. Due to the large distance between the two axial probes of 90 mm, the tilt motion is accurately measured.

The probes measure the relative displacement of a target surface from their sensing area with an accuracy of 10 nm. In the presented test rig, the following measures are taken to obtain accurate data of the bearing motion:

- As the probes are mounted on a vibrating structure, tight clamping of the sensors is required. Each of the probes is mounted in a custom-made structure consisting of a sleeve, a nut and an o-ring (Fig. 3.12). The o-ring clamps the sensor without damaging its thin casing.
- As the probes are pointed at a rotating shaft, mechanical runout cannot be avoided. During rotation of the shaft around its centre axis, radial and axial mechanical runout of the target surface distort the signal. Radial runout is caused by deviations of the flange top surface from a true circle

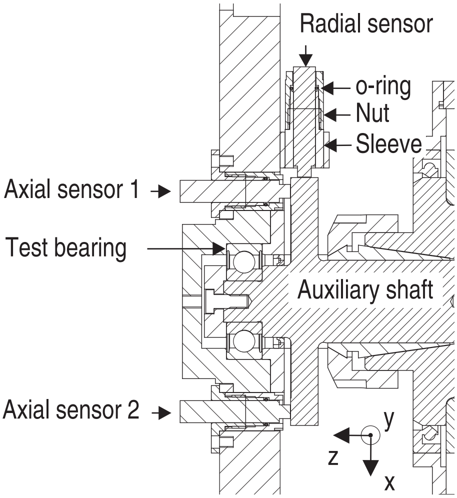

Figure 3.12: Positioning of the capacitive probes. One probe measures the radial bearing motion, while two other probes measure both the axial and tilt motion.

and includes low-frequency components such as eccentricity and out-of-roundness [89]. Axial runout is caused by deviations of the flange side surface from a flat surface, perpendicular to the axis of rotation. The error due to mechanical runout is reduced by applying a precise surface finish of the target surface. Both the bearing seat and target surface of the probes are ground during the same operation. A runout of less than 0.8 µm is achieved in both directions during rotation of the shaft around the bearing seat. If a higher accuracy is required, several costlier surface finish techniques are available. For example, the shaft can be coated with a 50 µm layer of nickel and turned with a diamond tool afterwards. A mirror finished surface with a runout of less than 0.1 µm is then obtained.

- Contamination of the air gap is avoided using a radial shaft seal between the test bearing and the measurement surface. The capacitive sensors are pointed at a surface which is never in contact with the grease of the bearing, not even while replacing the bearing. This ensures that the air gap is not contaminated.

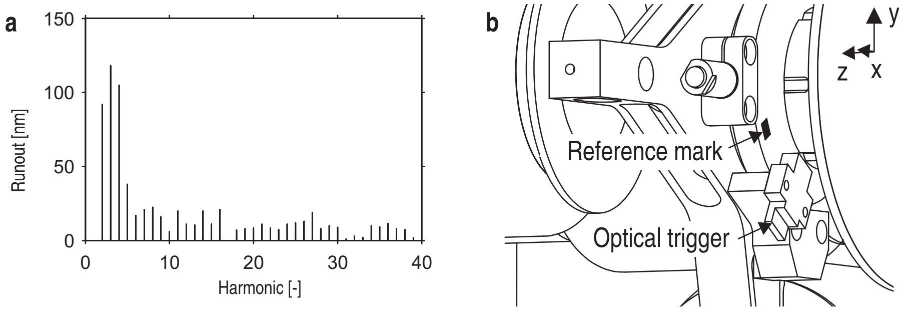

Figure 3.13: Actual radial runout of the target surface on the shaft (**a**). A reference mark on the shaft and an optical trigger are used to synchronise the actual runout and the measured signals (**b**).

Correction for mechanical runout

The error due to mechanical runout is limited as the target surface is precisely ground. The error is further reduced during post-processing of the test rig signals, by subtracting the actual runout from the measured signals of the capacitive probes. Synchronisation of the actual runout and the measured signals is done using a reference mark on the shaft and an optical trigger (Fig. 3.13**b**).

The actual runout of the target surface is initially characterised using a precise spindle supported by air bearings. The spindle has an error motion of less than 10 nm, which can be neglected in comparison to the runout of the target surface. The auxiliary shaft is clamped in the spindle at the bearing seat. Capacitive probes measure the actual runout while the shaft rotates around the bearing seat. The spectrum of the actual radial runout is shown in Fig. 3.13**a**. The second, third and fourth harmonic determine the radial runout.

3.3.2 Bearing dynamics

The test rig is designed to analyse the dynamic behaviour of a bearing in a range from 25 to 500 Hz. The measurements should not be affected by the dynamics of the surrounding structure. The three main structural components of the test rig, namely the housing of the test bearing, the spindle and the frame, are solid structures. They are optimised using FE software to analyse the bearing behaviour free of resonances of the test rig structure.

After assembly, experimental modal analyses of the three main components are performed to validate the FE analyses. During a modal analysis, a shaker dynamically excites the structure while the responses of the structure are measured with accelerometers. The sum of all measured frequency response functions (FRFs) is used to evaluate the dynamic behaviour. The highest peaks in this graph indicate the resonances with the largest total modal displacement. Small peaks indicate local modes with displacements at a limited number of degrees of freedom only [50].

This section discusses the dynamics of the three main structural components.

Housing of the test bearing

The housing of the test bearing is a solid structure transferring the forces of the four air springs to the bearing. To handle the static load up to 10 kN in each direction of the bearing, high strength of the housing is required. To minimise the inertial forces and maximise the resonance frequencies of the excited structure, low mass of the housing is required. It is made of DIN 1.2311 prehardened mould steel with a yield and ultimate tensile strength of respectively 821 and 1014 MPa. The stresses through the housing when applying the maximum air spring load are calculated based on a static FE analysis of the housing. A safety factor of 3 w.r.t. the FE calculated maximum stresses is applied during the design. The mass of the housing is limited to 1.7 kg.

The radial and axial shaker of the test rig excite the assembly consisting of the housing, the sleeve and the upper part of each air spring (Fig. 3.14**a**). The dynamics of this assembly are analysed using a three-dimensional (3D) FE model. The longitudinal and lateral stiffness of the air springs are small (Sect. 3.2.3) and neglected in this model. The upper part of each air springs is modelled as a point mass. The stiffness increase provided by the outer ring of the test bearing is neglected as well. In the final design, the first flexible mode of the assembly occurs at a resonance frequency of 695 Hz. The mode is presented in Fig. 3.14**b**.

To validate the FE calculations, a modal analysis is performed. The housing assembly is supported using flexible springs, approximating the free-free condition as defined in the FE calculations. Dummy masses represent the upper part of each air spring. Five accelerometers are mounted on the housing. Fig. 3.15 shows the sum of FRFs of this modal analysis. The first flexible mode appears at 618 Hz. The dynamic behaviour of a bearing can thus be analysed in a range from 25 to 500 Hz, free of resonances of the housing assembly.

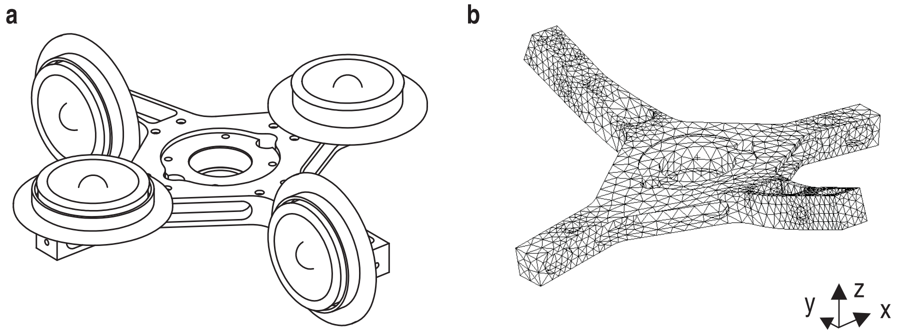

Figure 3.14: Assembly excited by the shaker (**a**) and its first mode (**b**).

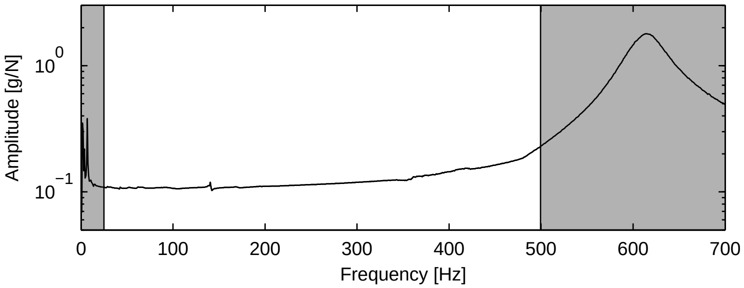

Figure 3.15: Sum of FRFs measured during the modal analysis of the housing assembly. The housing assembly is designed to be free of resonances in a range from 25 to 500 Hz (white area).

Frame of the test rig

The frame of the test rig supports the motor, the spindle and the static actuators (Fig. 3.16**a**). More importantly, it guarantees precise alignment between the motor and the spindle. It is made of milled aluminium plates. Dowel pins are positioned with strict tolerances between the panels of the frame, aligning the different parts. Due to the rigid connection between both spindle and motor, the alignment is unaffected by the operational conditions of the rig. The frame is designed such that the spindle can be moved axially in order to replace the test bearing. Locking and unlocking the spindle in the frame are done using two bolts. These bolts provide a clamping force between the frame and the spindle. This technique is adopted in milling machines as the initial alignment

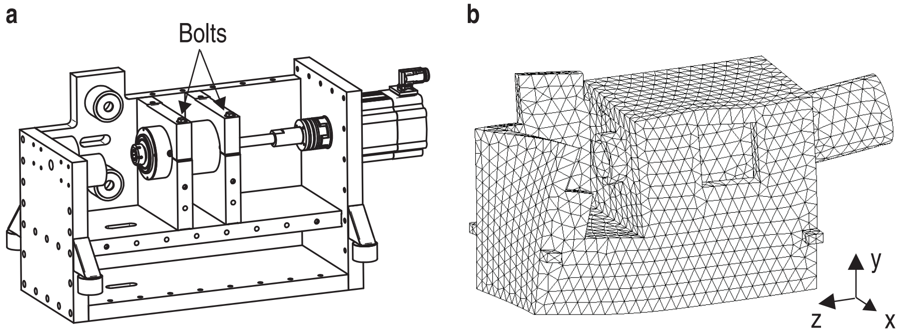

Figure 3.16: Frame of the test rig (shown without its top and front panel) (**a**) and its first flexible mode (**b**).

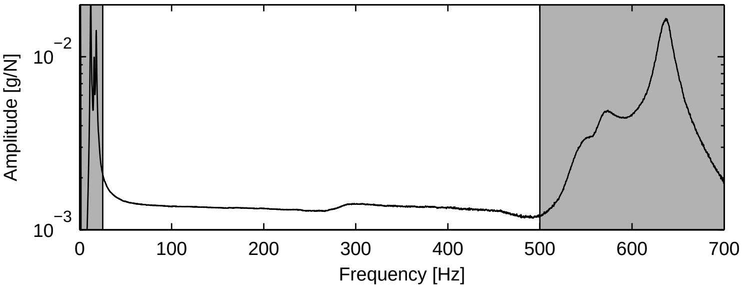

Figure 3.17: Sum of FRFs measured during the modal analysis of the test rig. The frame is designed to be free of resonances in a range from 25 to 500 Hz (white area).

with other components such as the motor is preserved after each locking action.

The frame of the test rig is a closed and rigid structure mounted on four bushings. The bushings dynamically decouple the test rig from the environment. The frame itself consists of an upper and a lower part, as shown in Fig. 3.16**a**. The upper part connects the different components of the test rig while the lower part forms a stiff structure to improve the torsional behaviour of the frame. The dynamics of the frame are analysed using a 3D FE model. The model includes the motor and the cylindrical housing of the spindle. The stiffness increase provided by the spindle bearings and the spindle shaft is neglected. The bushings are modelled as 3D springs. The six rigid body modes of the test rig moving on its bushings are all located between 4 and 16.4 Hz. The first flexible mode of the frame appears at 663 Hz. Fig. 3.16**b** visualises this first torsional mode.

To validate the FE calculations, the frame is equipped with twelve accelerometers and a modal analysis is performed. The test bearing housing is not mounted, as its dynamics are analysed separately. The sum of FRFs is shown in Fig. 3.17. The rigid body modes are located below 25 Hz. The first global flexible mode appears at 638 Hz. The dynamic behaviour of a bearing can thus be analysed in a range from 25 to 500 Hz, free of resonances of the frame.

Spindle of the test rig

The spindle of the test rig consists of a solid shaft supported by two tapered roller bearings in a cylindrical housing (Fig. 3.6). The tapered roller bearings are mounted in O-arrangement and axially preloaded to increase the bending stiffness of the spindle. The shaft is connected to the motor through a flexible coupling, decoupling both parts dynamically.

During design, an FE model of the stepped shaft is used to evaluate the spindle dynamics. The one-dimensional (1D) geometry of the model is shown in Fig. 3.18**a**. The radial and axial shaker excite the spindle in respectively the x-direction and the z-direction. The modes of the shaft in the xz-plane of the test rig are therefore analysed. Each node of the FE model has three degrees of freedom: translation in the x-direction, translation in the z-direction and rotation around the y-axis. The stiffness of the spindle bearings depends on the axial preload and is estimated based on Ref. [7]. A radial stiffness (in the x-direction) of 510x10^6 N/m, an axial stiffness (in the z-direction) of 263x10^6 N/m and a tilt stiffness (around the y-axis) of 160x10^3 Nm/rad are used. In the frequency range of interest, the FE model of the frame indicates a negligible relative movement between the spindle bearing seats inside the cylindrical housing. Flexibility between the outer rings of the spindle bearings is therefore not included in the current model. The vibrating part of the coupling between the motor and the shaft is modelled as a point mass. The test bearing housing is modelled as a point mass as well, as its dynamics are analysed separately. Between the bearing housing and spindle shaft, a stiffness element is added which represents the test bearing. A radial stiffness of 35x10^6 N/m (in the x-direction) and an axial stiffness of 3.5x10^6 N/m (in the z-direction) are used as average values of possible test bearing stiffnesses.

The first six modes of the spindle and test bearing assembly are shown in Fig. 3.18**b**–**g**. The first mode is characterised by a strong radial motion of the coupling part. In the second and third mode, the housing mass strongly vibrates w.r.t. the spindle in respectively the axial and radial direction. The

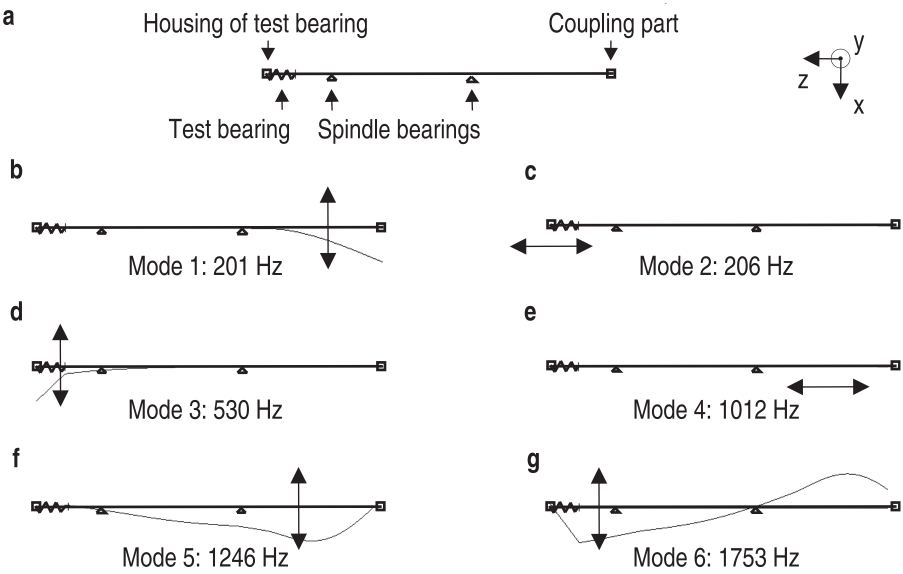

Figure 3.18: Model (**a**) and first six modes (**b**–**g**) of the spindle and test bearing assembly.

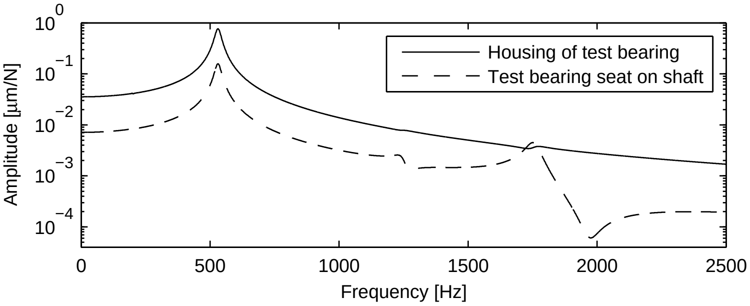

Figure 3.19: FRF of the radial displacement at two locations of the model.

resonance frequencies and damping ratios of these two modes are determined by the dynamic behaviour of the test bearing. They are used to identify the stiffness and damping of the test bearing in Chapter 5 and 6. At the resonance frequency of the fourth mode, the spindle shaft translates axially. In the fifth and sixth mode, the spindle shaft rotates around one of the two spindle bearings.

To understand the effect of the modes on the test bearing motion, the FRF between a shaker force on the bearing housing and the displacement of the test bearing is analysed. For a radial shaker excitation, Fig. 3.19 shows the displacement of the housing mass (solid line) and the displacement of the test bearing seat on the shaft (dashed line). Besides the third mode at 530 Hz due to the test bearing, clear radial motion of the bearing seat on the shaft first appears at 1753 Hz. For an axial shaker excitation, clear axial motion of the test bearing seat on the shaft first appears at 1012 Hz. The bearing can thus be excited up to 500 Hz without any influence of the spindle dynamics.

The modes of the spindle shaft are experimentally measured to validate the spindle dynamics. A shaker load is introduced on the test bearing housing while three accelerometers measure the response of the shaft. As the shaft is mounted in a cylindrical housing, it is only possible to install accelerometers on the front and the back of the shaft. Consequently, a full modal analysis could not be performed. The sixth mode of the spindle and test bearing assembly, having a high response at the sensor locations, could however be identified.

To analyse the effect of the air spring load on the spindle dynamics, a modal test is performed at three different load levels of the air springs. The sixth mode is found at 1899 Hz, 1908 Hz and 1915 Hz for respectively 400 N, 1000 N and 1600 N radial test bearing load. As the radial load introduced by the air springs is small compared to the high axial preload, the stiffness of the spindle bearings is only slightly affected by the air pressure. The change in spindle dynamics at different loads and speeds is therefore neglected when evaluating the test bearing stiffness (Sect. 5.1.3).

3.3.3 Bearing lubricant film

The lubricant film, having a high electrical resistance, separates the rolling elements and raceways, having a low electrical resistance. The electrical resistance through the bearing reveals the formation and behaviour of the lubricant film. This section describes the electrical circuit to measure the resistance. It further discusses the detection of metallic contact inside the bearing. Finally, some important considerations when interpreting the results are given.

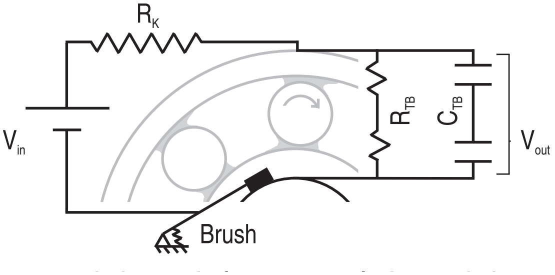

Figure 3.20: Electrical circuit to measure the electrical resistance of the rotating bearing R_{TB}. The circuit consists of a voltage source V_{in}, a known resistance R_K, the test bearing and a brush.

Measuring the electrical resistance

The circuit to measure the electrical resistance of the test bearing is shown in Fig. 3.20. The bearing is represented by an electrical impedance Z_{TB}, consisting of a resistance R_{TB} and a capacitance C_{TB} in parallel. The different metal-lubricant-metal transitions in the bearing can be treated as a number of resistors and capacitances in parallel and in series, forming the total resistance R_{TB} and capacitance C_{TB} [48]. The circuit is powered by a regular 6 V battery V_{in}. The battery operates as a stable and independent floating power supply. A known resistance R_K of 121 kΩ is connected in series with the bearing. A similar circuit is proposed by Matharu [73]. To guide the current back from the inner ring to the power supply, a carbon brush is mounted on the bearing shaft. The air springs, supporting the housing of the test bearing, act as electrical isolators. This ensures that the current can only pass through the test bearing to close the circuit and the bearing electrical resistance can be measured.

The known resistance R_K and the bearing resistance R_{TB} form a voltage divider circuit allowing to determine the bearing resistance. As a direct current (DC) power supply is used, the capacitance of the bearing does not influence the measurement. The known resistance R_K further guarantees that the current through the test bearing is always smaller than 0.05 mA. High currents cause electric sparking between the rolling elements and raceways. A current density of less than 100 mA/mm^2 does not influence the bearing life [70]. With an estimated total surface area through the test bearing contacts of at least 0.1 mm^2 (Sect. 4.4.1), the transferred current cannot damage the bearing. The resistance of the other components in the circuit, namely a part of the shaft and housing and the carbon brush, is identified separately. The resistance of these components is negligible compared to the known resistance R_K.

Calculating the electrical resistance

Calculation of the bearing electrical resistance is based on the relation between the output voltage V_{out} and the input voltage V_{in} of a voltage divider:

$$\frac{V_{out}}{V_{in}} = \frac{Z_{TB}}{R_K + Z_{TB}} \tag{3.1}$$

The ratio between the input and output voltage is fully determined by the relative importance of the bearing impedance Z_{TB} w.r.t. the total impedance of the circuit. Using a DC power supply, the bearing impedance equals the bearing resistance and is given by:

$$R_{TB} = \frac{R_K}{\dfrac{V_{in}}{V_{out}} - 1} \tag{3.2}$$

During normal operation, the bearing resistance is similar to the known resistance. It is thus determined with maximum accuracy using the voltage divider circuit.

Calculating the PCT

Based on the voltage drop over the test bearing, the time fraction of metallic contact is estimated. The percentage of contact time (PCT) is introduced by Heemskerk [48] as the time fraction of which the voltage drop is below a certain (arbitrary) reference level. The reference level is set just above 0 V, which corresponds to asperity contact. In the work of this manuscript, the reference level is set at 0.05 V. A PCT value of 0% corresponds to complete separation between the rolling elements and raceways while a PCT value of 100% corresponds to continuous metallic contact.

Interpreting the electrical resistance and PCT

When evaluating the electrical resistance and PCT of a full bearing, care should be taken when interpreting the results. Firstly, measuring a high resistance and low PCT implies that the conductivity between the inner and outer ring is low. This condition is already reached when the conductivity is low only through the inner ring contact or only through the outer ring contact for all rolling elements. A low conductivity does not prove that the lubricant sufficiently separates both the inner ring and rolling elements and the outer ring and rolling elements. The lubricant film might perform well at one ring while failing at the other. It is however reasonable to assume that the lubricant film behaves in the same way at both the inner and outer raceway contacts. Therefore, the resistance and PCT can be used to evaluate the lubricant film. Secondly, the voltage drop is dominated by the heaviest loaded rolling element, as the contact surface area is maximal and the film thickness is minimal. To analyse the resistance through a particular rolling element, Fujii [27] replaces all the rolling elements by ceramic balls except for one conducting the current. Finally, in case a voltage drop is measured over several bearings at ones, the most critical rolling element of the most critical bearing dominates the result. It is however not possible to locate this rolling element based on the measured voltage drop.

3.4 Data acquisition and control

To acquire sensor data and control the test rig, a computer is connected to an FPGA-based controller (NI cRio 9074 with 2M Gate FPGA). A real-time program is running on the computer while all acquisition and control data pass through the controller. Fig. 3.21 shows the communication between the different test rig components (dashed lines). The software is tailored to the requirements of the test rig. It runs three parallel loops:

- The high speed acquisition loop cycles at 20 kHz and records the sensor data to a file. Analog input data from accelerometers, load cells, proximity probes and the electrical resistance circuit is passed over the network using FIFO buffers and logged to a universal file format. The data from up to twelve analog channels is simultaneously acquired. Digital input data from the optical trigger and motor encoder is logged and used to correct the proximity probe data for mechanical runout. This correction is discussed in Sect. 3.3.1.
- The high speed control loop cycles at 20 kHz and generates the control signals for the electrodynamic shakers. The shakers are fed with broadband noise or periodic signals.
- The low speed loop cycles at 20 Hz and controls the pneumatic circuit and the electric motor. Also, the data from four thermocouples is acquired in this loop. Each of the four air springs is controlled independently. The software calculates the required air pressure based on the desired radial and axial bearing load, using the relations described in Sect. 3.2.3.

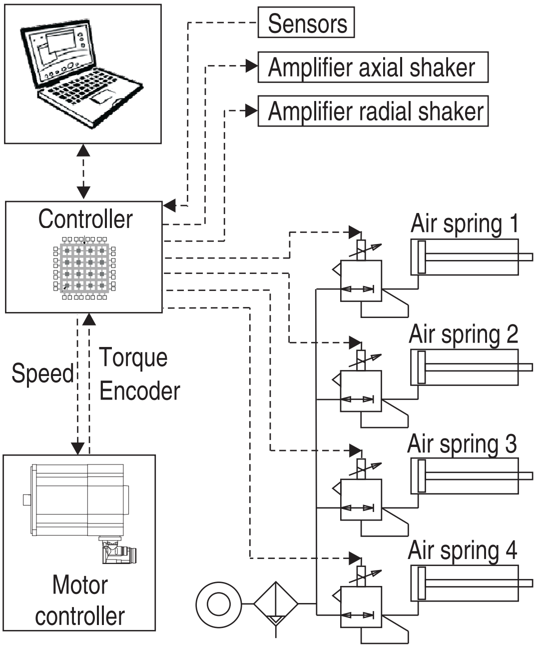

Figure 3.21: Communication between the different test rig components (dashed lines) and the air circuit of the test rig (solid lines).

During acquisition of the analog input channels, the bearing operational conditions are registered as well. The static load, speed and temperature are logged. The NI TDMS file format allows including these conditions, such that they are available during post-processing of the data. Also, the status of the communication between the controller and computer is continuously checked based on overflow and underflow detection of the data buffers.

The software allows planning a series of measurements in advance. The static load, dynamic load and speed are automatically adjusted after each successive test. To perform bearing lifetime tests, the software continuously monitors the root mean square (RMS) value of an input channel. The test is stopped when this RMS value or the bearing temperature exceeds a threshold.

3.5 Conclusion

An innovative and versatile bearing test rig is presented. Based on the discussion of the different concepts, there is a clear preference of one concept over the others. The test bearing is mounted on a rigid spindle formed by two tapered roller bearings in the O-arrangement. The O-arrangement is adopted in the spindle design as a high bending stiffness and a preload which is independent of the operational temperature are obtained. The optimal preload is set such that the clearance in the bearings is removed. This ensures smooth running with high running accuracy. The test bearing is mounted on an auxiliary shaft, clamped in the spindle of the test rig using a collet chuck. Precise alignment of the test bearing with the spindle is guaranteed. The housing of the test bearing is adapted to the test bearing using an intermediate sleeve. This modular structure allows testing different types and sizes of bearings. A load is directly applied on the outer ring of the test bearing in both the radial and axial bearing direction. The static load is provided by air springs while the dynamic load is provided by shakers. Full decoupling of the different force components is obtained.

The test rig allows precise identification of the bearing motion, the bearing dynamics and the behaviour of the lubricant film. The bearing motion is measured using capacitive proximity probes, mounted on the housing and pointed to the rotating shaft. Correction for mechanical runout is implemented. The test rig is designed to analyse the dynamic behaviour of the test bearing in a frequency range from 25 to 500 Hz. The main components of the test rig are designed using FE software such that the frequencies of the structure's flexible modes exceed 500 Hz. Modal analyses of the different components confirm the results of these calculations. The behaviour of the lubricant film is analysed based on the electrical resistance through the bearing. An electrical circuit to measure the resistance and detect metallic contact is discussed.

Chapter 4

Operational behaviour of the test bearing

In this chapter, the presented test rig is used to study the operational behaviour of a deep groove ball bearing. Three operational properties of the bearing are investigated: the bearing motion, the behaviour of the lubricant film and cage slip. The measurements are used to:

- Interpret the dynamic behaviour of the test bearing and the effect of external dynamic loads on the lubricant film formation in Chapter 5 and 6.
- Validate precise operation of the test rig. Smooth running of the spindle with high running accuracy and isolation of motor excitations (Sect. 3.2.1) are reflected in the measurements.
- Analyse the possibilities to identify the three operational properties based on techniques which can be applied in most rotating machinery: measurement of the radial displacement and the electrical resistance of the test bearing.
- Investigate the potential to estimate the bearing load based on these properties. Damage prognosis techniques estimate the system's remaining useful life using predictive models and past, current and anticipated future environmental and operational conditions [54]. The actual bearing load or detection of overloading can significantly improve the evaluation of the remaining useful life.

Throughout the manuscript, the same test bearing and the same test conditions are used. The selected test bearing and test conditions are first introduced in Sect. 4.1 and 4.2. The bearing motion, the behaviour of the lubricant film and cage slip are analysed in respectively Sect. 4.3, 4.4 and 4.5. Finally, the potential to estimate the bearing load using these properties is discussed in Sect. 4.6.

4.1 Test bearing

The test rig allows mounting different types and sizes of bearings. The current work uses a deep groove ball bearing. All the measurements presented in this manuscript are based on the same test bearing (with the exception of the accelerated lifetime tests of Sect. 6.3). The behaviour of the test bearing is strongly determined by its internal clearance. The clearance should be known when interpreting the results.

4.1.1 Selection of the test bearing

Single row deep groove ball bearings are used in a wide variety of applications. They are simple in design, non-separable and robust in operation. In the current work, a deep groove ball bearing 6302 (designation according to DIN 623 [20]) is analysed. Fig. 4.1**a** shows the test bearing and the definition of the coordinate system used in this manuscript. The bearing rotates around the z-axis. It is radially loaded in the x-direction and axially loaded in the minus z-direction.

The properties of the test bearing are summarised in Appendix D. The bearing geometry is characterised by 2 diameters (Fig. 4.1**b**): the pitch diameter d_m and the rolling element diameter D. The bearing pitch diameter is the mean of the inner raceway diameter d_i and the outer raceway diameter d_o. All the bearing components are made of steel.

The shielded version of the test bearing is mostly used in industry. As the sheet steel shields may influence the dynamic properties and electrical resistance of the bearing, the version without shields is preferred in the current study. Proper sealing is provided by radial shaft seals mounted on the bearing housing. The test bearing uses all purpose industrial grease, consisting of lithium soap and mineral oil. More than 90% of all rolling elements are greased and sealed for life [69], making grease lubrication the most interesting type to investigate.

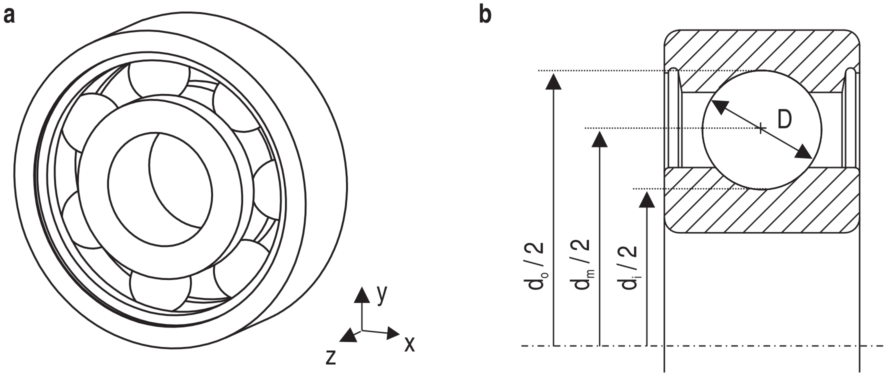

Figure 4.1: Overview (**a**) and cross-section (**b**) of the test bearing (shown without its cage).

4.1.2 Operational clearance of the test bearing

A deep groove ball bearing is generally designed to have internal radial clearance. The radial clearance (also called diametral clearance) is the maximum distance within which one ring can move freely and radially [102]. W.r.t. the rolling element diameter D, the inner raceway diameter d_i and the outer raceway diameter d_o, the radial clearance P_d is defined as (Fig. 4.1**b**):

$$P_d = d_o - d_i - 2\ D \tag{4.1}$$

The bearing manufacturer determines the optimum internal clearance for each bearing. The optimum clearance depends on the application. More radial clearance leads to larger contact angles such that the bearing is better suited to carry axial loads [118]. As the real bearing geometry deviates from the nominal geometry, the actual clearance of the test bearing is unknown. An interval for all possible values of the clearance is provided by the manufacturer. Three different intervals are defined:

- Although the manufacturing tolerances on the internal bearing dimensions are strict, small deviations from the nominal values cannot be avoided. The resulting interval of the radial clearance is indicated as the radial clearance before mounting.
- The applied clearance or interference fit between the bearing and the shaft or housing influences the geometry. Typically, an interference fit is

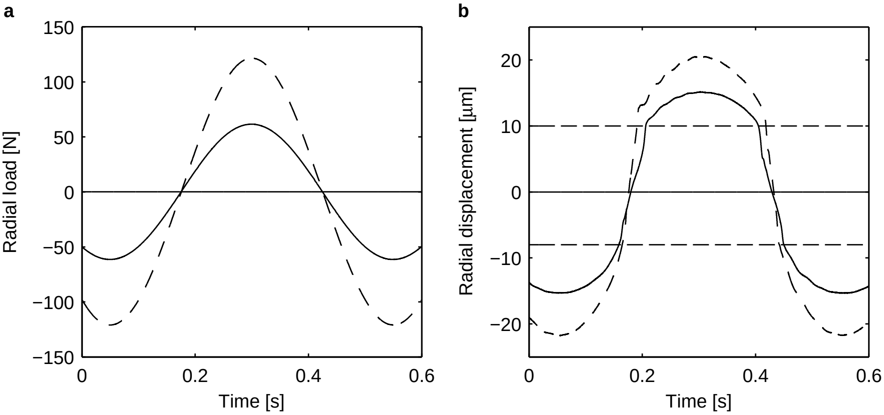

Figure 4.2: Radial bearing load (**a**) and radial bearing displacement (**b**) to identify the radial clearance. Two levels of the load are shown.

used between the rotating ring and its connecting structure to avoid a relative movement between both. An excessive interference fit changes the raceway geometry and the radial clearance [103]. The radial clearance after mounting takes into account these changes.

- As the shaft normally heats up more than the housing during operation, the inner ring expands more than the outer ring. The actual geometry and the internal clearance in the bearing change. The radial clearance during operation includes this effect.

Appendix D summarises the numerical values for the different clearance intervals.

After mounting of the test bearing, the actual radial clearance is measured. The radial shaker applies a sinusoidal load while the radial bearing displacement is measured using a capacitive proximity probe. The load is slowly varied with a frequency of 2 Hz. Fig. 4.2 shows the measured shaker load and the measured radial displacement. Two levels of the load amplitude are tested. The dashed vertical lines in Fig. 4.2**b** indicate the points where contact is made. Between -8 and 10 µm, the bearing moves through its clearance. Outside this region, the bearing elastically deforms. The upward and downward movement are not identical as the position of the rolling elements is different at both sides of the bearing. The shift of the displacement between -8 and 10 µm is determined by the limited inertial force of the housing and the radial static bearing load due the housing mass.

The radial clearance of the test bearing is 18 μm after mounting. As the bearing clearance can only be measured under zero static load, it is not possible to determine the clearance during operation. Based on the clearance values provided by the bearing manufacturer, a 4 μm reduction of the clearance due to a 10 °C temperature difference between inner and outer ring is observed. The estimated clearance during operation is thus 14 μm.

4.2 Test conditions

Throughout the manuscript, different properties such as the bearing motion and lubricant film thickness are investigated. When analysing the influence of the operational conditions on these properties, the conditions are consistently varied. This section presents the operational conditions of the measurements. The radial and axial load acting on the bearing are distributed over the different rolling elements. The internal load distribution is discussed for the different tested load levels.

4.2.1 Operational conditions

The static bearing load, operational temperature and rotational speed are consistently varied when analysing the influence of the operational conditions.

Influence of the load

When analysing the influence of the radial bearing load, the radial load is varied from 0 to 1600 N. Only the radial air springs are mounted during these tests. When analysing the influence of the axial bearing load, the axial air springs are added. The axial load ranges from 0 to 800 N while a fixed radial load is applied. The bearing speed is kept constant during the measurements. The measurements are performed in quick succession, such that isothermal conditions (w.r.t. time) can be assumed. The sole influence of the load is seen while an influence of the bearing temperature is avoided.

At the highest load level, the maximum Hertzian contact pressure is limited to 2500 MPa (following the calculations of Sect. 4.4.1). This is commonly accepted as a high but allowed maximum contact pressure for rolling element bearings. In some applications and during endurance testing, the maximum contact pressure in bearings can reach 3450 MPa [46].

The bearing load is often compared to two characteristic values: the static load rating C_0 and dynamic load rating C. The definition of admissible plastic deformation implies that the total deformation of the rolling element and the raceway occurring at the contact area under maximum stress does not exceed 0.01% of the rolling element diameter. Higher loads would jeopardise the properties required for rotation of the rolling elements. The maximum load is defined by the static load rating of the bearing. This rating represents the load at which, under defined operating conditions, the admissible plastic deformation is reached [7]. The static load rating equals 5.4 kN (Appendix D). The dynamic load rating of a radial bearing corresponds to a pure radial constant load at which the L_{10} bearing life equals 1 million revolutions (Sect. 2.4.2). The dynamic load rating equals 11.9 kN (Appendix D).

Recalling Sect. 3.1.2, the test bearing is mounted on a cantilever shaft and the outer ring possibly tilts w.r.t. the inner ring. To restrict this tilt angle, the spindle is optimised for maximum bending stiffness (Sect. 3.2.1) while the housing of the test bearing is flexibly connected to the environment (Sect. 3.2.3). The tilt angle is measured for the different considered levels of the radial and axial load. The measurement is based on the relative bearing displacement seen by both axial proximity probes (Sect. 3.3.1). The tilt angle reaches its maximum value when a pure radial load of 1600 N is applied. Depending on the mounted stingers to transfer the dynamic load, a tilt angle up to 2.8 arcmin is measured. This misalignment is tolerated by the bearing manufacturer [99].

Influence of the temperature

The influence of the temperature is analysed during the first 40 min of a warm-up. Starting at room temperature, the bearing is brought to speed after which the measurement starts. A fixed radial load is applied on the bearing. The inner and outer ring temperature are measured simultaneously. Heat, generated by friction in the rolling contacts of the bearing, is dissipated more easily through the bearing housing than the bearing shaft. As in most bearing applications, the inner ring heats up more than the outer ring. The temperature of the inner ring increases faster and reaches its stable values at an earlier point in time.

Influence of the speed

When analysing the influence of the bearing speed, the rotational speed of the motor is varied from 0 to 1500 r/min. As the outer ring of the test bearing is stationary, the bearing speed corresponds to the speed of the motor and the shaft. A fixed radial load is applied on the bearing during all measurements.

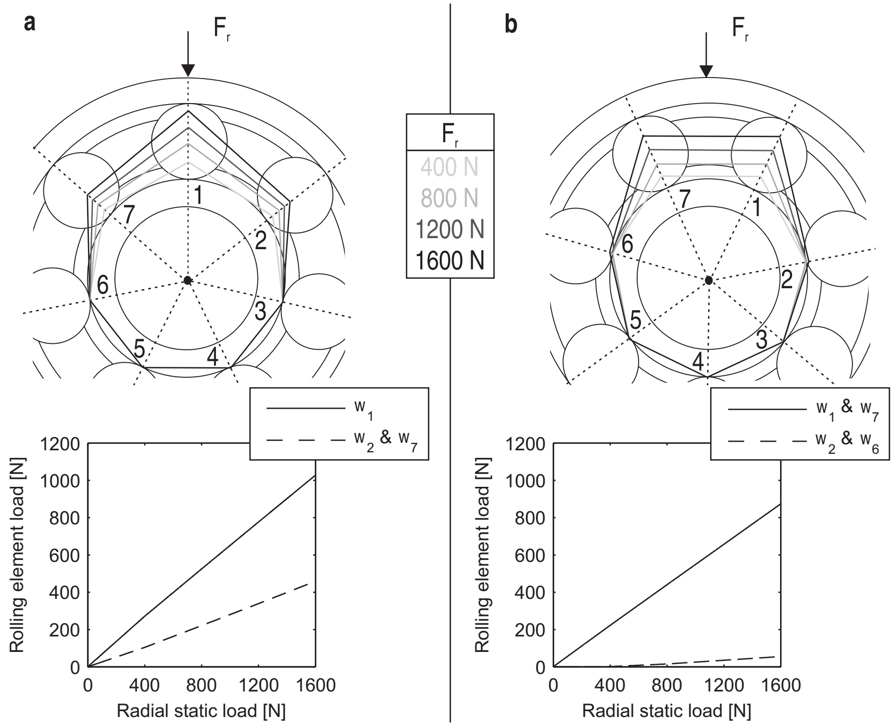

Figure 4.3: Internal load distribution for four different levels of the radial load and two positions of the rolling element set (**a** and **b**).

In Sect. 4.4.4, it is shown that the lubricant film is formed in this range of the speed. The influence of the film formation is consequently analysed. The measurements are performed in quick succession, such that isothermal conditions can be assumed. The sole influence of the speed is seen while an influence of the temperature is avoided.

4.2.2 Internal load distribution

To understand the effect of the static load, the internal load distribution should be known. The radial and axial load acting on the bearing are distributed over the different rolling elements. The calculation of the internal load distribution is done by the bearing manufacturer. It is based on an analytical model taking into account the flexibility of the contacts.

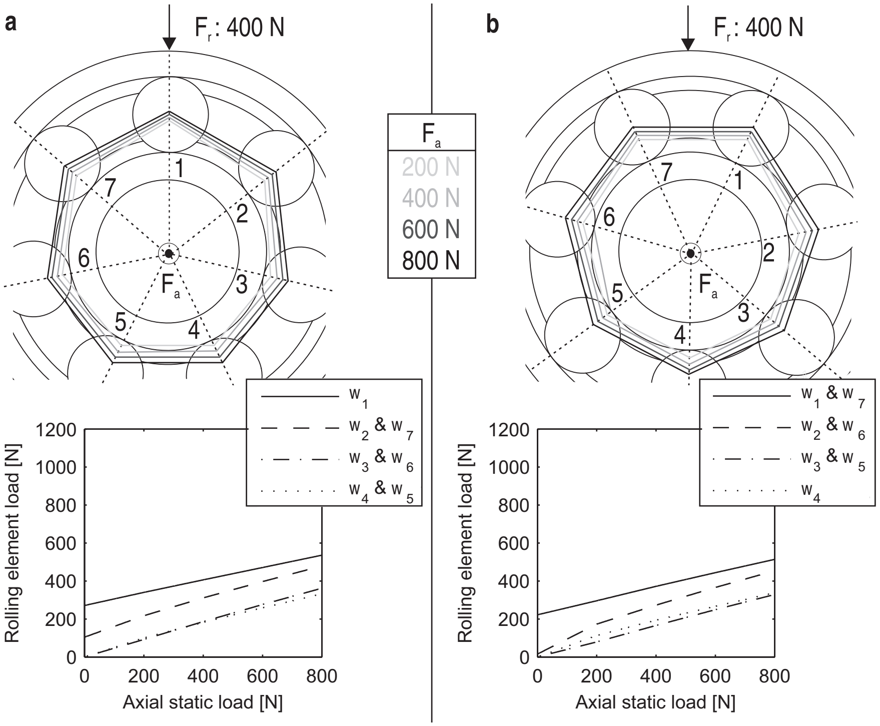

Figure 4.4: Internal load distribution for four different levels of the axial load and two positions of the rolling element set (**a** and **b**). A radial load of 400 N is simultaneously applied.

Fig. 4.3 shows the rolling element load w for four levels of the radial load. As the angular position of the shaft changes, the position of the cage and rolling elements changes during rotation. In the first angular position (**a**), the load is transferred through three rolling elements: 1, 2 and 7. In the second angular position (**b**), the load is transferred through four rolling elements: 1, 2, 6 and 7.

When introducing an axial load, all rolling elements are loaded. Fig. 4.4 shows the load distribution for four levels of the axial load. A radial load of 400 N is simultaneously applied.

4.3 Bearing motion

This section discusses the motion of the test bearing. Both the influence of the bearing load and the structure's dynamics are analysed.

4.3.1 Causes of bearing motion

There are two causes of bearing motion and vibrations: variable elastic compliance and geometrical imperfections.

At all times, even perfect bearings generate vibrations. The vibrations are caused by the rotation of a finite number of loaded rolling contacts between the rolling elements and rings. Because these contacts are elastic, the bearing stiffness becomes explicitly dependent on time [118]. During rotation, the position of the rolling element set continuously varies between the position of Fig. 4.3**a** and the position of Fig. 4.3**b**. As analysed in Sect. 5.4.1, the bearing stiffness consequently varies between these two positions. This effect was first recognised by Perret [3, 83, 84] and is called variable elastic compliance. It is most easily measured at low frequencies, as the first harmonics are dominant.

Geometrical imperfections in the bearing lead to bearing-induced vibrations as well. Localised defects, such as cracks, pits and spalls, are caused by damage of the rolling surfaces. When a localised defect passes its mating surface, a short force pulse is generated. Under a constant rotational speed, these pulses are generated at characteristic frequencies [102, 110]. Distributed effects, such as surface roughness, waviness, misaligned raceways, rolling element diameter variations and cage runout are caused by the manufacturing processes or improper installation. Ref. [102] gives a general overview of the current literature on the relation between geometrical imperfections and bearing-induced vibrations. The imperfections mainly appear in the spectrum at high frequencies, where the vibration amplitudes are both high and enhanced by structural resonances.

Two commonly observed geometrical imperfections are waviness and rolling element diameter variations. Waviness consists of global sinusoidally shaped imperfections on the outer surface of the components and is caused by irregularities in the grinding and honing process. Nowadays, the amplitudes of waviness in small deep groove ball bearings are of the order of nanometers. In spite of that, waviness still produces significant vibrations in the entire audible range [118]. Differences smaller than the manufacturing tolerances between the ball diameters are unavoidable. The resulting off-sized ball effect is analysed both experimentally and analytically in the literature [2]. Differences of 1 to

2 µm are assumed. Vibrations at multiples of the cage speed result from this type of imperfections [118].

4.3.2 Analysis of bearing motion

This work analyses the bearing motion at low frequencies using a capacitive proximity probe. For deep groove ball bearings, the motion due to variable elastic compliance is predominantly oriented in the radial direction. The radial bearing motion is analysed using the spectrum of the radial displacement. The radial capacitive probe measures the displacement of the test bearing in the direction of the radial load (x-direction). The bearing rotates at 600 r/min. A strong excitation of the bearing is observed at this speed (Sect. 4.3.5). A radial load of 1000 N is applied on the bearing.

Fig. 4.5 shows the spectrum of the radial displacement. The following spectral components are identified:

- At the rotational frequency of the shaft f_s and its harmonics, an excitation is observed. This excitation originates from an eccentricity of only a few micron between the main spindle shaft of the test rig and the auxiliary shaft of the test bearing. Despite the high accuracy applied during manufacturing of both the collet and collet chuck, and the conical shape of the mating parts, a radial runout of the auxiliary shaft is inevitable.
- At the frequency at which the cage and rolling element set are rotating f_c as well as its harmonics, an excitation is measured. It is caused by geometric imperfections of the bearing, more precisely variations of the rolling element diameters and cage runout.
- At each seventh multiple of the cage frequency, a highly pronounced excitation is observed. The test bearing contains seven rolling elements. The frequency at which a rolling element is passing the loaded zone of the stationary outer ring equals seven times the cage frequency. This frequency is called the ball pass frequency (BPF). It is also abbreviated as BPFO, emphasising that the rolling elements are passing as seen from a fixed point on the outer ring. The high excitation at the BPF is the result of variable elastic compliance. Each time a rolling element passes the loaded zone, a varying stiffness excites the structure.
- The effect of variable elastic compliance is enhanced by the excitation due to the eccentricity of the collet chuck. A modulation of the BPF at the rotational frequency of the shaft appears. It is expressed by the sidebands of the BPF and its harmonics at a distance equal to 1 x f_s, 2 x f_s, etc.

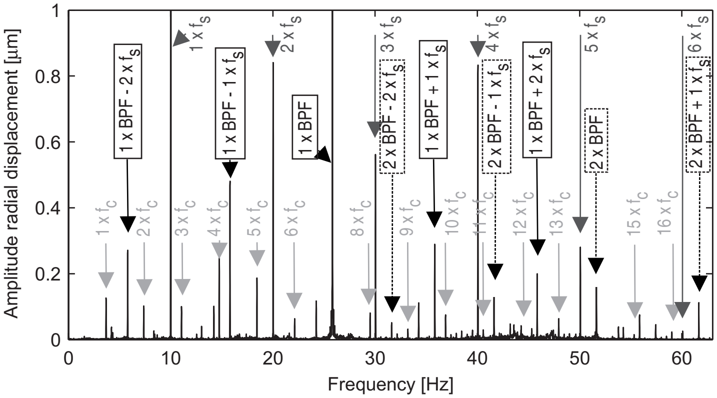

Figure 4.5: Spectrum of the radial bearing displacement. The different components of the bearing motion are identified.

The remaining peaks of the displacement spectrum correspond to an excitation of the spindle bearings. The cage frequency and its harmonics of both spindle bearings are identified. The excitation of the spindle bearings is negligible compared to the test bearing excitation.

The main excitation of the test bearing is the motion at the BPF, resulting from variable elastic compliance. The bearing displacement at the BPF is determined by both the bearing load and the structure's dynamics, because:

- The bearing load determines the variation of the bearing stiffness when a rolling element passes the loaded zone.
- The structure's dynamics determine how the bearing excitation is amplified by the mass, stiffness and damping characteristics of the bearing and its surrounding structure.

In the following sections, the influence of the bearing load and the structure's dynamics on the displacement at the BPF is analysed. This, by variation of the bearing load, temperature and speed.

4.3.3 Variable compliance: influence of the load

Changing the load and keeping the bearing temperature and speed constant shows the isolated influence of the bearing load. The displacement at the BPF

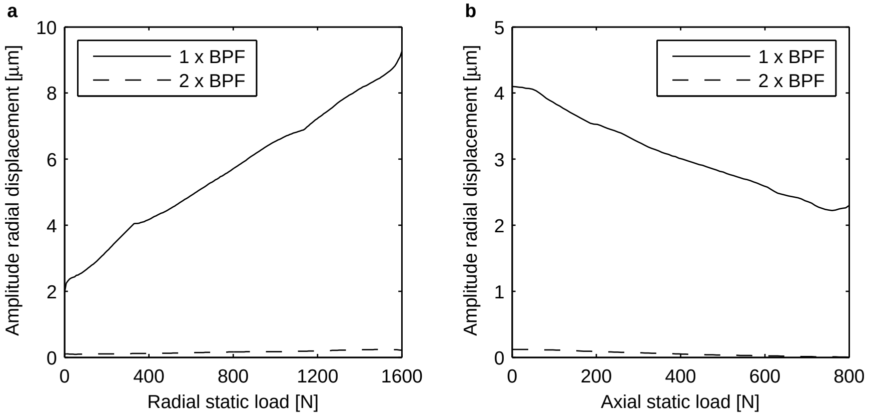

Figure 4.6: Displacement at the BPF and its second harmonic during a run-up of the radial (**a**) and axial (**b**) load.

and its second harmonic is calculated while increasing the radial and axial bearing load. Keeping the bearing speed fixed at 600 r/min, the BPF equals 25.3 Hz. The influence of the varying bearing load on the structure's dynamics is neglected in this analysis, as this is a second-order effect.

Fig. 4.6**a** shows the result for a run-up of the radial load from 0 to 1600 N. No axial load is applied. As the radial load increases, the variation of the radial bearing stiffness and deformation between the two positions of Fig. 4.3 increases. The effect of variable elastic compliance consequently increases.

Fig. 4.6**b** shows the result for a run-up of the axial load from 0 to 800 N. A 400 N radial load is simultaneously applied. Ball bearings are usually mounted with an externally applied axial load to ensure proper loading of the rolling elements. Also, the level of vibrations generated by the bearing is generally reduced [118]. As the axial load increases, the variation of the radial bearing stiffness and deformation between the two positions of Fig. 4.4 decreases. The effect of variable elastic compliance consequently decreases. This was also observed in the measurements of Ref. [3].

4.3.4 Variable compliance: influence of the temperature

Changing the temperature and keeping the bearing load and speed constant shows the influence of the structure's dynamics. As the bearing temperature

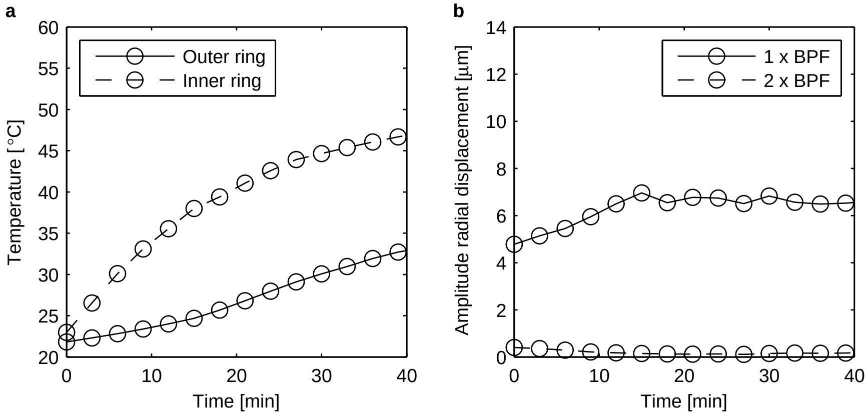

Figure 4.7: Temperature (**a**) and displacement at the BPF and its second harmonic (**b**) during a warm-up.

varies, its stiffness and damping properties change. The structure's dynamics consequently change, as well as the response at the BPF and its second harmonic.

Starting at room temperature, the displacement at the BPF and its second harmonic is measured during a warm-up of the bearing. Fig. 4.7 shows the result. The displacement is measured every 3 min. A radial load of 1000 N is applied and the bearing rotates at 600 r/min. The BPF increases during the first 15 min of the warm-up. After 15 min, the steady-state value is reached. Sect. 5.3 discusses the varying stiffness and damping of the bearing w.r.t. the temperature. A decrease of the bearing stiffness and damping during the first 20 min of a warm-up influences the bearing response at the BPF. This effect of the structure's dynamics is better seen when analysing the influence of the bearing speed in the next section.

4.3.5 Variable compliance: influence of the speed

Changing the speed and keeping the bearing load and temperature constant shows the influence of the structure's dynamics. Amplification of the bearing response due to the structure's dynamics depends on the frequency of excitation. As the bearing speed changes, the BPF changes proportionally. The response at the BPF consequently changes.

Fig. 4.8 shows the Campbell diagram of the bearing displacement. The rotational speed is increased from 0 to 1500 r/min. A 1000 N radial load is applied. Up to

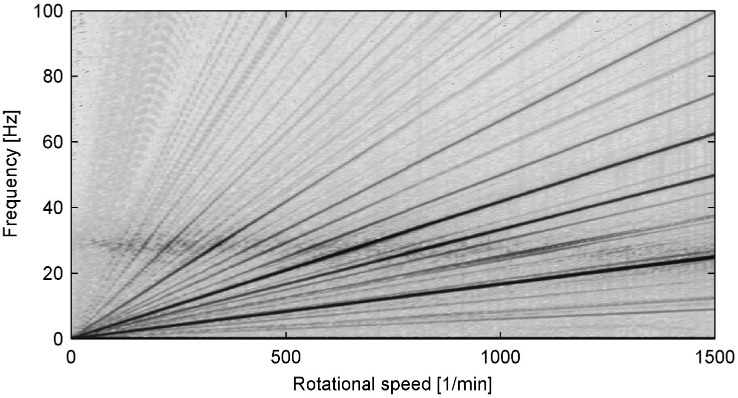

Figure 4.8: Campbell diagram of the bearing displacement during a run-up of the speed.

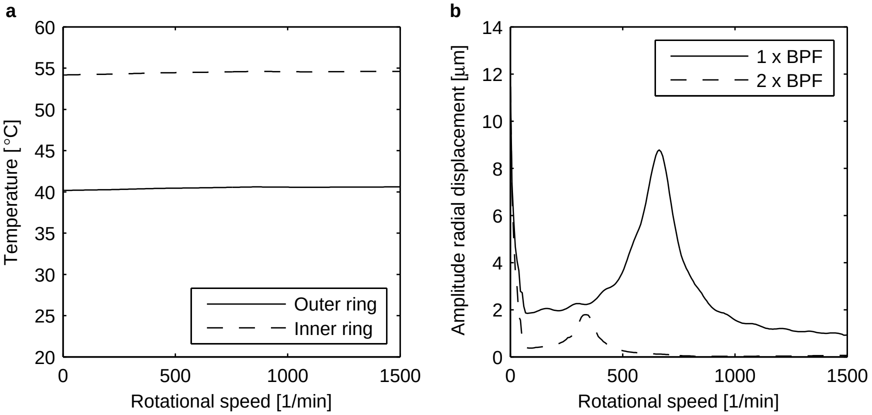

Figure 4.9: Temperature (**a**) and displacement at the BPF and its second harmonic (**b**) during a run-up of the speed.

100 Hz, the bearing motion is clearly measured. Above 100 Hz, the variations of displacements no longer exceed the noise level. Increased excitation at approximately 30 Hz is observed. This excitation originates from a rigid body mode of the housing mass, at which the housing mass rotates around its y-axis (Sect. 5.1.2). Rotation around the y-axis through the centre of the bearing generates a displacement in the measurement direction (x-direction) at the location of the radial proximity probe. The rotational rigid body modes of the housing mass around the x-axis and z-axis do not result in a significant displacement in the measurement direction, at the location of the proximity probe. They are not observed in the Campbell diagram.

While increasing the speed, the displacement at the BPF and its second harmonic is calculated using the order tracking technique. The result is summarised in Fig. 4.9. The displacement at the BPF reaches a maximum at 660 r/min. The BPF then equals the frequency of the rotational rigid body mode, amplifying the bearing response. The second harmonic reaches it maximum at 330 r/min, where the response is amplified by the same rotational rigid body mode.

4.4 Lubricant film thickness

The measured electrical resistance through the bearing allows evaluating the lubricant film thickness and the time fraction of metallic contact (PCT). First, a model of the bearing electrical resistance is introduced. This model allows linking the measured electrical resistance to the lubricant film thickness. Afterwards, the electrical resistance and PCT are discussed for different operational conditions. The influence of the bearing load, temperature and speed is analysed.

4.4.1 Model of the bearing electrical resistance

The electrical resistance of the bearing is determined by the resistance of each conductive path through the bearing. Each loaded rolling element forms such a conductive path. Its resistance is determined by the series resistance of the EHL film at both the inner and outer ring contact. The total bearing resistance is derived from the parallel resistance of all loaded rolling elements:

$$R = \left(\sum \frac{1}{\rho \, \dfrac{h_{ci}}{A_i} + \rho \, \dfrac{h_{co}}{A_o}} \right)^{-1} \tag{4.2}$$

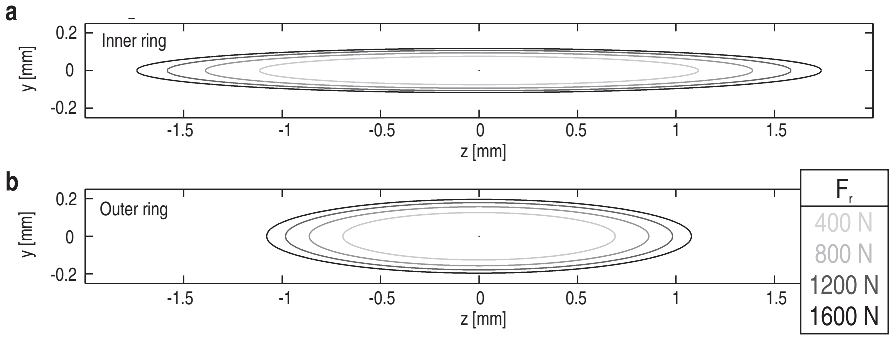

Figure 4.10: Contact geometry on inner ring (**a**) and outer ring (**b**) for four level of the radial load.

The EHL film thickness is nearly uniform over the contact surface (Sect. 2.2.3). It is described by the central lubricant film thickness at the inner ring h_{ci} and the central lubricant film thickness at the outer ring h_{co}. The constriction at the outlet is neglected in the model. The deformed surface takes on contours similar to those of the equivalent dry contact [5, 122]. The contact surface area at the inner ring A_i and the contact surface area at the outer ring A_o are derived from the Hertzian contact theory.

Based on the internal load distribution of Sect. 4.2.2, the contact surface area and the lubricant film thickness are determined for every loaded contact. Also, the lubricant film resistivity ρ is defined. The two angular positions of Fig. 4.3 of a radially loaded bearing are considered. The results of the heaviest loaded rolling element, namely the first element in the first angular position of the rolling element set, are shown in the figures of this section.

Contact surface area

The surface area of each contact is derived using the Hertzian contact theory (Eq. 2.11, 2.12 and 2.13). The surface of the outer raceway is concave while the surface of a rolling element is convex. The surface of the inner raceway is concave in the axial direction and convex in the rolling direction. The contact geometry on the inner and outer ring of the heaviest loaded rolling element is given in Fig. 4.10. The major and minor axis of the elliptical contact are positioned in respectively the axial (z-direction) and rolling direction (y-direction).

Fig. 4.11 shows the contact surface area (**a**) and maximum contact pressure (**b**)

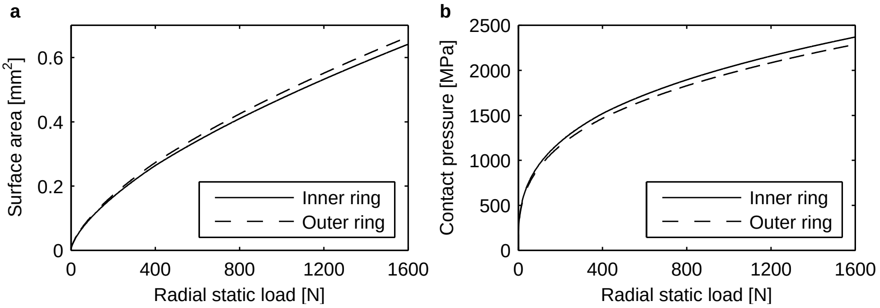

Figure 4.11: Contact surface area (**a**) and maximum contact pressure (**b**) as a function of the radial load.

of the heaviest loaded rolling element. While the contact geometry at the inner and outer raceway is fairly different, the contact surface area is similar. As the surface area on the inner raceway is smaller, the maximum contact pressure is higher. Even with moderate loading of the outer ring, the stresses induced on the surfaces of the rolling elements and raceways are large due to the small contact areas between the mating members [46].

Lubricant film thickness

Hamrock and Dowson [41, 42] established empirical formulas to determine the film thickness under fully flooded isothermal conditions. To this day, the equations are routinely used in EHL film thickness calculations for maximum contact pressures up to 3000 to 4000 MPa [104]. Both for the central lubricant film thickness and the minimum lubricant film thickness, an equation is derived:

$$h_c = 2.69\ r\ \left(\alpha_{pv}\ E'\right)^{0.53} \left(\frac{v_e'\ \eta_0}{E'\ r}\right)^{0.67} \left(\frac{w}{E'\ r^2}\right)^{-0.067} \left(1 - 0.61\mathrm{e}^{-0.73\ \epsilon}\right) \tag{4.3}$$

$$h_0 = 3.63\ r\ \left(\alpha_{pv}\ E'\right)^{0.49} \left(\frac{v_e'\ \eta_0}{E'\ r}\right)^{0.68} \left(\frac{w}{E'\ r^2}\right)^{-0.073} \left(1 - \mathrm{e}^{-0.68\ \epsilon}\right) \tag{4.4}$$

When grease is used as a lubricant, the lubricant film thickness is generally estimated using the properties of the base oil while ignoring the effect of the thickener [46]. The following lubrication and material properties are used:

- Pressure-viscosity index of mineral oil α_{pv}: 25x10^{-9} Pa^{-1} [5, 113].
- Viscosity of mineral oil at 40 °C η_0: 0.05 Pa s [122].
- Reduced modulus of elasticity E': 208x10^9 Pa [7].

The geometry of the contact is taken into account based on two parameters derived in the Hertzian contact theory (Eq. 2.1 and 2.4):

- Reduced radius of curvature r: 0.0028 m (at inner ring) and 0.0047 m (at outer ring).
- Ellipticity parameter ϵ: 14.8 (at inner ring) and 5.51 (at outer ring).

Finally, the following operating conditions determine the film thickness:

- Contact load w: the rolling element load (Sect. 4.2.2).
- Entrainment velocity v_e': 0.6939 m/s (at inner ring) and 0.6939 m/s (at outer ring). The bearing rotates at 1000 r/min and pure rolling is assumed.

The entrainment velocity, as used in the Reynolds equation, is the mean velocity at which the lubricant is dragged into the contact. It is the relative velocity of the lubricant w.r.t. the motion of the contact itself [122]. The kinematics of a single rolling element are analysed in Appendix E. Due to inner ring rotation ω_i, the cage rotates with an angular velocity ω_c and the rolling elements rotate with an angular velocity ω_r. Using Eq. E.17 and E.18, the entrainment velocity at the inner ring v_{ei}' is given by:

$$v_{ei}' = \frac{v_i' + v_{ri}'}{2} = (\omega_i - \omega_c)\,\frac{d_m - D}{4} + \omega_r\,\frac{D}{4} \tag{4.5}$$

Using Eq. E.3, E.8 and E.18, the entrainment velocity at the outer ring v_{eo}' is given by:

$$v_{eo}' = \frac{v_o' + v_{ro}'}{2} = \omega_c\,\frac{d_m + D}{4} + \omega_r\,\frac{D}{4} \tag{4.6}$$

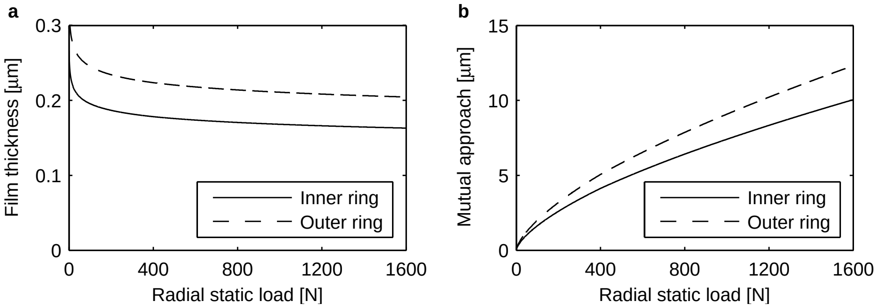

Figure 4.12: Central lubricant film thickness (**a**) and mutual approach (**b**) as a function of the radial load.

The film thickness is unaffected by slip between the rolling bodies as long as the mean entrainment velocity remains the same. Recent research analyses the influence of slip on the film thickness. Ref. [16] experimentally investigates this influence for a single contact between a steel ball and a glass disc. Due to sliding, temperature effects such as inlet heating lead to a reduction of the lubricant viscosity and film thickness. These effects are neglected in common rolling element bearing calculations.

The calculated central lubricant film thickness of the heaviest loaded rolling element is shown in Fig. 4.12**a**. The film thickness declines with load until a certain level where it becomes nearly independent of load [104]. This is a very useful feature of EHL, allowing lubrication under high load. The thickness is compared to the mutual approach δ between the rolling element and raceway in a dry contact (Fig. 4.12**b**). This is the global approach between the contacting bodies, derived using the Hertzian contact theory (Eq. 2.14).

The final polishing process of the manufacturer gives the rolling elements an average surface roughness R_a of about 0.05 µm. The raceways are honed and lapped to about 0.175 µm [63, 122]. Based on Eq. 2.20 and 2.21, the film thickness parameter Λ ranges from 0.6 to 0.9 at the inner raceway and from 0.7 to 1.1 at the outer raceway as a function of the radial load at 1000 r/min. When the inner ring speed increases to 3000 r/min, the film thickness parameter ranges from 1.2 to 1.7 at the inner raceway and from 1.5 to 2.2 at the outer raceway. A film thickness parameter $\Lambda \approx 1$ is often observed and many engineering components operate successfully in this condition [22]. In fact, the majority of rolling element bearings operates in mixed (partial) lubrication regime. Elastic deformation flattening the asperities occurs and elastohydrodynamic lubrication is established between asperities. This still poorly understood process is known as micro-elastohydrodynamic lubrication [104]. The mechanisms of micro-EHL are described by Johnson, Greenwood and Poon [57]. It was found that the average surface separation between two rough surfaces is about the same as predicted for smooth surfaces.

The empirical film thickness formulas of Eq. 4.3 and 4.4 use the properties of the base oil when grease lubrication is applied. The influence of the thickener was analysed by Cann [11, 12]. At low temperature, the grease films are generally thinner than those consisting of the fully flooded base oil due to grease starvation. High viscosity bled lubricant is unable to resupply the contact before the next rolling element arrives. At higher temperature, grease forms a thicker film. An increased local supply of the lubricant is observed due to the lower oil viscosity at higher temperature. A partially flooded EHL film is produced, augmented by a boundary film of deposited thickener. The film thickness may only be a fraction of the thickness calculated for fully flooded oil lubrication conditions. However when the lubricant film is thin, both friction and temperature increase. The viscosity reduces permitting easier return of the lubricant to the contacts [46].

Lubricant film resistivity

Prashad [87] experimentally characterises the resistivity of different greases. Grease is added between two cylindrical brass electrodes. The gap between both electrodes is precisely set. A megaohm meter allows measuring the resistivity of the grease. The resistivity depends on the lubricant viscosity, consistency, applied voltage, additives, etc. When introducing a voltage drop of 10 V over the electrodes, the resistivity of commonly used greases ranges from $6.1\text{x}10^4$ to $3.3\text{x}10^7$ Ωm.

The actual resistivity of a thin EHL film ρ is unknown. In the current study, it is adjusted such that the modelled bearing resistance fits the measured resistance at a radial load of 1000 N and a rotational speed of 1000 r/min. A resistivity of $9.5\text{x}10^4$ Ωm is obtained. This identified resistivity is lower than the average grease resistivity because:

- asperities of the rolling element and raceway surfaces make random metallic contact;
- metallic particles contaminate the lubricant film during the bearing operation;
- the steel cage possibly creates additional conductive paths.

Moreover, the lubricant in the bearing contacts is exposed to high pressure, influencing its resistivity [17].

4.4.2 Lubricant film thickness: influence of the load

The electrical resistance through the test bearing is identified for different radial and axial loads. In Fig. 4.13**a**, the influence of the radial load is visualised. The radial load is continuously increased from 0 to 1600 N at a rate of 20 N/s during the measurement. In Fig. 4.13**b**, the influence of the axial load is visualised. The axial load is continuously increased from 0 to 800 N at a rate of 10 N/s while a 400 N radial load is applied. All measurements are performed at a constant bearing speed of 1000 r/min. The grey lines represent the calculated resistance as a function of time. During rotation of the bearing, current spikes influence the resistance measurement. The spikes appear due to random metallic contact between asperities in the rolling contacts. They increase the noise level and are filtered out before interpreting the results. The signals are smoothed using a moving average filter of 10 s. The black lines show the mean resistance.

Following Eq. 4.3, Hamrock and Dowson predict that the film thickness reduces according to the power of -0.067 when increasing the load. Also, the total surface area of the contacts increases as the load increases. The electrical resistance consequently decreases. The graphs of the radial and axial load run-up are very similar. It is actually the vector sum of both the radial and axial load on each rolling element which determines the film thickness and total surface area of the contacts.

The time fraction of metallic contact is shown in Fig. 4.13**c** and 4.13**d** for respectively the run-up of the radial and axial load. The time signal of the voltage drop over the bearing is divided into blocks of 10 s and the PCT is calculated for each block. The bearing operates under the condition of mixed lubrication as predicted by the model of the previous section. When increasing the bearing load, the film thickness reduces such that metal-to-metal contact occurs more often.

Fig. 4.14 compares the measured and modelled resistance (Sect. 4.4.1) for different values of the radial load. The electrical resistance depends on the position of the cage. The grey area represents all possible values of the resistance when varying this position of the cage. The mean resistance is given by the dashed line. An infinite resistance is calculated at 0 N due to a zero contact surface area. In practice, asperities of the rolling elements and raceways make contact (Fig. 4.13**c**) and a finite resistance is measured. At load levels above 450 N, the correspondence between the model and measurements is good. This, keeping in mind that the resistivity of the lubricant film is tuned such that the measured and modelled resistance coincide at a radial load of 1000 N.

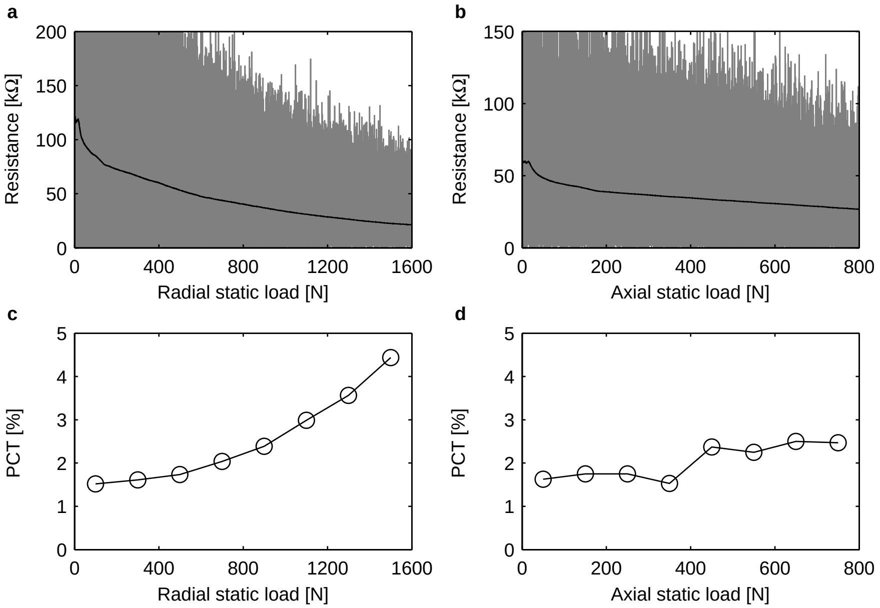

Figure 4.13: Measured electrical resistance (grey lines) and mean electrical resistance (black lines) during a run-up of the radial (**a**) and axial (**b**) load. PCT during the run-up of the radial (**c**) and axial (**d**) load.

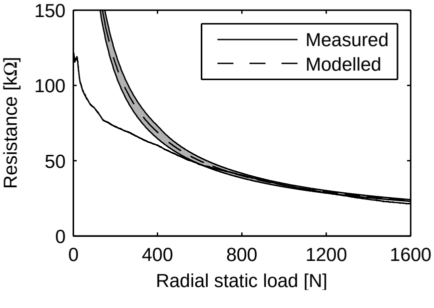

Figure 4.14: Comparison between the measured and modelled electrical resistance. The grey area represents all possible values of the modelled resistance when varying the position of the cage.

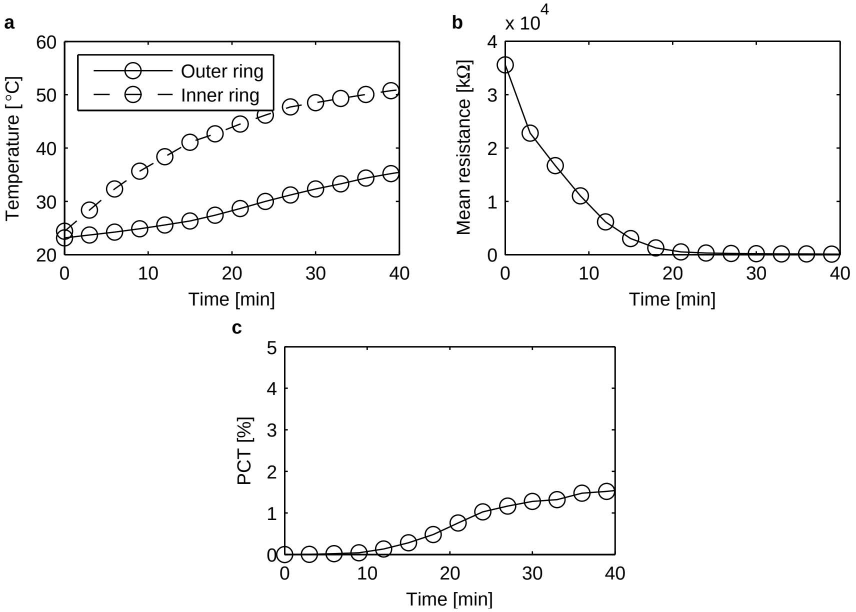

Figure 4.15: Temperature (**a**), electrical resistance (**b**) and PCT (**c**) during a warm-up.

4.4.3 Lubricant film thickness: influence of the temperature

The influence of the bearing temperature on the electrical resistance is measured during a warm-up of the bearing. Starting at room temperature, the resistance is measured while a radial load of 1000 N is applied and the bearing rotates at 1000 r/min. The inner and outer ring temperature and the mean electrical resistance are measured every 3 min. Fig. 4.15**a** and 4.15**b** show the results during the first 40 min of the warm-up.

Following Eq. 4.3, Hamrock and Dowson predict that the film thickness is linked to the lubricant's viscosity according to the power of 0.67. As the lubricant's viscosity decreases exponentially with increasing temperature (Eq. 2.18), a significant reduction of the film thickness is expected. In addition, the resistivity of the lubricant decreases with increasing temperature. During the first 20 min of the bearing warm-up, the lubricant heats up strongly and the electrical resistance reduces drastically. Its value diminishes from 3.5×10^7 Ω to 5.1×10^5 Ω.

The time fraction of metallic contact is shown in Fig. 4.15**c**. The PCT is calculated every 3 min. No metallic contact is observed during the first 10 min

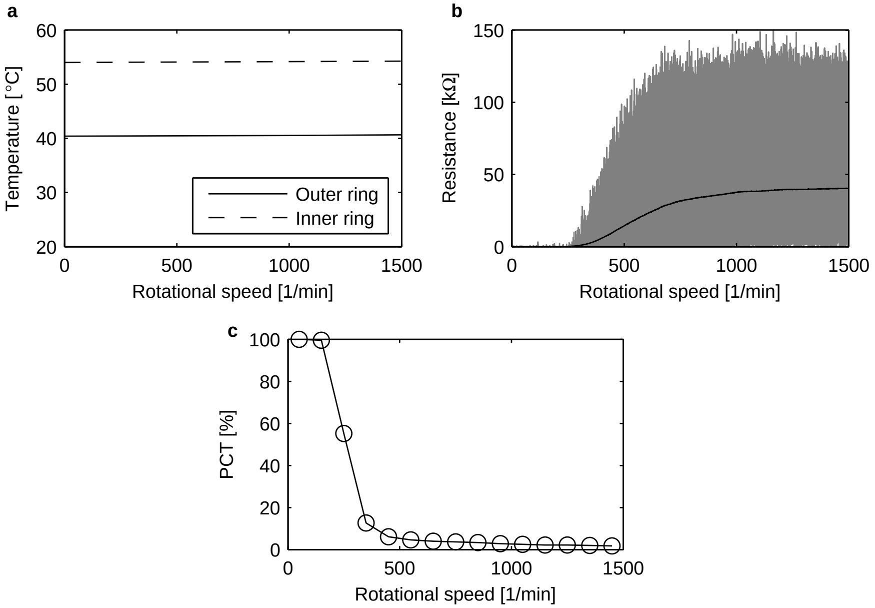

Figure 4.16: Temperature (**a**), electrical resistance (**b**) and PCT (**c**) during a run-up of the speed. Both the calculated resistance (grey line) and the mean resistance (black line) are shown.

of the warm-up. As the lubricant's temperature increases, the lubricant's viscosity and film thickness decrease. The amount of metal-to-metal contact consequently increases. Increasing metallic contact in turn leads to an increase of the temperature. An equilibrium is only reached after several hours, when the mean electrical resistance and PCT reach their steady-state values. The mean electrical resistance and PCT are then respectively $40\text{x}10^3$ Ω and 2.7%.

4.4.4 Lubricant film thickness: influence of the speed

To analyse the influence of the rotational speed on the electrical resistance, the speed is increased from 0 to 1500 r/min. The speed is continuously increased at a rate of 20 (r/min)/s. A radial load of 1000 N is applied on the bearing. The measurement of the electrical resistance starts after the bearing reached its stable temperature at 1000 r/min. Fig. 4.16**a** and 4.16**b** show respectively the temperature and measured resistance through the bearing during the run-up.

To obtain the mean resistance (black line), the measured resistance is smoothed using a moving average filter of 10 s. Isothermal conditions are assumed.

The mean electrical resistance reveals the formation of a lubricant film inside the bearing. Around 200 r/min, the lubricating film in the rolling contacts of both the inner and outer raceway starts to form. At a speed of 1200 r/min, the formation of the film is complete. Further increase of the lubricant film thickness is not possible. Bulk lubricant, pushed aside by the passage of a rolling element, does not have the time to reflow into the track before the next element arrives. Starvation of the lubricant film occurs [13]. Fig. 4.16**c** shows the PCT, calculated using blocks of 5 s. The PCT decreases from 100% to approximatly 3% during the formation of the lubricant film.

4.5 Cage slip

During the operation of rolling element bearings, the speed of the cage deviates from its theoretical value based on the bearing kinematics. This slip of the cage has been investigated since the beginning of the 1960s. Its importance is emphasised in different studies, aiming to understand the bearing behaviour.

Bearings operating at light loads and high speeds, such as the main shaft bearings of gas turbine engines, can experience significant cage and rolling element slip. This condition of gross sliding is called skidding [46]. Skidding between the rolling elements and raceways causes increased wear of the surfaces, if the lubricant film is insufficient to separate the different bodies [95, 112]. The influence of the load and speed [6, 43], oil viscosity [86, 100], internal clearance [6, 100], frictional forces [23] and curvature [40] on cage slip of different types of ball and roller bearings is investigated in the literature.

Damaged bearings excite their surrounding structure at characteristic frequencies. These characteristic frequencies are determined by the cage and rolling element speed. Diagnosis techniques based on their occurrence should take into account possible shifts. A recent publication of Pennacchi [82] investigates the influence of cage and roller slip on the characteristic frequencies of a bearing. The radial bearing load is varied while the different characteristic frequencies are tracked.

This section discusses cage slip of the test bearing for different operational conditions. First, the cause of cage slip is presented. To interpret the measurement results, the kinematics of the test bearing are analytically investigated afterwards. Finally, the measurement results are reviewed.

4.5.1 Cause of cage slip

Even though called rolling element bearings, the major source of friction in bearings is sliding. A contact surface is formed when a load is applied between the rolling element and raceway. During rotation of a rolling element relative to the raceway surface, a combination of rolling and sliding motion occurs.

If no lubrication is applied or in case of solid lubrication, sliding in ball bearings occurs due to the basic internal geometry of the bearing. Pure rolling only appears in two points of the contact. In all other points, sliding in the direction parallel to the rolling motion occurs. If a full lubricant film is formed, the friction depends wholly on the properties of the lubricant. When the lubricant film is insufficient to completely separate the rolling surfaces ($\Lambda < 3$), asperities break through the lubricant film. The sliding friction shear stress during this asperity-asperity interaction occurs in the regime of boundary lubrication. Only a portion of the contact however operates in this manner. The remainder of the contact surface operates according to fluid-fluid lubrication. The friction shear stress is a combination of both [46].

Besides friction in the rolling contacts, other sources of friction are [46]:

- Viscous drag on the rolling elements.

  During operation, a certain amount of lubricant occupies the free space within the boundaries of the bearing. Because of their orbital motion, the balls or rollers must force their way through this fluid. The viscous fluid creates a drag force that retards the orbital motion.

- Sliding friction between the rolling elements and cage pockets.

  At any given azimuth location, there is generally a normal force acting between the rolling element and its cage pocket. The rolling element can drive the cage or vice versa. The amount of friction that occurs depends on the normal force, lubricant properties, rolling element speeds and cage pocket geometry.

- Sliding friction between the bearing rings and cage.

  In some bearings built for rather critical applications, the cage is partly driven by one of the rings because of a sliding contact in between. In most bearings however, there is no contact between the rings and cage.

- Sliding friction between the roller ends and ring flanges in roller bearings.

- Sliding friction in the seals, keeping the lubricant inside the bearing.

All these occurrences of friction define the sliding motion of the cage and rolling elements. To understand the full behaviour of the cage and rolling elements, sophisticated numerical analysis of forces and moments is required [5]. Harris [43, 44, 45] extensively investigated the cage slip for an axially loaded angular contact bearing by deriving each of the friction terms and solving the equations of motion. He shows that the results of his model correspond well to the measured cage slip. An analytical formulation for the generalised ball, cage and raceway motion in a ball bearing and the generalised roller motion in a cylindrical roller bearing is given by Gupta [35, 36, 37, 38, 39].

4.5.2 Analysis of cage slip

In the current study, cage slip of the test bearing is evaluated based on the deviation of the measured ball pass frequency (BPF) from its theoretical value. As discussed in Sect. 4.3.1, the main excitation of the test bearing is the motion at the BPF. This excitation is clearly identified in the spectrum of the radial bearing displacement. The BPF is the frequency at which a rolling element is passing the loaded zone. As the test bearing contains seven rolling elements, the BPF equals seven times the cage frequency. This proportionality allows evaluation of the actual speed based on the BPF. The theoretical value of the BPF is derived from the nominal bearing geometry and assumes perfect rolling of the rolling elements.

In the next two sections, the BPF is analytically investigated. Firstly, the influence of inner and outer ring slip on the BPF (and BSF) is analysed. Secondly, the influence of internal clearance on the BPF (and BSF) is analysed. These relations are needed when interpreting the measurement results. Afterwards, the measurement results are discussed. The influence of the bearing load, temperature and speed on the cage slip is analysed. For different operational conditions, the BPF is measured using the spectrum of the radial bearing displacement. A measurement time of 180 s is employed to obtain a frequency resolution of 0.0055 Hz.

While cage slip is easily measured, rolling element slip is not. Only when fatigue spalls are present on the rolling elements, an excitation at the ball spin frequency (BSF) is seen. This excitation would allow evaluating the rolling element slip. The spall however affects the BSF itself. Kawakita [61, 62] measures the BSF using magnetised rolling elements and Hall sensors on the cage. This technique is applicable for large bearings. With the test rig presented in this work, the BSF cannot be measured. The analytical analyses of the next two sections does consider the BSF.

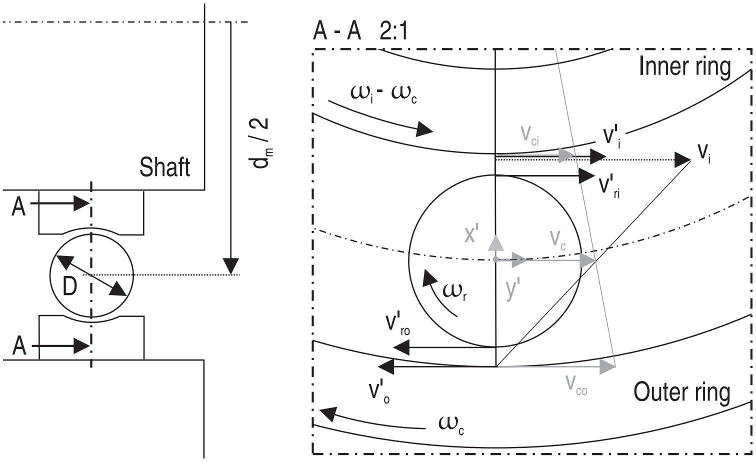

Figure 4.17: Kinematics of a rolling element, described in a moving coordinate system x′y′.

4.5.3 BPF and BSF versus inner and outer ring slip

The two-dimensional (2D) kinematics of one rolling element are analysed using Fig. 4.17. They are described in a moving coordinate system x′y′, fixed to the cage and rotating with angular velocity ω_c. The rolling element experiences slip at both the inner and outer ring. Appendix E derives the angular velocity of the cage ω_c and the angular velocity of the rolling elements ω_r. The analysis assumes that the DGBB is only loaded in its radial direction, such that the contact angle α equals $0\,^\circ$.

Knowing the number of rolling elements Z and the angular velocity of the cage and rolling elements, the BPF and BSF are given by:

$$BPF = \frac{\omega_c}{2\pi}\ Z = \frac{\omega_i\ Z}{4\pi}\ \frac{d_m - D}{d_m} + \frac{s_0 - s_i}{d_m} \tag{4.7}$$

$$BSF = \frac{\omega_r}{2\pi} = \frac{d_m\ \omega_i}{4\pi\ D}\ \left(1 - \left(\frac{D}{d_m}\right)^2\right) - \left(\frac{s_o - s_i}{d_m}\ \frac{d_m - D}{D} + \frac{2\ s_i}{D}\right) \tag{4.8}$$

The first term of these expressions represents the BPF and BSF in the absence of slip, as derived in Ref. [46]. The second term represents the deviation of

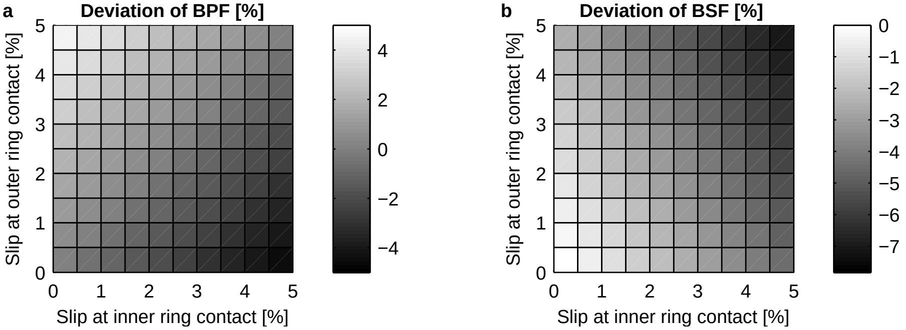

Figure 4.18: Deviation of BPF (**a**) and BSF (**b**) due to slip at inner and outer ring contact.

the BPF and BSF due to slip. The slip at the inner ring contact s_i and outer ring contact s_o is defined as the difference between the relative velocity of the raceway and the rolling element.

Based on Eq. 4.7 and 4.8, Fig. 4.18 shows the deviation of the BPF and BSF due to slip. The slip is given as a ratio w.r.t. the inner ring speed v_i. Whether the BPF is higher or lower than its theoretical value depends on the difference between the slip at the inner and outer ring contact. If the slip at the inner ring contact is higher, the BPF is lower than theoretically expected. This behaviour is referred to as positive cage slip [100]. If the slip at the outer ring contact is higher, the BPF is higher. Negative cage slip occurs. The BSF is always smaller than its theoretical value when slip occurs.

4.5.4 BPF and BSF versus clearance

A deep groove ball bearing is generally designed to have internal radial clearance. The radial clearance is the maximum distance within which one ring can move freely and radially [102]. The radial clearance P_d results in axial clearance which disappears when an axial load is applied. A contact angle α_0 different from $0\,^\circ$ is then formed (Fig. 4.19). Harris [46] derives an expression for α_0 using the radial clearance P_d, the inner raceway radius of curvature r_i, the outer raceway radius of curvature r_o and the rolling element diameter D. Here, the inner and outer raceway radius of curvature correspond to the radius of curvature $r_{1(I)}$ of the Hertzian contact theory from Sect. 2.1.1. The contact angle α_0 is given by:

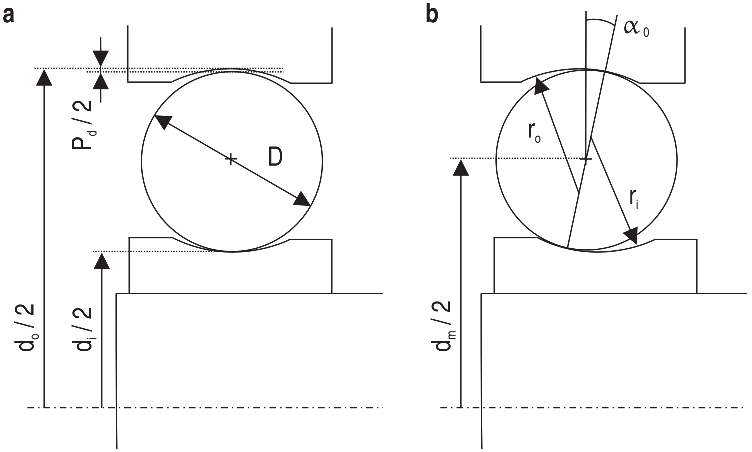

Figure 4.19: Deep groove ball bearing when no load is applied (**a**) and the formation of a contact angle when an axial load is applied (**b**).

$$\cos(\alpha_0) = 1 - \frac{P_d}{2\ (r_o + r_i - D)} \tag{4.9}$$

The axial clearance (also called free endplay) is the maximum distance within which one ring can move freely and axially. The axial clearance P_e is given by the following equation [46]:

$$P_e = 2\ (r_o + r_i - D)\ \sin(\alpha_0) \tag{4.10}$$

Based on Eq. 4.9 and 4.10, Fig. 4.20**a** and 4.20**b** show the contact angle and axial clearance w.r.t. the radial clearance. This analysis does not take into account the flexibility of the inner and outer ring contacts. The fixed contact angle is formed once an axial load is applied. In practice, the contact angle further increases when increasing the axial load due to the flexibility of the contacts. A simulation of Ref. [7] shows a 70% further increase of the contact angle after applying a high axial load of 0.2xC_0 on a DGBB. Also, each rolling element experiences a different contact angle when a radial and axial load are combined.

When introducing the contact angle α_0, the effective inner and outer raceway diameter change. The BPF an BSF consequently change. The theoretical increase of the BPF an BSF is also analysed in Ref. [103]. In the absence of slip, the BPF and BSF are given by [46]:

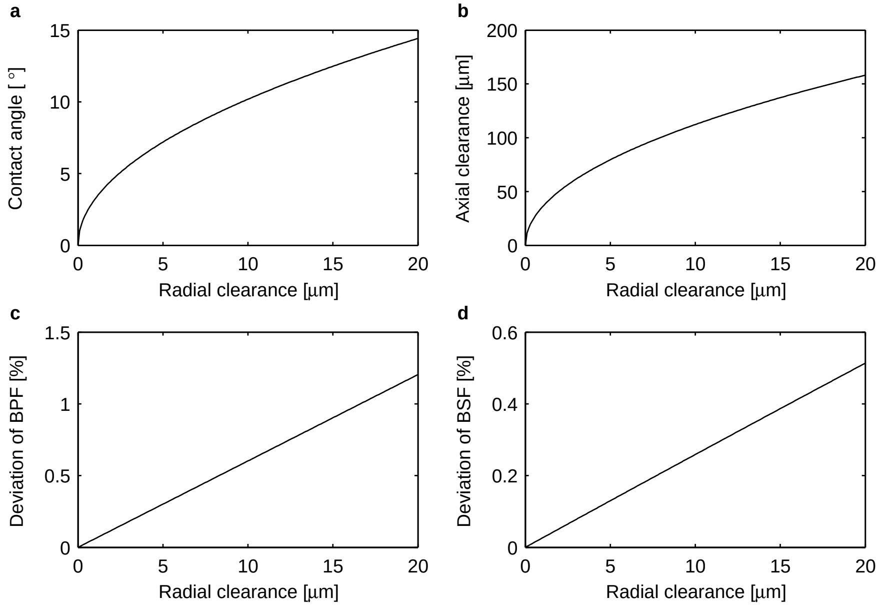

Figure 4.20: Contact angle (**a**) and axial clearance (**b**) due to radial clearance. Deviation of the BPF (**c**) and BSF (**d**) due to radial clearance.

$$BPF = \frac{\omega_c}{2\pi}\ Z = \frac{\omega_i\ Z}{4\pi}\ \frac{d_m - D\ \cos(\alpha_0)}{d_m} \tag{4.11}$$

$$BSF = \frac{\omega_r}{2\pi} = \frac{d_m\ \omega_i}{4\pi\ D}\ \left(1 - \left(\frac{D\ \cos(\alpha_0)}{d_m}\right)^2\right) \tag{4.12}$$

Based on these equations, the deviation of the BPF and BSF as a function of the radial clearance is shown in respectively Fig. 4.20**c** and 4.20**d**.

4.5.5 Cage slip: influence of the load

The effect of a radial and axial static load on the cage slip of the test bearing is experimentally analysed. Firstly, the radial load is increased from 0 to 1600 N. Secondly, the axial load is increased from 0 to 800 N while an 400 N radial load is applied. All measurements are performed at a constant bearing speed of 1000 r/min. The influence of the radial and axial load on the BPF is shown

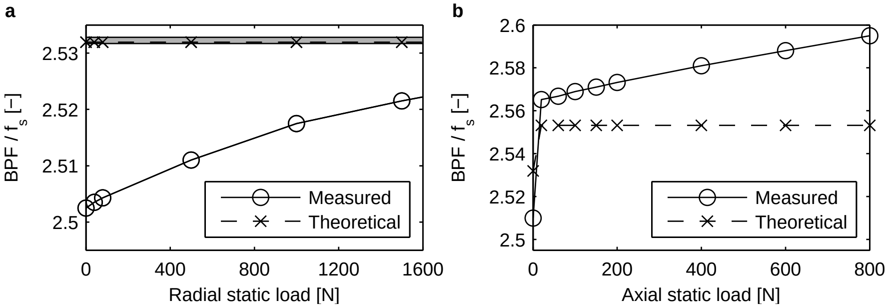

Figure 4.21: BPF w.r.t. the rotational frequency of the shaft f_s during a run-up of the radial (**a**) and axial (**b**) load. Both the measured (solid lines) and theoretical (dashed lines) BPF are shown. The grey area indicates the scatter on the theoretical BPF due to geometrical changes.

in Fig. 4.21. The solid line indicates the measured BPF w.r.t. the rotational frequency of the shaft f_s. Based on the nominal bearing geometry, the dashed line indicates the theoretical BPF w.r.t. the rotational frequency of the shaft. The theoretical BPF assumes perfect rolling and is given by the first term of Eq. 4.7.

When increasing the radial load, the BPF converges to its theoretical value and the cage slip reduces. Similar observations were made by Poplawski [86] and Pennacchi [82]. The BPF is lower than its theoretical value, indicating that more slip is occurring at the inner raceway contact than the outer raceway contact (Sect. 4.5.3). A reduction of the lubricant film thickness at higher radial load levels is discussed in Sect. 4.4.2. It is however not possible to prove that the cage slip reduces due to a decrease of the film thickness.

When introducing a small axial load, the BPF clearly shifts. More slip at the outer raceway contact than the inner raceway contact is now observed. The theoretical BPF (dashed line) takes into account the effective inner and outer raceway diameter as a function of the contact angle. A contact angle different from zero degrees is formed (Sect. 4.5.4). With an estimated radial clearance of 14 µm (Sect. 4.1.2), the BPF increases by 0.84% when a contact angle of 12.1 ° is formed. The measured increase of the BPF is much more pronounced. The axial load not only affects the effective inner and outer raceway diameter, the loaded zone of the bearing drastically changes. The load is no longer transferred by two or three rolling elements. Now, all rolling elements transfer a part of the load changing the friction behaviour between the rolling elements and raceways.

When increasing the axial load, the BPF diverges from its theoretical value as the cage slip increases. Simultaneously, the lubricant film thickness reduces (Sect. 4.4.2). A reduced lubricant film thickness consequently does not imply a reduction of the cage slip. The cage slip is determined by the complex load distribution over the different rolling elements. As the actual rolling element load depends on the position of the rolling element, each rolling element experiences a different contact angle and thus tries to roll at a different speed. The cage ensures that the mean speed of all rolling elements is the same by causing some random slip [88].

The grey area around the dashed line in Fig. 4.21**a** indicates the possible scatter on the theoretical BPF due to geometrical changes. The scatter is estimated based on the operational clearance provided by the bearing manufacturer. This clearance takes into account the manufacturing tolerances, the bearing temperature and the mounting fits. The relation between the internal bearing dimensions and the clearance is given by Eq. 4.1. The nominal bearing dimensions (Appendix D) assume zero radial clearance. The operational clearance ranges from -4 to 14 μm according to the bearing manufacturer. The BPF is maximal when the rolling element diameter is 7 μm smaller than its nominal value. The radial clearance then equals 14 μm instead of the nominal 0 μm. The BPF is minimal when the rolling element diameter is 2 μm bigger than its nominal value. The radial clearance then equals -4 μm instead of the nominal 0 μm.

4.5.6 Cage slip: influence of the temperature

The influence of the bearing temperature on the cage slip is experimentally analysed during a warm-up of the bearing. Starting at room temperature, the radial displacement is measured every 3 min. A radial load of 1000 N is applied and the bearing rotates at 1000 r/min.

During the first 10 min of the warm-up, the lubricant's viscosity strongly decreases (Sect. 4.4.3). This changes the friction behaviour in the contacts. Following Fig. 4.22, only a small variation of the BPF due to the reduction of the viscosity is observed.

It should be noted that the temperature affects the internal bearing geometry. This effect is discussed in the previous section. A 10 °C temperature difference between the inner and outer ring is measured during operation. Based on this difference, a variation of the BPF during the warm-up of 0.003% is expected. The effect is thus negligible.

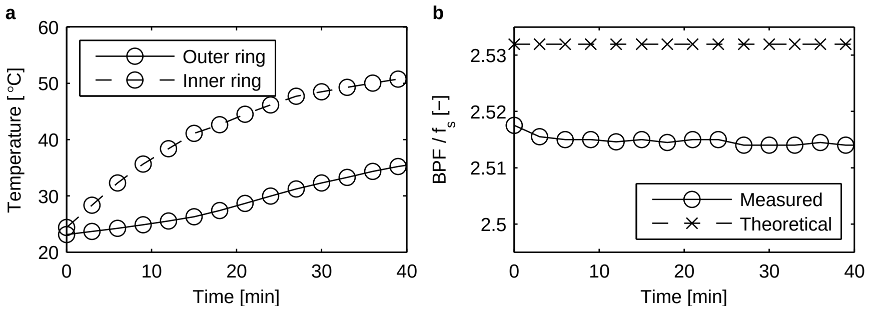

Figure 4.22: Temperature (**a**) and BPF w.r.t. the rotational frequency of the shaft f_s (**b**) during a warm-up. Both the measured (solid lines) and theoretical (dashed lines) BPF are shown.

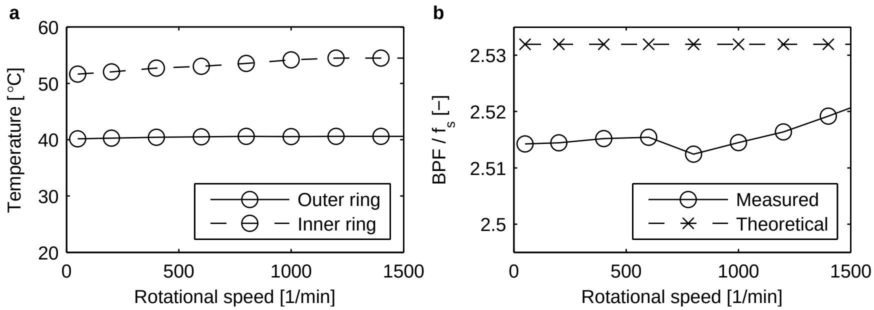

Figure 4.23: Temperature (**a**) and BPF w.r.t. the rotational frequency of the shaft f_s (**b**) during a run-up of the speed. Both the measured (solid lines) and theoretical (dashed lines) BPF are shown.

4.5.7 Cage slip: influence of the speed

To analyse the effect of the rotational speed on the cage slip, the speed is increased from 0 to 1500 r/min. A 1000 N radial load is applied. Isothermal conditions can be assumed. The BPF is divided by the rotational frequency of the shaft to allow comparison at different speeds. The result is shown in Fig. 4.23. The formation of the lubricant film is analysed in Sect. 4.4.4. The BPF mostly varies during the formation of the lubricant film between 500 and 1000 r/min. Overall, the effect of the speed is rather small.

4.6 Load identification

In the final section of this chapter, the potential to estimate the bearing load using the operational properties is discussed. Identification of the bearing load during operation is of particular interest in many applications. The actual bearing load or detection of overloading can significantly improve the evaluation of the remaining useful life.

The amplitude at the BPF is strongly influenced by the bearing load, but also affected by the structure's dynamics. Estimation of the bearing load is only possible when the operational speed and structure's dynamics are constant. When the operational speed varies, the structure's dynamics should be characterised beforehand.

The electrical resistance through the bearing is strongly influenced by the bearing load, but also affected by the temperature and speed. The complex relation between the bearing load and the lubricant's temperature complicates the load estimation. Furthermore, long measurements of the resistance are required to obtain consistent values, which hampers detecting rapid variations of the load.

The BPF only experiences small variations when the load changes. A high frequency resolution is required to detect these variations. Rapid variations of the load cannot be detected, as long measurements are required.

In stationary operating conditions, the amplitude at the BPF is the most appropriate indicator of the actual bearing load. When the rotational speed of the bearing fluctuates, order tracking of the BPF should be considered. More research on the applicability is however required.

4.7 Conclusion

Three operational properties of the test bearing are investigated: the bearing motion, the behaviour of the lubricant film and cage slip. The properties are measured using techniques which can be applied in most rotating machinery. The motion and cage slip are derived from the radial bearing displacement while the lubricant film behaviour is derived from the electrical resistance through the bearing.

During rotation, the finite number of loaded rolling contacts introduces continuous variation of the bearing deformation. This effect of variable elastic compliance results in a strong excitation at the ball pass frequency. At higher levels of the radial load, the variation of the bearing deformation during rotation increases. The excitation at the BPF consequently increases. At higher levels of the axial load, an opposite trend is observed. Also, a highly pronounced excitation is seen when the BPF corresponds to the frequency of a structural resonance.

The measured electrical resistance through the bearing reveals the behaviour of the lubricant film and allows detection of metallic contact. As the bearing load increases, the film thickness decreases and the contact surface area increases. Metal-to-metal contact between the rolling elements and raceways occurs more often. As the lubricant's temperature increases, the lubricant's viscosity decreases exponentially such that the film thickness reduces. Metallic contact is only detected after a considerable decrease of the film thickness. As the bearing speed increases, the formation of the lubricant film is revealed.

A few percent of sliding motion between the rolling elements and raceways results in cage slip. Depending on the operational conditions, cage slip up to approximately 1% is detected. Cage slip is reduced when increasing the radial static load. After introducing a small axial load, the effective inner and outer raceway diameter change and all rolling elements transfer a part of the bearing load. A clear shift of the cage slip is observed. The effect of the bearing temperature and speed on cage slip is small.

Clean analysis of the bearing motion and cage slip proves precise operation of the test rig. The different spectral components of the bearing displacement are linked to the theoretical bearing motion. Excitation at the rotational frequency of the shaft and its harmonics reveals a small eccentricity between the auxiliary and main shaft of the test rig. This eccentricity cannot be avoided when collet chucks are adopted. Excitation of the spindle bearings is negligible w.r.t. the test bearing excitation.

Chapter 5

Dynamic behaviour of the test bearing

Accurate knowledge on the bearing dynamic properties is essential during the design of rotating machinery. These properties determine the machine's critical speeds, the forces acting on the different components, etc. The current study investigates the stiffness and damping characteristics of the test bearing in the direction of the radial static bearing load.

The stiffness of rolling element bearings is mainly determined by the Hertzian deformation between the rolling elements and raceways. The lubricant film influences this stiffness of the contacts. Bending of the outer ring and deformation of the interferences between the housing, bearing and shaft further determine the bearing stiffness.

There are three major sources of damping in rolling element bearings [19]. Firstly, lubricant film damping generated within the contacts between the rolling elements and raceways. Secondly, material damping due to Hertzian deformation of the rolling bodies as well as frictional losses caused by metallic contact between rolling elements and raceways. Thirdly, damping generated in the interference between the housing, bearing and shaft.

Identification of the bearing stiffness and damping is based on the dynamic response of the test rig. The test rig is dynamically excited using an electrodynamic shaker while its response is measured using an accelerometer. Fitting a spring-mass-damper model of the test rig to the measured response allows identifying the bearing dynamic properties. The behaviour of the lubricant film between the rolling elements and raceways is simultaneously measured based on the electrical resistance through the bearing.

The dynamic properties of the test bearing structure are identified for different conditions of the load and lubricant film. While the influence of the bearing load on the stiffness is well described in the literature, little information about the influence of the lubricant film is provided. Variation of the bearing temperature and speed reveals the influence of the lubricant film on the bearing stiffness and damping.

The method to accurately identify the bearing stiffness and damping is reviewed in Sect. 5.1. Sect. 5.2 describes the dynamic properties for different levels of the radial and axial load. The influence of the bearing temperature and speed are discussed in respectively Sect. 5.3 and 5.4.

5.1 Identification of the stiffness and damping

This section presents the identification of the test bearing stiffness and damping, based on the dynamic response of the test rig. After selecting the appropriate excitation signal, the dynamic behaviour of the bearing structure is analysed using the modal analysis technique. An analytical model of the test rig is fitted to the measured data to identify the test bearing stiffness and damping. The effect of an error in the model on the identification is checked. Finally, the stiffness identification is validated using a dummy bearing with a known stiffness.

5.1.1 Excitation signal and level

To identify the dynamics of the bearing structure, stepped sine excitation is used. With stepped sine excitation, all the input energy is concentrated at the frequency of excitation. Noise and harmonics in the response signal at frequencies distinct from the excitation frequency are discarded. As such, the signal-to-noise ratio is superior to random or transient excitation methods. The main disadvantage of using stepped sine excitation is a longer measurement time to identify the system. At each stepped frequency increment, time is required to attain a steady-state condition of the response [51, 125].

Fig. 5.1 shows a measured frequency response function (FRF) between the input force of the radial shaker and the acceleration of the bearing housing for two different excitation methods. During the measurement, the bearing rotates at 1000 r/min and a 400 N radial static load is applied. Both the input

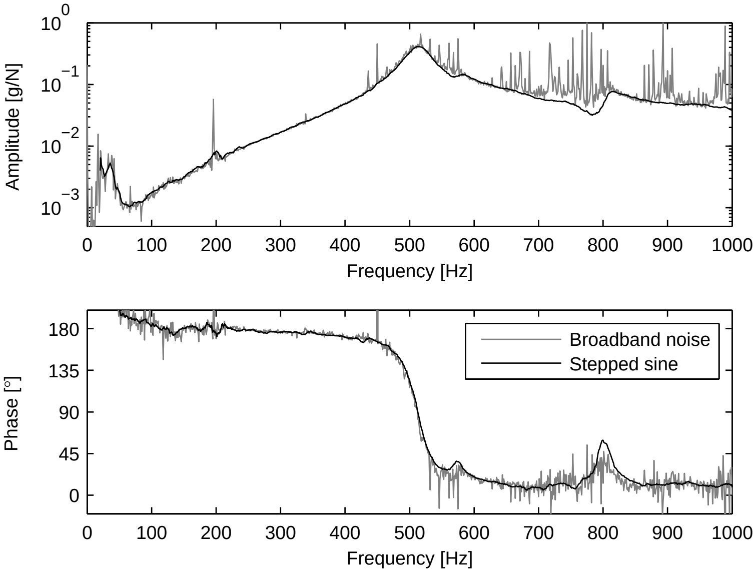

Figure 5.1: Comparison between broadband noise and stepped sine excitation. The FRF between the measured input force and a measured housing response is visualised for both excitation signals.

force and acceleration are measured in the direction of the static bearing load. The test bearing and the spindle bearings generate vibrations during rotation (Sect. 4.3). The FRF identified using broadband noise (grey line) is affected by these vibrations. The FRF identified using stepped sine excitation (black line) provides clean information on the structure's dynamics.

The excitation level is controlled in a feedback loop and steered to a constant force at each frequency. A system identification step prior to stepped sine excitation is used to control the excitation level. The assumption of linearity for small excitations of the system is checked by performing the same test at different shaker excitation levels. The amplitude of the exciting sine ranges from 1 to 5 N. Linearity can be assumed for analyses up to 1400 Hz. Below this frequency, the FRFs measured at different excitation levels coincide well. Above this frequency, differences between the FRFs are observed. This conclusion only holds for excitation levels being several orders of magnitude smaller than the static bearing load. Significant variations of the bearing load do influence the bearing response, as further discussed in Sect. 5.2.1.

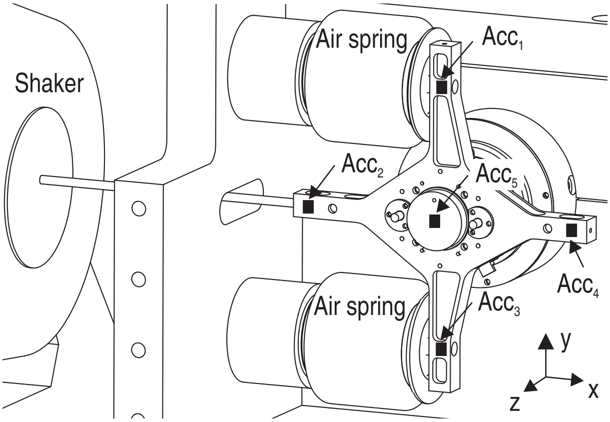

Figure 5.2: Set-up during the modal analysis of the test bearing housing. An electrodynamic shaker excites the system while five accelerometers measure the housing response.

5.1.2 Dynamic bearing response

In the presented test rig, the inner ring of the test bearing is mounted on a rigid shaft. The outer ring is mounted in a floating housing supported by flexible air springs. When applying an external dynamic load on the bearing, the rigid body modes of this housing show up as the main resonances. Changing the bearing load, rotational speed or operational temperature affects the stiffness and damping characteristics of the bearing. The resonance frequencies and damping ratios of the rigid body modes are used to identify the dynamic characteristics of the test bearing.

The rigid body modes of the housing mass have been identified by conducting a modal test. Five triaxial accelerometers measure the housing motion while the radial shaker excites the system. Fig. 5.2 shows the set-up. Only the radial air springs and shaker are mounted. The air springs apply a static load of 400 N and the bearing rotates at 1000 r/min.

Below 100 Hz, the following rotational rigid body modes are identified:

- 33 Hz: rotation of the housing around the y-axis.
- 78 Hz: rotation of the housing around the x-axis.
- 92 Hz: rotation of the housing around the z-axis.

These modes are mainly determined by the stiffness of the air springs and the shaker stinger, as the tilt stiffness of the bearing is very small. Above 100 Hz, the following translational rigid body modes are identified:

- 141 Hz: translation of the housing in the z-direction.
- 426 Hz: translation of the housing in the y-direction.
- 512 Hz: translation of the housing in the x-direction.

These modes are mainly determined by the radial and axial stiffness of the test bearing. In the absence of the radial (and axial) static load, the axial stiffness of the bearing is zero. The outer ring is free to float axially (Sect. 4.5.4). By introducing a 400 N radial load, Hertzian contacts in the loaded zone of the bearing are formed. The bearing obtains some axial stiffness which is highly dependent on the radial load.

The six rigid body modes, corresponding to the six degrees of freedom of the housing mass, appear separately and uncoupled. As explained in Sect. 3.2.3, the vibrating structure is balanced. In this way, the dynamic load acts through the centre of the bearing. If this condition would not be fulfilled, the modes would be coupled. For example, a small tilt movement could be observed at the resonance frequency of a translational mode.

In the current study, the bearing stiffness and damping in the direction of the radial static load are investigated. The translational mode in the x-direction is used to identify these dynamic characteristics. The resonance frequency of this mode varies between 485 and 588 Hz, as a function of the operational conditions. The damping ratio varies between 1.9% and 3.2%. In the next section, the bearing stiffness and damping are derived from this measured resonance frequency and damping ratio.

5.1.3 Model for stiffness and damping identification

In order to estimate the bearing stiffness and damping, a reduced spring-mass-damper model of the test rig is developed. The model is shown in Fig. 5.3. It simulates the radial acceleration of the bearing housing (w.r.t. the radial force F). The model is fitted to the measured radial acceleration of the bearing housing (w.r.t. the radial shaker force $F_{r,d}$). In this way, the stiffness and damping of the test bearing are identified.

Recalling Sect. 3.3.2, the test rig is designed to analyse the bearing dynamics in the range from 25 to 500 Hz. It is shown that the test bearing housing and the

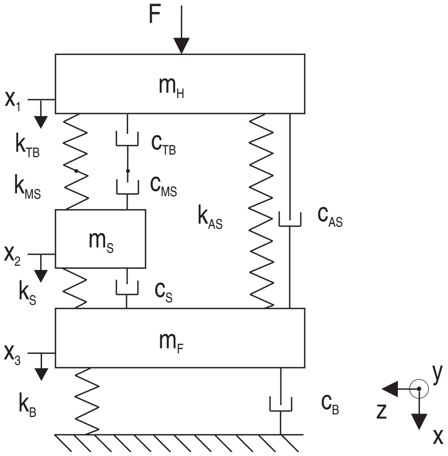

Figure 5.3: Analytical model describing the radial acceleration of the bearing housing.

frame have their first flexible mode at respectively 618 and 638 Hz. They are considered being rigid in the range from 25 to 500 Hz and represented by a point mass m_H and m_F in the model. The spindle has a first flexible mode at 1899 to 1915 Hz (depending on the test bearing load) which results in a significant radial motion of the test bearing seat. For excitations up to this resonance frequency, the spindle is represented by a mass m_S, a bending stiffness k_S and an equivalent damping c_S. The mass of the bearing housing m_H, the spindle m_S and the frame m_F each have one degree of freedom: x_1, x_2 and x_3.

The housing, spindle and frame are connected to each other through a set of springs and dampers. The stiffness and damping between the bearing housing and the spindle is determined by the test bearing and the modular mounting system. The test bearing is represented by the stiffness k_{TB} and the damping c_{TB}. The mounting system is represented by the stiffness k_{MS} and the damping c_{MS}. Air springs are located between the bearing housing and the frame to provide a static load on the test bearing. The air springs have a combined stiffness k_{AS} and damping c_{AS}. The frame is mounted on bushings having a combined stiffness k_B and damping c_B.

The motion of the housing, spindle and frame w.r.t. the radial force F is described by the FRF matrix of the system. An equation of motion is derived for each degree of freedom. In matrix notation, the following differential equation describes the total system:

$$\underline{\underline{M}}\,\underline{\ddot{x}} + \underline{\underline{C}}\,\underline{\dot{x}} + \underline{\underline{K}}\,\underline{x} = \underline{F} \tag{5.1}$$

The mass matrix $\underline{\underline{M}}$, the stiffness matrix $\underline{\underline{K}}$, the damping matrix $\underline{\underline{C}}$, the displacement vector $\underline{X}$ and the force vector $\underline{F}$ are respectively given by:

$$\begin{gathered}
\underline{\underline{M}} = \begin{bmatrix} m_H & 0 & 0 \\ 0 & m_S & 0 \\ 0 & 0 & m_F \end{bmatrix} \\
\underline{\underline{K}} = \begin{bmatrix} k_{TB+MS} + k_{AS} & -k_{TB+MS} & -k_{AS} \\ -k_{TB+MS} & k_{TB+MS} + k_S & -k_S \\ -k_{AS} & -k_S & k_S + k_B + k_{AS} \end{bmatrix} \\
\underline{\underline{C}} = \begin{bmatrix} c_{TB+MS} + c_{AS} & -c_{TB+MS} & -c_{AS} \\ -c_{TB+MS} & c_{TB+MS} + c_S & -c_S \\ -c_{AS} & -c_S & c_S + c_B + c_{AS} \end{bmatrix} \\
\underline{x} = \begin{bmatrix} x_1 \\ x_2 \\ x_3 \end{bmatrix} \\
\underline{F} = \begin{bmatrix} F \\ 0 \\ 0 \end{bmatrix}
\end{gathered} \tag{5.2}$$

In these equations, the combined stiffness k_{TB+MS} and damping c_{TB+MS} are given by:

$$\begin{gathered}
k_{TB+MS} = \left(\frac{1}{k_{TB}} + \frac{1}{k_{MS}}\right)^{-1} \\
c_{TB+MS} = \left(\frac{1}{c_{TB}} + \frac{1}{c_{MS}}\right)^{-1}
\end{gathered} \tag{5.3}$$

Transforming Eq. 5.1 to the frequency domain yields the FRF matrix of the system.

Table 5.1: Values of the model parameters.

Parameter	Derived from	Value
m_H	Weighing	2.57 kg
m_S	Curve fitting	2.81 kg
m_F	Curve fitting	205 kg
k_{MS}	Curve fitting	114x10^6 N/m
k_{AS}	Data sheet	650x10^3 N/m
k_S	Curve fitting	348x10^6 N/m
k_B	Data sheet	180x10^3 N/m
c_{MS}	Curve fitting	820 Ns/m
c_{AS}	Data sheet	230 Ns/m
c_S	Curve fitting	3125 Ns/m
c_B	Data sheet	607 Ns/m

The parameters of the model are summarised in Table 5.1. The damping values are the equivalent viscous damping coefficients. They incorporate viscous damping of the lubricant, material damping, etc. The value of the housing mass m_H is easily measured. Also, the manufacturers of the bushings and air springs provide values to derive k_B, k_{AS}, c_B and c_{AS}. The remaining parameters to determine are the mounting system stiffness k_{MS} and damping c_{MS}, the spindle stiffness k_S and damping c_S and the masses m_S and m_F. They are derived simultaneously with the test bearing stiffness k_{TB} and damping c_{TB}, by curve fitting the modelled FRFs to the measured FRFs. The FRFs of both the housing and spindle acceleration w.r.t. the shaker force are used.

Fig. 5.4 compares the measured (black lines) and calculated (grey lines) FRFs of both the housing and spindle acceleration. During this measurement, a 400 N radial load is applied on the test bearing. The bearing is stationary which allows measuring the spindle acceleration. Below 300 Hz, the measured FRFs are influenced by the axial translational and the three rotational modes of the bearing, which are not modelled. Above 600 Hz, the flexible modes of the surrounding structure appear. However, between 300 and 600 Hz, the correspondence between the model and the measurements is excellent.

After curve fitting the modelled and measured FRFs, the combined stiffness k_{TB+MS} and damping c_{TB+MS} are identified. k_{TB+MS} is the stiffness of both k_{TB} and k_{MS} in series. c_{TB+MS} is the damping of both c_{TB} and c_{MS} in series. The bending stiffness k_S is considered constant for different test bearing loads and speeds, as explained in Sect. 3.3.2. The masses m_S and m_F are the equivalent masses of the spindle and the frame, concentrated at the location of

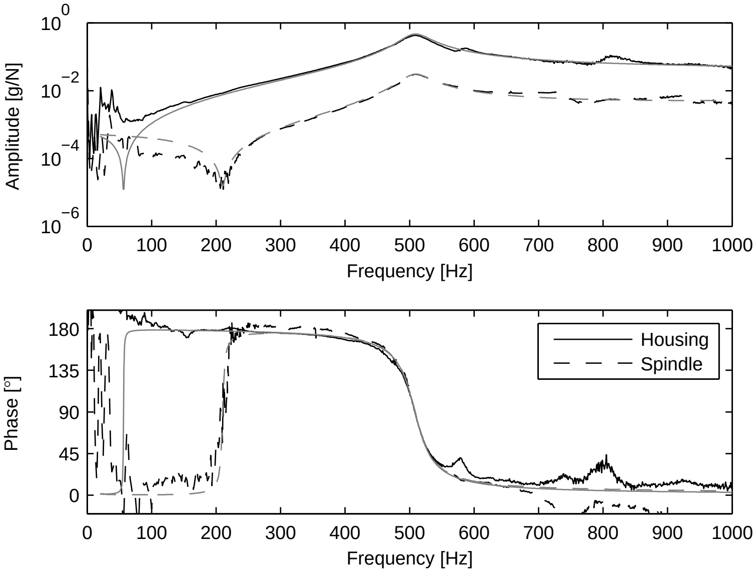

Figure 5.4: Comparison between the measured (black lines) and calculated (grey lines) FRFs. Both the FRF of the housing acceleration (solid lines) and spindle acceleration (dashed lines) are plotted.

the test bearing. The simulated system has three natural frequencies:

- 4.7 Hz: the motion of m_F on the bushing stiffness k_B.
- 512 Hz: the motion of m_H on the stiffness k_{TB+MS}.
- 1908 Hz: the first bending mode of the spindle shaft exciting the bearing.

Finally, the test bearing stiffness k_{TB} and damping c_{TB} are derived from the combined stiffness k_{TB+MS} and damping c_{TB+MS}. Only the values of the stiffness k_{MS} and damping c_{MS} of the modular mounting system have to be determined. Sect. 3.2.2 introduced the modular mounting system of the test bearing, which allows testing different types and sizes of bearings. k_{MS} and c_{MS} comprise the stiffness and damping of the bearing housing, the intermediate sleeve, the auxiliary shaft and the collet chuck. The bolted connection between the housing and sleeve and the chuck connection between the auxiliary shaft and spindle shaft are included as well. k_{MS} and c_{MS} are experimentally measured using a solid bearing consisting of a steel disk with the same dimensions as the test bearing. The disk is pressed into the sleeve and onto the shaft, forming a stiff connection between the sleeve and shaft. Since the stiffness of the steel disk is at least a factor 10 higher than k_{MS}, k_{TB+MS} approximates k_{MS}. Therefore, k_{MS} is identified using a similar procedure as applied to determine the test bearing stiffness, now with the steel disk mounted in the test rig and neglecting k_{TB} in the model. The damping of the mounting system c_{MS} is obtained from an estimated damping ratio of 2.5% for a bolted metal structure [1].

The current study investigates the bearing stiffness k_{TB} and damping c_{TB} for different operational conditions of the bearing. Using the parameters of Table 5.1, the identification of the bearing stiffness and damping only requires fitting the calculated and measured FRF of the bearing housing acceleration. The least squares curve fitting is performed in the vicinity of the rigid body mode, at which the bearing housing translates in the direction of the radial load. When changing the operational conditions of the bearing, the resonance frequency and damping ratio of this mode are mostly affected. The resonance frequency varies between 485 and 588 Hz, as a function of the operational conditions (Sect. 5.1.2). The model is developed for identification of the bearing dynamics in the range from 25 to 500 Hz. At high levels of the bearing load, the resonance frequency exceeds this range. Sect. 5.2.1 shows that the damping identification is hampered by a structural resonance at high loads.

5.1.4 Sensitivity analysis of the identification

The parameters of the analytical model cannot be exactly determined. This section discusses the effect of an error in an estimated parameter on the identification of k_{TB} and c_{TB}. The sensitivity of the identification, to deviations of the model parameters, is analysed. First, the true value of k_{TB} is set at 50x10^6 N/m and the true value of c_{TB} is set at 1000 Ns/m. In this way, the true FRFs are derived. Then, a deviation of 10% is added to a single parameter. Both k_{TB} and c_{TB} are determined from the true FRFs, using this modified model. Finally, the relative error between the true and estimated value of both k_{TB} and c_{TB} is derived. Table 5.2 summarises the results, after modifying each of the model parameters separately.

Table 2 shows:

- The error on the estimation of the stiffness k_{TB}.

  Table 2 emphasises the importance of an accurate determination of m_H, and - to a lesser extent - k_{MS} and k_S. The accurate measurement of the housing mass m_H is easily accomplished. As explained in Sect. 5.1.3, the stiffness of the mounting system k_{MS} and the spindle stiffness k_S are

Table 5.2: The error on the estimation of k_{TB} and c_{TB} after adding 10% to one of the model parameters.

Modified parameter	$\vert$Error on $k_{TB}\vert$ [%]	$\vert$Error on $c_{TB}\vert$ [%]
m_H	17.1	40.2
m_S	0.1	0.4
m_F	0.2	0.5
k_{MS}	3.8	< 0.1
k_S	1.5	1.9
k_B	< 0.1	< 0.1
k_{AS}	0.3	< 0.1
c_{MS}	< 0.1	9.9
c_S	< 0.1	1.8
c_B	< 0.1	< 0.1
c_{AS}	< 0.1	7.1

experimentally determined by curve fitting of the analytical model on measured FRFs. Following the datasheet of the air springs, the stiffness of the air springs k_{AS} varies depending on the applied air pressure. In the model, a mean value of its stiffness is used. Variations of up to 30% of the air spring stiffness are possible by changing the test bearing load. The sensitivity analysis proves that these changes do not significantly affect the identified k_{TB}.

- The error on the estimation of the damping c_{TB}.

  The damping identification is more sensitive to errors of the model. In most cases, an error on the estimation of a parameter has a larger effect on the identification of c_{TB} than k_{TB}. The maximum error is made when m_H, c_{AS} or c_{MS} are poorly estimated. The damping of the air springs c_{AS} is related to the air pressure, but this relation is unknown. For the estimation of c_{MS}, only a typical damping ratio is available. The modular mounting system, which allows testing different types and sizes of bearings, introduces an additional flexibility with unknown damping characteristics. To accurately identify damping characteristics of rolling element bearings, the test rigs presented by Mitsuya [75] and Dietl [19] are better suited. Mitsuya analyses a bearing assembly, in which the inner ring and shaft are unified. Also, the outer ring and housing are unified. The structure enables preloading without the need for any solid contact, using an externally pressurised air bearing. Uncertainties caused by the bearing assembly and preloading are strongly reduced. Dietl measures

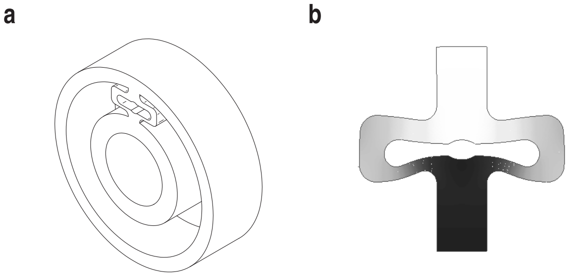

Figure 5.5: Design (**a**) and deformation (**b**) of the dummy bearing, used to validate the identification of the bearing stiffness.

the damping characteristics of a regular bearing. However, the supporting structure is made as stiff as possible. In this way, the bearing is the major source of compliance in the system and thus the major source of damping. The test rig presented in this paper is less suited for absolute determination of the bearing damping. Comparing the identified damping at different operational speeds and temperatures does provide valuable information on the damping characteristics of the test bearing, as shown in Sect. 5.3 and 5.4.

5.1.5 Validation of the stiffness identification

To validate the stiffness estimation, a dummy bearing with a known stiffness is mounted in the test rig. The design of the dummy bearing is shown in Fig. 5.5**a**. It consists of an inner ring, outer ring and a flexible structure in between. The intermediate structure contains four leaf springs, resulting in a radial stiffness comparable to a normal test bearing stiffness. The dummy bearing is manufactured to a precision on its dimensions of 0.02 mm. The stiffness is mainly determined by the thickness of the leaf springs and accurately derived using the FE model of Fig. 5.5**b**. The model uses a 2D geometry of the leaf springs. Assuming the nominal values of the geometry and a Young's modulus of 205x10^9 Pa, a calculated stiffness of 32.63x10^6 N/m is obtained.

The stiffness of the dummy bearing is experimentally identified using the same technique as explained in Sect. 5.1.3. A radial load of 400 N is applied on the structure. The identified stiffness equals 31.92x10^6 N/m. In comparison to the model, the stiffness deviates from its calculated value by 2.2%. This deviation can be caused by both an error in the calculated and measured stiffness.

The Young's modulus and the dimensions assumed in the model can slightly deviate from their real values and an error in the experimental identification can be made. However, it is concluded that the stiffness is identified sufficiently accurately.

5.2 Stiffness and damping: influence of the load

This section discusses the influence of the radial and axial static load on the bearing stiffness and damping. As explained in the previous section, the identification is based on the dynamic bearing response. The bearing stiffness is also derived from the static deformation of the bearing. The results of both methods are compared.

5.2.1 Identification based on the dynamic bearing response

Variation of the radial and axial static load shows the influence of the load on the bearing dynamics. For measurements at different levels of the axial static load, the axial air springs are added to the set-up of Fig. 5.2. Identification of the bearing stiffness and damping is done using the model of Sect. 5.1.3. The model parameters of Table 5.1 are derived based on the dynamic bearing response under a pure radial static load of 400 N. Applying the model at different load levels is only valid when the model parameters are independent of the load. The air springs exhibit strong nonlinear behaviour since their stiffness and damping depend on the applied air pressure. However, the sensitivity analysis of Sect. 5.1.4 shows a negligible influence of the air spring stiffness k_{AS} on the test bearing stiffness k_{TB}. Also, the axial air springs do not influence the radial stiffness k_{AS}, due to their negligible lateral stiffness. A change of the air spring damping c_{AS} does influence the estimation of the test bearing damping c_{TB}. The effect of the axial air springs on the damping c_{AS} is unknown. At load levels different from the load used during identification of the model parameters, the identified damping should be handled with care.

The FRF of the housing acceleration is measured in the frequency range from 450 to 600 Hz, in steps of 1 Hz. This allows accurate identification of the bearing stiffness and damping. The measured FRF is shown for three levels of the radial static load in Fig. 5.6. A clear shift of the resonance frequency of the radial rigid body mode is observed.

Fig. 5.7**a** and 5.7**c** present the identified bearing stiffness and damping for different levels of the radial load between 0 and 1600 N. The rotational speed of

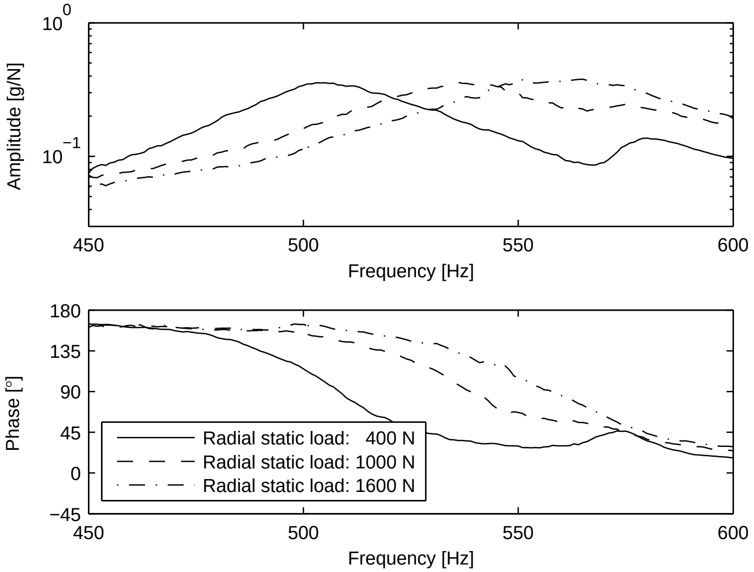

Figure 5.6: FRF of the housing acceleration for three different levels of the radial static load.

the bearing equals 1000 r/min. To avoid an influence of a varying temperature, the tests are carried out in quick succession. The stiffness increases as the radial load increases. More rolling elements transfer the load through the bearing and the contact surface between the rolling elements and the rings increases. The identified bearing damping shows an increasing trend. Similar measurements of Dietl [19] and numerical analyses of Sopanen [102] confirm this trend. A varying damping of the air springs at different load levels and a structural resonance around 580 Hz (Fig. 5.6) complicate the identification.

Usually, ball bearings are mounted with an externally applied axial load to ensure proper loading of the rolling elements. The applied load has a significant effect on the contact stiffnesses in the bearing [118]. While a 400 N radial load is applied, the stiffness is identified for different values of the axial load. Fig. 5.7**b** shows an increased radial stiffness k_{TB} due to an axial static load. The identified bearing damping c_{TB} shows unrealistic values after the axial air spring are mounted. These values are not reported.

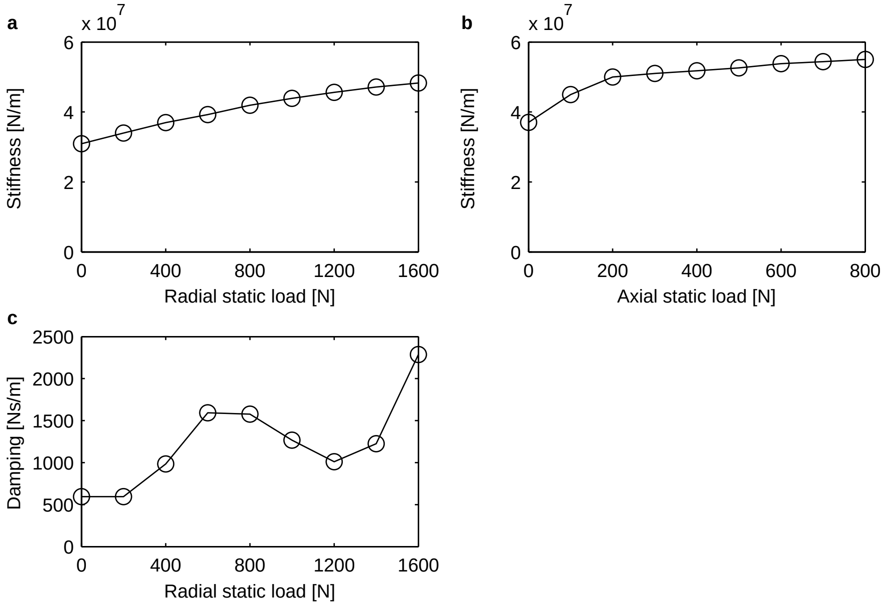

Figure 5.7: Identified stiffness (**a**) and damping (**c**) w.r.t. the radial load (no axial load applied). Identified stiffness (**b**) w.r.t. the axial load (400 N radial load applied).

5.2.2 Identification based on the static bearing deformation

The radial bearing stiffness k_{TB} can also be derived from the static deformation of the bearing, measured by the radial capacitive proximity probe. The radial load is increased by 100 N every 60 s while the radial bearing displacement is measured. Fig. 5.8 shows the displacement. The radial load is increased from 400 to 800 N. A constant axial load of 400 N is applied and the bearing rotates at 1000 r/min. Due to the motion of the rotating bearing, the radial displacement fluctuates strongly around its mean value at each load level. This bearing motion is discussed in Sect. 4.3. The mean displacement at each load level (black line) is obtained using a moving average filter of 10 s.

The capacitive probes are mounted on the housing and pointed to the shaft. In between, the test bearing and the mounting system comprise the flexible system (Fig. 3.12). The difference between the measured mean displacement at two successive load levels reveals the flexibility of the system at these load levels. The radial bearing stiffness k_{TB} is derived from this flexibility and the known stiffness of the mounting system k_{MS} (Sect. 5.1.3). Fig. 5.9 shows the identified

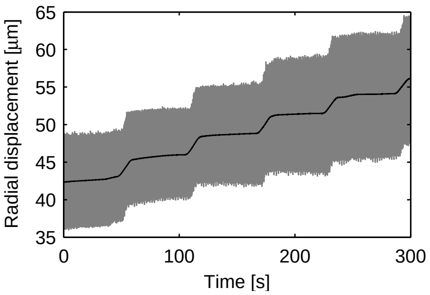

Figure 5.8: Radial displacement of the bearing during a run-up of the radial load (grey line). The load is increased by 100 N every 60 s. The mean displacement is calculated using a moving average filter of 10 s (black line).

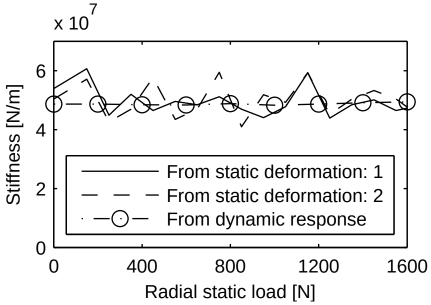

Figure 5.9: Calculated radial bearing stiffness based on the static deformation of the bearing. The result of two similar tests is compared to the identified stiffness based on the dynamic bearing response. An axial load of 400 N is simultaneously applied in all tests.

radial bearing stiffness based on two tests in the same conditions. Due to the axial static load of 400 N, the radial stiffness is nearly independent of the radial load.

To evaluate the measurement results, the stiffness is identified from the dynamic response (Sect. 5.1.3) under the same static load. Fig. 5.9 shows a similar trend of the identified bearing stiffness for both methods. However, a high scatter on the stiffness derived from the proximity probes is observed. Electro-pneumatic regulators accurately control the static bearing load. During calibration of the air spring load, deviations of the load up to 0.5% are noted when repeatably applying a certain pressure (Sect. 3.2.3). These small absolute variations however introduce a large relative error when two load levels are compared. An equal raise of the air pressure yields variations of the load increase up to 20%. As the stiffness is determined based on the difference between the displacement at two load levels, the results are affected by these variations. When identifying the bearing stiffness based on the dynamic bearing response, only the absolute load level should be set accurately. This method is preferred and used in the remainder of the chapter.

5.3 Stiffness and damping: influence of the temperature

This section discusses the influence of the temperature on the formation of the lubricant film and its effect on the identified bearing stiffness and damping. Starting at room temperature, the rotational speed of the bearing is brought to 1000 r/min. The radial bearing load is 400 N. The temperature, electrical resistance, stiffness and damping are measured as a function of time. Fig. 5.10 shows the results during the first 40 min of the warm-up.

As the bearing temperature increases, the lubricant film thickness decreases and the internal bearing clearance increases. The bearing stiffness consequently decreases. During the first 40 min of the warm-up, the identified stiffness is reduced by 10%. The stiffness reaches a stable value at a point in time comparable to that of the inner ring temperature. Similar observations were made by Stone [107], during a warm-up of a deep groove ball bearing. While the electrical resistance follows variations of the lubricant's temperature, the stiffness reacts to temperature variations of both the lubricant and the material surrounding the rolling contacts. An additional effect, linked to the temperature of the surrounding material, seems to influence the stiffness. It can be noted that expansion of the bearing material also affects the bearing stiffness. As the inner ring reaches a higher temperature than the outer ring, the internal bearing clearance decreases and the bearing stiffness increases. However, this effect is overshadowed by the first two effects.

As the lubricant film thickness decreases, the bearing damping also decreases. During the first 40 min of the warm-up, the damping is reduced by 37%. The behaviour of the damping as a function of time is very similar to the behaviour of the resistance. Both are linked to the lubricant's temperature in the bearing contacts. While the viscosity of the lubricant is considered to decrease strongly during the bearing warm-up, the measured damping variation is limited. This observation is supported by findings of Dietl [19]. Dietl analysed lubricants with different viscosity values, and their influence on the bearing damping.

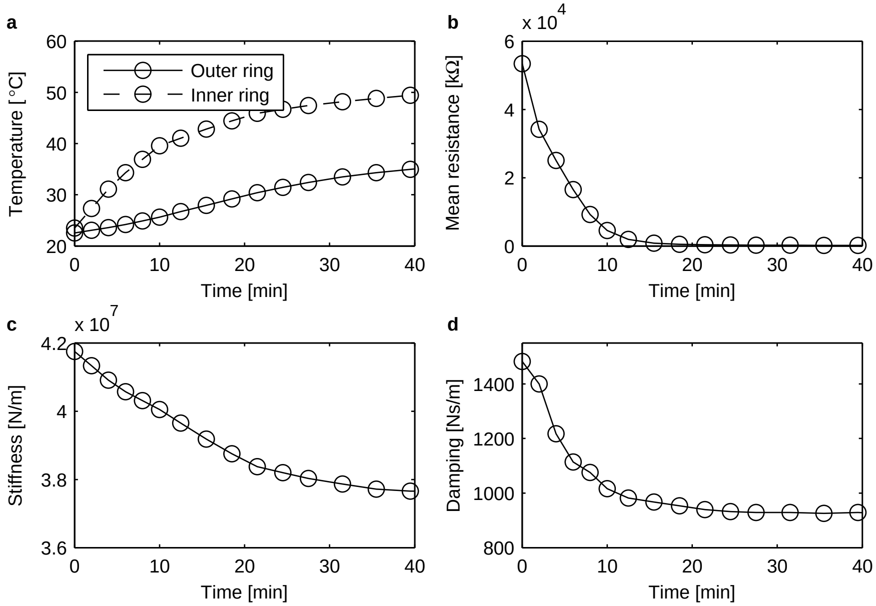

Figure 5.10: Temperature (**a**), electrical resistance (**b**), identified stiffness (**c**) and identified damping (**d**) during a warm-up.

He showed that the bearing damping is only increased by 10% after using a lubricant having a five times higher viscosity.

5.4 Stiffness and damping: influence of the speed

In this section, the bearing stiffness and damping properties are analysed for different rotational speeds of the bearing. As the bearing temperature has a significant influence on the results, both the isothermal and steady-state temperature condition are analysed. First, a stationary bearing is investigated, considering the influence of the shaft angular position on the bearing dynamic properties.

5.4.1 Shaft angular position

Recalling Sect. 4.2.2, the internal load distribution changes as the angular position of the rolling element set changes. Consequently, the Hertzian contact

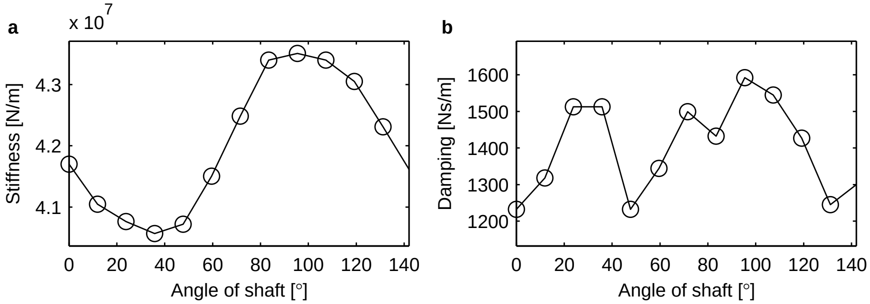

Figure 5.11: Identified stiffness (**a**) and damping (**b**) of the stationary test bearing for different angles of the shaft.

stiffness of the different contacts changes. Bending of the outer ring, due to the loose fit between the outer ring and the housing, also depends on the position of the rolling element set. The bearing stiffness, determined by the Hertzian contact stiffness of the different contacts and bending of the outer ring, is different for different angular positions. As a result, the bearing stiffness fluctuates at the rate at which a rolling element passes the loaded zone. This effect is called variable elastic compliance. The frequency at which a rolling element passes the loaded zone is the ball pass frequency (BPF).

The stiffness and damping of the test bearing are identified for different angular positions of the shaft. Fig. 5.11 shows the result of a series of measurements at room temperature. A radial load of 400 N is acting on the bearing. For the mounted deep groove ball bearing 6302, the BPF equals 2.53 times the rotational frequency of the shaft. The period at which a rolling element passes the loaded zone equals 142.3 ° of shaft rotation. A variation in stiffness of 7.3% between the two positions of Fig. 4.3 is observed. The damping shows significant variations as well, however lacking a clear trend for different shaft positions.

5.4.2 Rotation at a constant bearing temperature

In order to analyse the influence of the rotational speed on the stiffness and damping of the bearing, tests at different speeds from 100 to 1500 r/min are performed. A radial load of 400 N is acting on the bearing. The measurements start after the bearing reached its stable temperature at 1000 r/min. To avoid an influence of a varying temperature, the tests are carried out in quick succession. The identified bearing stiffness and damping are given in respectively Fig. 5.12**c** and 5.12**d**. The formation of the lubricant film in the contacts between rolling

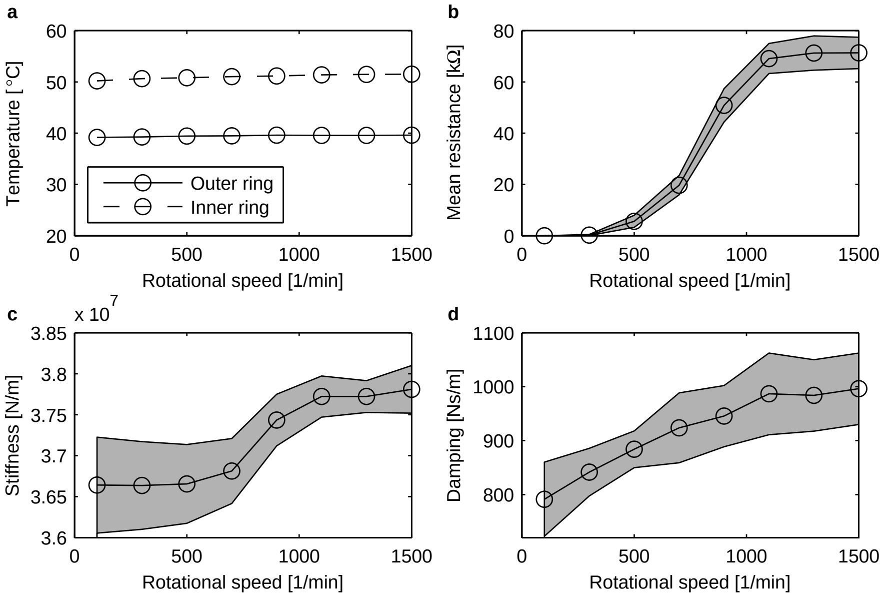

Figure 5.12: Temperature (**a**), electrical resistance (**b**), identified stiffness (**c**) and identified damping (**d**) during a run-up of the speed. The tests are performed in isothermal conditions. The grey areas indicate the scatter on the data, obtained after repeating each test five times.

elements and raceways is simultaneously measured by means of the bearing's electrical resistance (Fig. 5.12**b**). The grey areas visualise the scatter on the identified parameters, resulting from five measurements starting at the same stable temperature.

To accurately identify the bearing stiffness and damping, the FRF of the housing acceleration is measured in the frequency range from 450 to 550 Hz, in steps of 1 Hz. 150 periods of each exciting sine are applied on the structure. As discussed in Sect. 5.4.1, the stiffness of a stationary bearing depends on the position of the rolling element set. During rotation, the mean stiffness is identified. Applying stepped sine excitation, sufficient periods of each exciting sine are measured. At the lowest bearing speed (100 r/min), the period at which a rolling element passes the loaded zone equals 0.24 s. When the frequency of the exciting sine equals 500 Hz, at least 119 periods of the sine are measured in order to excite the bearing through a full period of a rolling element passing the loaded zone. A total measurement time of 30 s is required at each rotational speed. Fig. 5.12**a** shows that the measurements are performed in isothermal conditions.

In case of a non-rotating bearing, the EHL contacts behave as dry contacts. When the bearing starts to rotate, a lubricant film builds up between the rolling elements and the raceways [121]. Up to rotational speeds of 200 r/min, the electrical resistance of the bearing equals zero. The lubricant is squeezed out of the contacts, leaving only pure metal-to-metal contacts. At speeds above 200 r/min, a lubricant film in the contacts starts to form and the resistance increases. At 1200 r/min, the formation of the film is complete.

Despite scatter of up to 3%, an increasing trend of the identified stiffness is found. A mean increase of 3.2% is observed. The trend is similar to the increase of the electrical resistance through the bearing. In the literature, no experimental measurements showing this relation between the film formation and the increased bearing stiffness are reported. The effect is numerically investigated by Wijnant and Wensing. Wijnant [120] simulates a single lubricated contact and observes an increased contact stiffness in comparison to a dry contact. Wensing models a full bearing. Owing to the formation of a lubricant film, the effective internal bearing clearance is reduced. The elastohydrodynamic film can even create negative clearance or preload [94, 118]. In this way, the formation of a lubricant film leads to an increased bearing stiffness as well. It can be noted that another factor, influencing the bearing stiffness as a function of its rotational speed, is the centrifugal force acting on the rolling elements. The centrifugal force mainly influences the effective contact angle of the bearing. In this way, the force affects the bearing stiffness. In case of a deep groove ball bearing, loaded only in its radial direction and rotating at speeds up to 1500 r/min, the centrifugal force cannot affect the stiffness measurably.

Despite a high scatter on the results between similar tests, the identified damping clearly tends to increase with increasing rotational speed. A mean increase of 24% in the considered speed range is observed. In the literature, no measurements of the bearing damping during formation of the lubricant film are reported. Refs. [19, 75, 93] do compare damping measurements of lubricated and non-lubricated rolling element bearings. A higher damping of the lubricated bearings is observed in each publication. As shown in Fig. 5.12**b**, the bearing can be considered being dry for speeds up to 200 r/min. At 1200 r/min, the bearing can be considered being fully lubricated. In this way, the observations of these publications correspond to the current results. Other publications related to this work are Refs. [107, 120]. Stone [107] reports on measurements of damping of a deep groove ball bearing during a run-up from 0 r/min. No significant variation of the damping is observed. Wijnant [120] numerically analyses the influence of the lubricant film on the bearing damping, in the speed range of a fully developed lubricant film.

A scatter on the identified damping of up to 20% is observed. Kraus [65] reports similar deviations on the measured damping of two spindle bearings.

Mitsuya [75] explains that the bearing has a complex structure by itself. Slight differences in the contact conditions, the differential or spin slips, the location of the cage, etc. produce large scatter in the damping identification.

Finally, the influence of the radial bearing load on the identified stiffness and damping during a run-up of the speed is analysed. The measurements of the current section are repeated at different levels of the radial load between 200 and 800 N. In Sect. 4.4.2, the influence of the load on the lubricant film thickness is analysed. Sect. 5.2 discusses the identified bearing stiffness and damping w.r.t. the load. The variation of the electrical resistance and identified stiffness and damping, due to the formation of a lubricant film, is compared for different load levels. The relative changes of the electrical resistance and identified stiffness and damping are similar to the changes of Fig. 5.12 at 400 N. An increase of the bearing stiffness between 2.5% and 3.4% and an increase of the damping between 16% and 47% are identified. An effect of a reduced film thickness at higher load levels cannot be observed. The variations between the different load levels are smaller than the actual scatter on the results between similar tests.

5.4.3 Rotation at a stabilised bearing temperature

In practice, a higher rotational speed of the bearing implies a higher operational temperature of the different bearing components. Sect. 5.3 discussed the effect of the temperature on the bearing dynamics at a constant speed. Sect. 5.4.2 discussed the effect of the speed on the bearing dynamics in isothermal conditions. For this section, measurements are performed after the bearing's temperature has reached its stable value at each different speed. Consequently, the combined effect of both rotation and temperature is analysed. The measurements are repeated five times to assess the scatter on the identified values. Fig. 5.13 shows the results. The radial bearing load is 400 N.

The measurements are first compared to those in isothermal conditions of Fig. 5.12. The measurements of Fig. 5.12 are performed starting from a stable temperature at 1000 r/min and a 400 N radial load. During the measurements of this section, the temperature is lower at speeds below 1000 r/min. When comparing the measurements of Fig. 5.12 and 5.13 at the same speeds, this lower temperature implies:

- The lubricant's viscosity is higher and the lubricant film is thicker.
- The electrical resistance of the bearing is higher. Also, a lubricant film is already formed at a speed of 100 r/min.

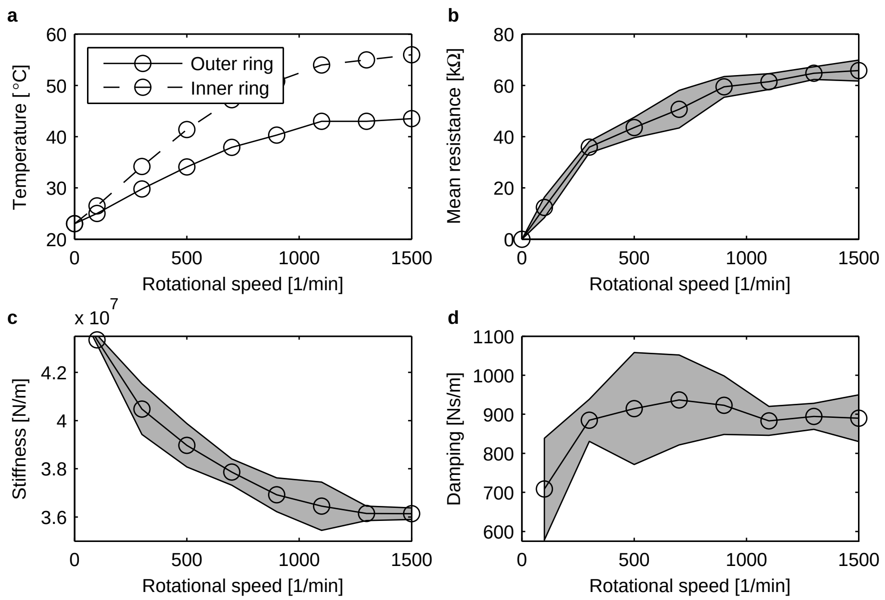

Figure 5.13: Temperature (**a**), electrical resistance (**b**), identified stiffness (**c**) and identified damping (**d**) during a run up of the speed. Each test is performed after stabilisation of the temperature. The grey areas indicate the scatter on the data, obtained after repeating each test five times.

- The identified stiffness is higher. Sect. 5.3 indicated a higher bearing stiffness at lower temperatures.
- The identified damping is higher. Sect. 5.3 indicated a higher bearing damping at lower temperatures. Only the measurement at 100 r/min does not follow this reasoning.

At speeds above 1000 r/min, the operational temperature is higher in comparison to the measurements at isothermal conditions. This implies a lower electrical resistance, identified stiffness and identified damping. This is confirmed by the measurements and seen when comparing Fig. 5.12 and 5.13.

In isothermal conditions, the resistance, stiffness and damping increase as the speed increases. At a constant speed, the resistance, stiffness and damping reduce as the temperature increases. When combining both effects, the resistance increases as the speed and temperature increase. The resistance evolves in the same way as the measured temperatures as a function of speed. After all, the temperature of the lubricant and both the inner and outer ring reached their stable values. The stiffness decreases as the speed and temperature increase. Whether the lubricant film leads to an increase or decrease of the bearing stiffness is determined by the temperature conditions. The damping remains roughly constant at speeds above 100 r/min.

5.5 Conclusion

The bearing housing is excited using an electrodynamic shaker while its response is measured with accelerometers. Stepped sine excitation of the structure is preferred over broadband noise excitation. Broadband noise excitation introduces harmonic distortions in the measured response due to nonlinear behaviour of the test bearing. Modal analysis of the housing reveals the resonance frequencies and damping ratios of the rigid body modes of the housing mass. The housing mass is supported by the test bearing and flexible air springs. Changing the bearing load, speed or temperature affects the stiffness and damping characteristics of the bearing. The resonance frequencies and damping ratios of the rigid body modes allow identifying the dynamic characteristics of the test bearing. A spring-mass-damper model of the test rig is fitted to the measured response to obtain the test bearing stiffness and damping. The stiffness identification is determined by model parameters which are well-known. It is validated using a dummy bearing with a known stiffness. The damping identification is more sensitive to errors of the model. The test rig is not suited for absolute determination of the bearing damping. Comparing the identified damping at different operational speeds and temperatures does provide valuable information on the damping characteristics of the test bearing.

The influence of the radial and axial load on the bearing stiffness is analysed. Two different methods are compared. The first method is based on the dynamic bearing response and the spring-mass-damper model of the test rig. The second method uses the static bearing deformation as measured by the radial proximity probe. In the second method, the stiffness is derived from a change in deformation between two load levels. A small error on the applied bearing load introduces a significant error in the stiffness calculation. In the first method, only the absolute load level should be precisely set. The first method is preferred to accurately identify the bearing stiffness.

Variation of the bearing temperature and speed reveals the influence of the lubricant film. During a warm-up of the bearing, the lubricant film thickness strongly decreases and the internal bearing clearance increases. The identified stiffness and damping consequently reduce. During a run-up of the speed, the electrical resistance through the bearing shows the formation of a lubricant film. In isothermal conditions, the stiffness and damping increase due to the formation of the lubricant film. In practice, a higher rotational speed of the bearing implies a higher operational temperature of the bearing components. The influence of the film formation is analysed for different speeds at a stable bearing temperature. A combined effect of both the temperature and speed is observed. Whether the lubricant film leads to an increase or decrease of the bearing stiffness is determined by the temperature conditions. In the literature, no experimental measurements showing these relations between the film formation and the dynamic properties are reported. The results help to evaluate the significance of modelling the lubricant film when numerically analysing the vibrations of a bearing system.

Chapter 6

Dynamic loading of the test bearing

Accurate prediction of the lifetime of rolling element bearings is a crucial step towards a reliable design of many rotating machines. Lifetime calculations of bearings are based on the ISO 281 standard. For bearings subjected to highly varying loads, recent research emphasises a strong reduction of the actual bearing lifetime w.r.t. the calculated bearing lifetime. The current study analyses the effect of external dynamic loads on the lifetime of the test bearing. Two separate investigations are conducted. The behaviour of the lubricant film during strong external excitation and wear of the raceway surfaces due to dynamic loads are analysed.

Increased wear of the raceway surfaces is expected when the lubricant film breaks down during external excitation. The behaviour of the lubricant film is identified using the electrical resistance through the bearing and the measured bearing motion. When introducing a dynamic load, a clear response of the lubricant film is measured. This response is analysed for different types of excitation and different operational conditions of the bearing. Increased metallic contact during external excitation of the bearing is investigated.

When introducing an axial dynamic load on the bearing, a significant increase of the bearing temperature is measured. The additional frictional power loss is analysed for different excitation amplitudes, static load levels and rotational speeds. The heat generation mechanism is identified. The results reveal the operational conditions of the bearing at which surface wear due to dynamic loads is expected to be maximal.

Finally, accelerated lifetime tests under high dynamic load are performed. In separate tests, strong radial, axial and combined radial and axial vibrations are introduced on the test bearing. The operational conditions of the bearing are selected such that surface wear is expected to be maximal. The raceway surfaces are investigated using a scanning electron microscope and the initial effect of surface wear is identified.

The response of the lubricant film to dynamic excitations is discussed in Sect. 6.1. Sect. 6.2 describes the frictional power loss due to dynamic excitations. The accelerated lifetime tests are reviewed in Sect. 6.3.

6.1 Lubricant response under dynamic load

This section discusses the influence of external dynamic loads on the lubricant film response. Both the properties of the excitation (amplitude, frequency and direction) and the operational conditions of the bearing (static load, operational temperature and rotational speed) are varied while the lubricant film response is measured.

6.1.1 Analysis of lubricant response

In Sect. 4.3.2, the radial motion of the test bearing is analysed. The radial displacement is measured using a capacitive proximity probe while the bearing rotates at 600 r/min and a 1000 N radial load is applied. The resulting spectrum is given in Fig. 4.5. The response of the lubricant film, due to this bearing displacement, is analysed analogously. The electrical resistance is measured for 180 s to derive its spectrum (Fig. 6.1). This spectrum has a higher noise level than the spectrum of the bearing displacement. Nevertheless, a variation of the electrical resistance due to the bearing displacement can be seen. A variation at the rotational frequency of the shaft, the first five harmonics of the cage frequency and the first two harmonics of the BPF is observed.

A radial sine excitation, having an amplitude F_r equal to 35 N and an excitation frequency f_e equal to 320 Hz, is added to the bearing load. The bearing rotates at 1000 r/min while a 1000 N radial static load is applied. Fig. 6.2 shows the spectrum of the bearing electrical resistance. A response of $1.6\text{x}10^3$ Ω at the excitation frequency is observed, w.r.t. a mean electrical resistance of approximately $40\text{x}10^3$ Ω.

The measured peak at the frequency of excitation (and its harmonics) reveals the response of the lubricant film due to an external excitation. The response

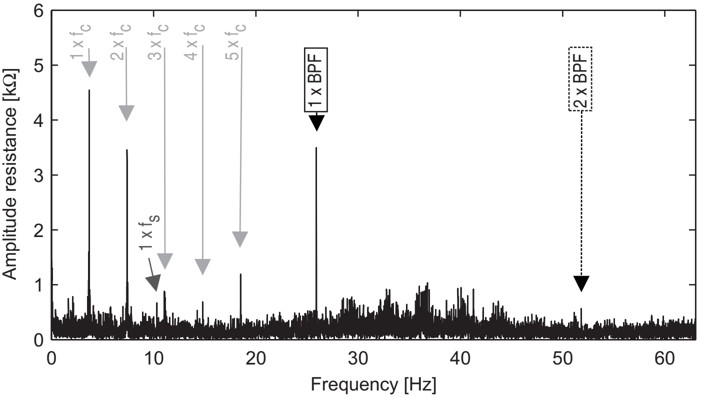

Figure 6.1: Spectrum of the bearing electrical resistance (static bearing load). Different components of the bearing motion are identified.

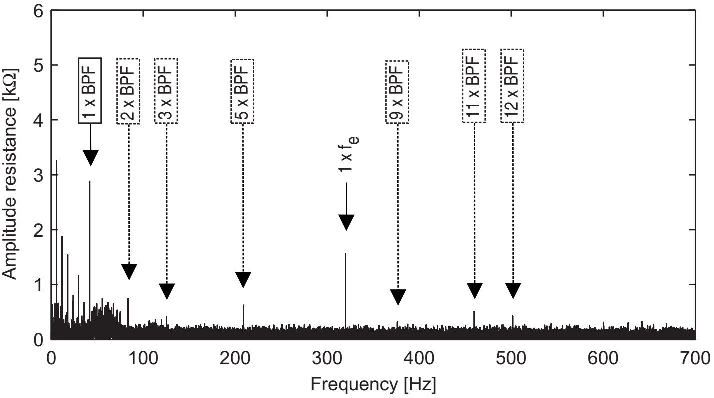

Figure 6.2: Spectrum of the bearing electrical resistance (static and dynamic bearing load). A clear response of the sine excitation at 320 Hz is observed.

is determined by both the properties of the excitation and the operational conditions of the bearing. The influence of both is analysed in the next sections. First, an upper limit of the excitation frequency is derived based on the error when neglecting the bearing capacitance.

6.1.2 Calculating the variation of the electrical resistance

Recalling Fig. 3.20, the different metal-lubricant-metal transitions in the bearing form a resistance R_{TB} and capacitance C_{TB} in parallel. The mean bearing resistance is measured based on the voltage drop over the bearing V_{out}. As a DC power supply is used, the bearing capacitance does not influence the results. When applying an external excitation, the bearing resistance varies at the frequency of excitation. The bearing capacitance can no longer be neglected when identifying this variation of the bearing resistance. The capacitance introduces additional conductive paths through the bearing influencing the measured voltage drop.

Identifying the bearing capacitance

The influence of the bearing capacitance on the calculated resistance is analysed separately. For this purpose, an alternating current (AC) supply powers the circuit of Fig. 3.20. The input voltage V_{in} is a pure sine with an amplitude of 5 V. The frequency of the sine is varied from 20 to 1020 Hz in steps of 50 Hz. The ratio between the measured output voltage V_{out} and the input voltage V_{in} is shown in Fig. 6.3. At 0 Hz, both voltages are in phase. When increasing the frequency of the input voltage, the conductance of the capacitive paths increases and the bearing impedance decreases. The voltage ratio thus decreases while the phase difference between the input and output voltage increases.

The analysis is repeated for different operational conditions of the bearing. A high radial load of 1600 N and a low rotational speed of 600 r/min imply a thin lubricant film and a large surface area of the contacts. The bearing resistance is small while the bearing capacitance is high. Consequently, the impedance of the test bearing is small. Following Eq. 3.1, so is the voltage ratio. The solid line of Fig. 6.3 represents this condition. When reducing the load and increasing the speed, the lubricant film thickness increases and the surface area decreases. Consequently, the impedance of the test bearing and the voltage ratio increase.

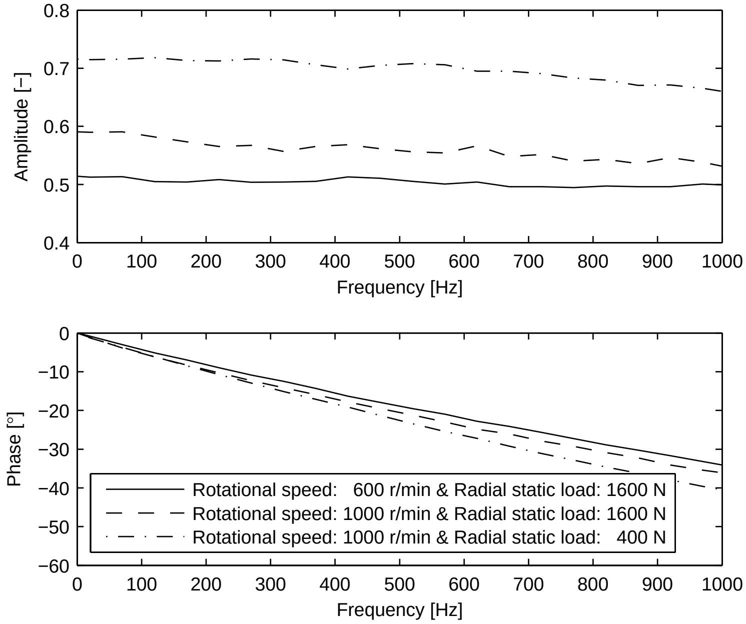

Figure 6.3: Ratio between the output voltage V_{out} and the input voltage V_{in} of the electrical circuit. The input voltage is a pure sine of which the frequency is varied.

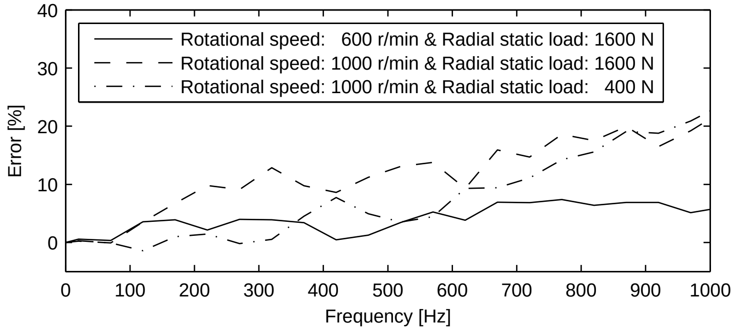

Figure 6.4: Error when neglecting the bearing capacitance during calculation of the bearing resistance.

Error when neglecting the bearing capacitance

The capacitance C_{TB} depends on the operational conditions of the bearing: the radial and axial load, the speed and the temperature. Identifying the capacitance is an elaborate task. This part investigates the error on the calculation of a varying resistance when neglecting the bearing capacitance.

To calculate the electrical resistance, the measured value of the ratio between the output voltage V_{out} and the input voltage V_{in} at the frequency of excitation is filled into Eq. 3.2. To calculate the resistance and take into account the bearing capacitance, the value of the ratio at 0 Hz should be used instead. At 0 Hz, the circuit is correctly described by this equation. The relative difference between the calculated resistance in both ways is shown in Fig. 6.4, representing the error when neglecting the capacitance.

In the remainder of this chapter, the response of the electrical resistance is analysed for frequencies up to 700 Hz. Up to 700 Hz, an error of less than 20% is observed and neglecting the bearing capacitance is accepted.

6.1.3 Lubricant response: influence of the amplitude

The influence of the external excitation on the lubricant film response depends on the amplitude and direction of the excitation. Both are analysed separately. In all tests, the bearing rotates at 1000 r/min while a 1000 N radial static load is applied. The bearing displacement at the excitation frequency is analysed as well. The radial displacement is obtained from the radial proximity probe, while the axial displacement is calculated as the mean displacement of both axial proximity probes. Recalling Sect. 3.3.3, the voltage drop over the bearing is dominated by the heaviest loaded rolling element. The contact surface area is maximal and the film thickness is minimal for this contact. The heaviest loaded rolling element also defines the lubricant's response to dynamic excitations.

Firstly, the amplitude of the radial excitation is increased while its frequency is fixed. The excitation frequency is set at 320 Hz. Fig. 6.5**a** and 6.5**c** show the relation between the amplitude of the radial load, the radial displacement and the electrical resistance. The response of the electrical resistance is proportional to the amplitude of the radial load, once the noise level is exceeded. The second and higher harmonics of both the displacement and electrical resistance are negligible.

During radial displacement of the outer ring w.r.t. the inner ring, the lubricant film thickness and surface area of each contact change. The electrical resistance responds to these variations according to Eq. 4.2 of Sect. 4.4.2. For small

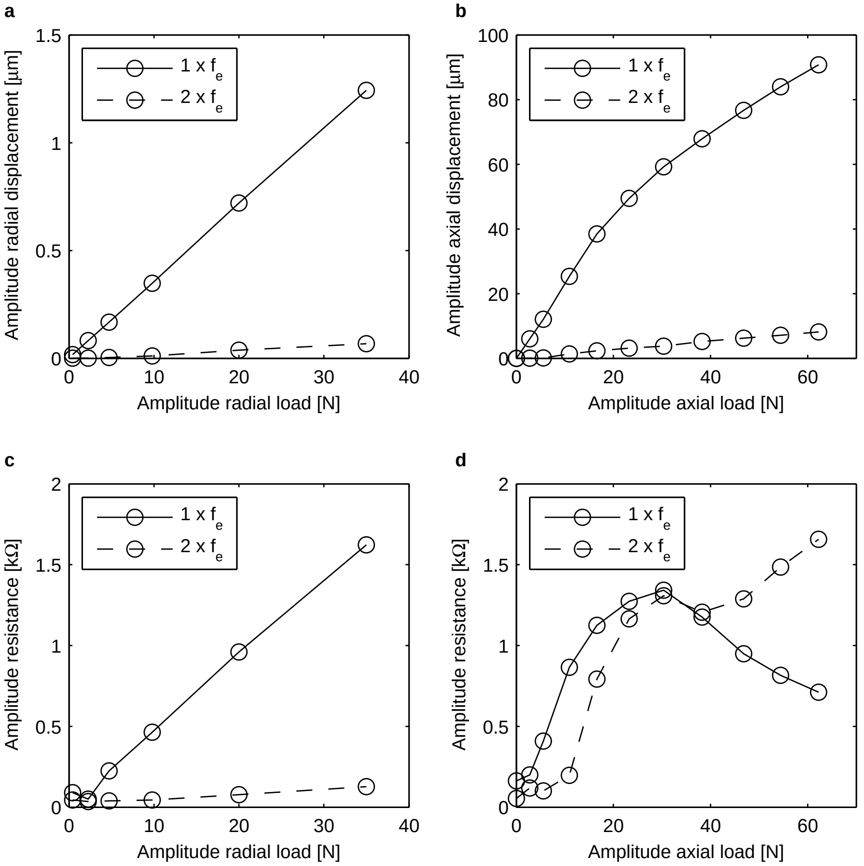

Figure 6.5: Amplitude of the radial displacement (**a**) and electrical resistance (**c**) w.r.t. the amplitude of the radial dynamic load. Amplitude of the axial displacement (**b**) and electrical resistance (**d**) w.r.t. the amplitude of the axial dynamic load.

variations of the radial load, a proportional relation between the bearing displacement and the variation of the electrical resistance is observed. Sect. 6.1.5 shows that the measured variations of the electrical resistance are similar to the variations when the radial static load is changed.

Secondly, the amplitude of the axial excitation is increased while its frequency is fixed. The excitation frequency is set at 210 Hz, corresponding to the frequency of the axial rigid body mode when a 1000 N radial load is applied (Sect. 5.1.2). A

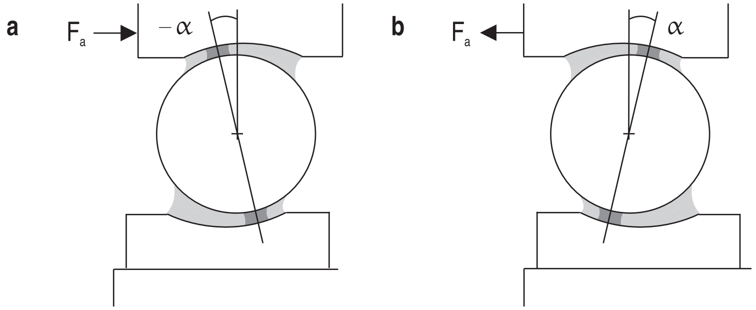

Figure 6.6: Formation of the EHL film (dark grey) for two axial positions of the outer ring (**a** and **b**).

strong excitation is therefore obtained when increasing the amplitude. Fig. 6.5**b** and 6.5**d** give the relation between the amplitude of the axial load, the axial displacement and the electrical resistance. Nonlinear relations are observed.

Under the condition of no load, the outer ring is free to float axially (Sect. 4.5.4). A 14 µm measured radial clearance during operation (Sect. 4.1.2) results in a 132 µm axial clearance. The amplitude of the axial motion equals 66 µm, being half of the axial clearance. The axial clearance is removed once a radial load is applied. Hertzian contacts form and the bearing obtains axial stiffness (Sect. 5.1.2). As the axial stiffness is much smaller than the radial stiffness, the displacement amplitudes in the axial direction are higher. As the axial stiffness increases at higher load levels, the response of the axial displacement deviates from a linear trend.

During axial displacement of the outer ring w.r.t. the inner ring, the lubricant film thickness and surface area of each contact change. The electrical resistance responds to these variations. Also, introducing an axial load leads to the formation of a contact angle α. The contact angle varies sinusoidally when applying the dynamic excitation. The dark grey areas in Fig. 6.6 show the locations where the pressure builds up and the EHL film is formed for two positions of the outer ring. Due to the nonlinear motion of the rolling elements and the variation of the EHL film location, the response of the lubricant film is strongly nonlinear at high load levels. Sect. 6.1.5 shows that the response of the lubricant film is linked to a variation of the lubricant film thickness.

The PCT value of Sect. 3.3.3 gives the time fraction of metallic contact. Fig. 6.7 shows the mean electrical resistance and PCT for the current measurements including a radial and axial excitation. The mean electrical resistance and PCT are dominated by random metallic contact as $\Lambda \approx 1$. A variation of the

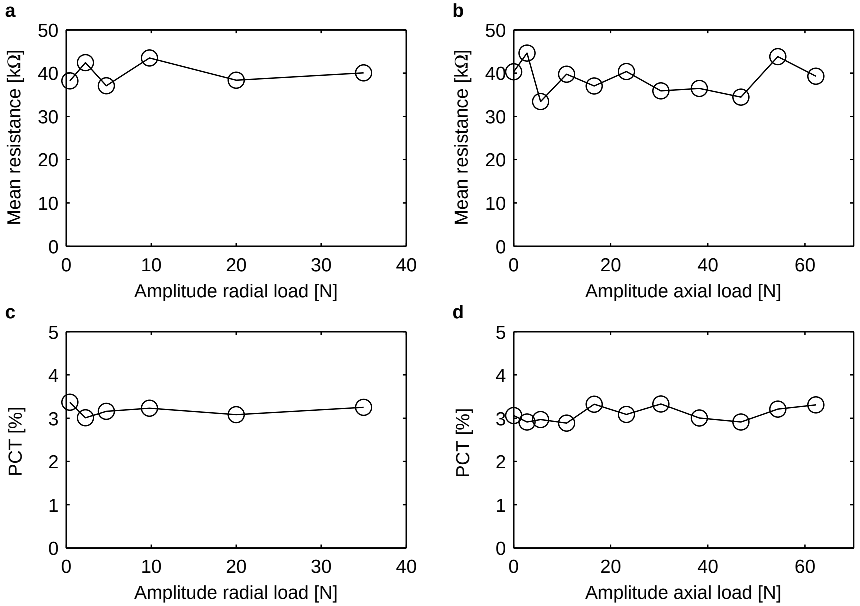

Figure 6.7: Mean resistance w.r.t. the amplitude of the dynamic load in the radial (**a**) and axial (**b**) direction. PCT w.r.t. the amplitude of the dynamic load in the radial (**c**) and axial (**d**) direction.

lubricant film thickness around its mean value due to the dynamic excitation does not affect these values. Breakdown of the lubricant film is not observed. The EHL film separates the rolling elements and raceways and follows variations of the radial and axial dynamic load.

6.1.4 Lubricant response: influence of the frequency

The results are not only affected by the amplitude of the excitation, but also the excitation frequency. To analyse this relation, the frequency of the sine excitation is varied from 20 to 670 Hz in steps of 50 Hz. Excitation at multiples of the mains frequency (50 Hz) is consequently avoided. The amplitude of the sine excitation is 35 N. The bearing rotates at 1000 r/min and a radial load of 1000 N is continuously applied.

Fig. 6.8**a** shows the response of the bearing displacement and electrical resistance when the excitation is applied in the radial direction. Both the first and second harmonic of the response are visualised. Analogously, Fig. 6.8**b** shows the

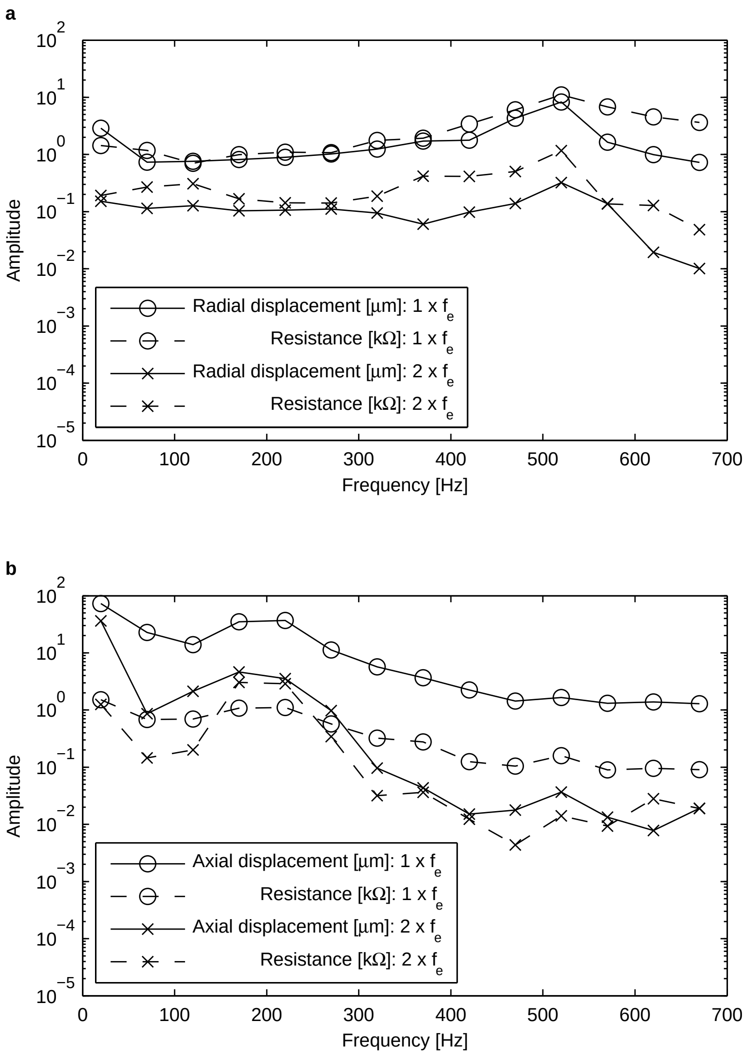

Figure 6.8: Response of the bearing displacement and electrical resistance w.r.t. a sine excitation at different frequencies. The excitation is applied in the radial (**a**) and axial (**b**) direction. Both the first and second harmonic of the response are visualised.

response for different excitations in the axial direction. The bearing displacement is determined by the dynamics of the bearing system, discussed in Sect. 5.1.2. When a radial load of 1000 N is applied, the radial translational rigid body mode of the bearing housing leads to an increased radial response around 540 Hz and the axial translational rigid body mode of the bearing housing leads to an increased axial response around 210 Hz.

The response of the electrical resistance generally follows the amplitude of the bearing displacement, analogous to the observations of Sect. 6.1.3. This holds for both for a radial and a small axial excitation and both the first and second harmonic of the response. When the excitation frequency approximates the frequency of the axial rigid body mode, the axial excitation results in a high axial displacement. The second and higher harmonics of the electrical resistance are more pronounced. This nonlinear behaviour during strong axial excitation is also discussed in Sect. 6.1.3.

In the next sections, the influence of the bearing operational conditions on the lubricant film response is analysed. The frequency of the radial dynamic load is set at 320 Hz. The frequency of the axial dynamic load corresponds to the frequency of the axial rigid body mode. Consequently, the first and second harmonic of the response are high (Fig. 6.8) and accurately measured (Sect. 6.1.2) in both directions. The amplitude of the dynamic load in the radial and axial direction is controlled and fixed to 35 N. At a speed of 1000 r/min and a radial static load of 1000 N, a radial displacement of 1.2 μm and an axial displacement of 61 μm at the excitation frequency are obtained. The effect of a strong excitation is thus analysed.

6.1.5 Lubricant response: influence of the load

The static load applied on the bearing influences both the dynamics of the system and the lubricant film behaviour. A combined effect is observed when analysing the response of the electrical resistance. When increasing the static load:

- The bearing stiffness and the resonance frequencies of the housing's rigid body modes increase (Sect. 5.2.1). The bearing displacement at the excitation frequency subsequently changes. The response of the electrical resistance follows these changes of bearing displacement.
- The contact pressure between the rolling elements and raceways increases. The lubricant's viscosity subsequently increases and a stronger lubricant film forms. In this context, the terms weak and strong lubricant film indicate whether the film does or does not easily allow thickness variations.

The effect of the structure's dynamics is discussed in Sect. 6.1.3 and 6.1.4. Generally, a proportional relation between the bearing displacement and the variation of the electrical resistance is observed. To separately analyse the effect of the lubricant's viscosity, the variation of the electrical resistance is divided by the bearing displacement. The electrical resistance per unit of displacement reveals the effect of a changing lubricant film behaviour while cancelling the effect of the structure's dynamics. During rotation of the bearing at 1000 r/min, the following load combinations are investigated:

1. The influence of the radial static load on the response of a radial excitation.

   The radial static load is varied from 0 to 1600 N. A strong sine excitation ($F_r = 35$ N and $f_e = 320$ Hz) is added in the radial direction. Fig. 6.9**a** and 6.9**c** show the amplitude of the radial displacement and electrical resistance at the frequency of excitation and its second harmonic. At zero radial load, the electrical resistance shows a high second harmonic. The outer ring is then free to travel within the clearance of the bearing. The amplitude of the resistance w.r.t. the amplitude of the radial displacement is given in Fig. 6.9**e**. As the radial load increases and a stronger lubricant film forms, the response of the electrical resistance decreases.

   The variation of the electrical resistance due to a variation of the radial load is also derived from the mean resistance and the static bearing deformation. The mean electrical resistance is discussed in Sect. 4.4.2 and shown in Fig. 6.10**a**. The mean electrical resistance decreases as the bearing load increases, due to a reduction of the lubricant film thickness and an increase of the surface area of each contact. The variation of the mean electrical resistance per unit of load is given by the derivative of Fig. 6.10**a**. Fig. 6.10**c** shows the absolute value of this derivative. Also, the bearing deformation per unit of load is equal to the inverse of the bearing stiffness. The stiffness is discussed in Sect. 5.2.1 and given in Fig. 5.7**a**. The variation of the electrical resistance per unit of displacement therefore equals the ratio between both and is shown in Fig. 6.10**e**. This figure also includes the variation of the electrical resistance derived from the radial excitation. The variation of the electrical resistance due to an external excitation is similar to the variation due to a change of the static bearing load. The lubricant film thickness thus follows the imposed variations of the dynamic excitation. Breakdown of the lubricant film due to the dynamic excitation is not detected. At a low radial static load, the correspondence deteriorates due to the nonlinear motion of the bearing through its clearance.

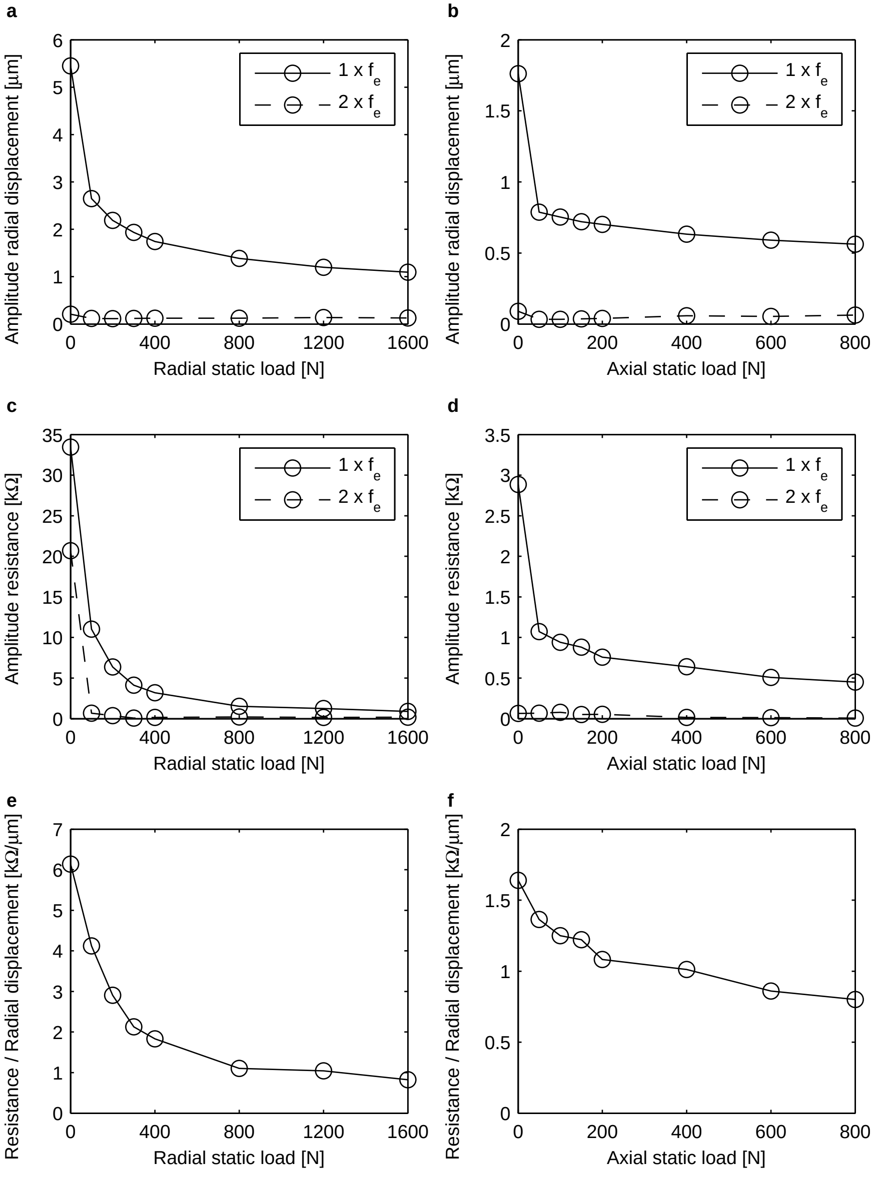

Figure 6.9: Radial excitation: amplitude of the radial displacement (**a**), resistance (**c**) and resistance w.r.t. displacement (**e**) while the radial static load is varied. Amplitude of the radial displacement (**b**), resistance (**d**) and resistance w.r.t. displacement (**f**) while the axial static load is varied.

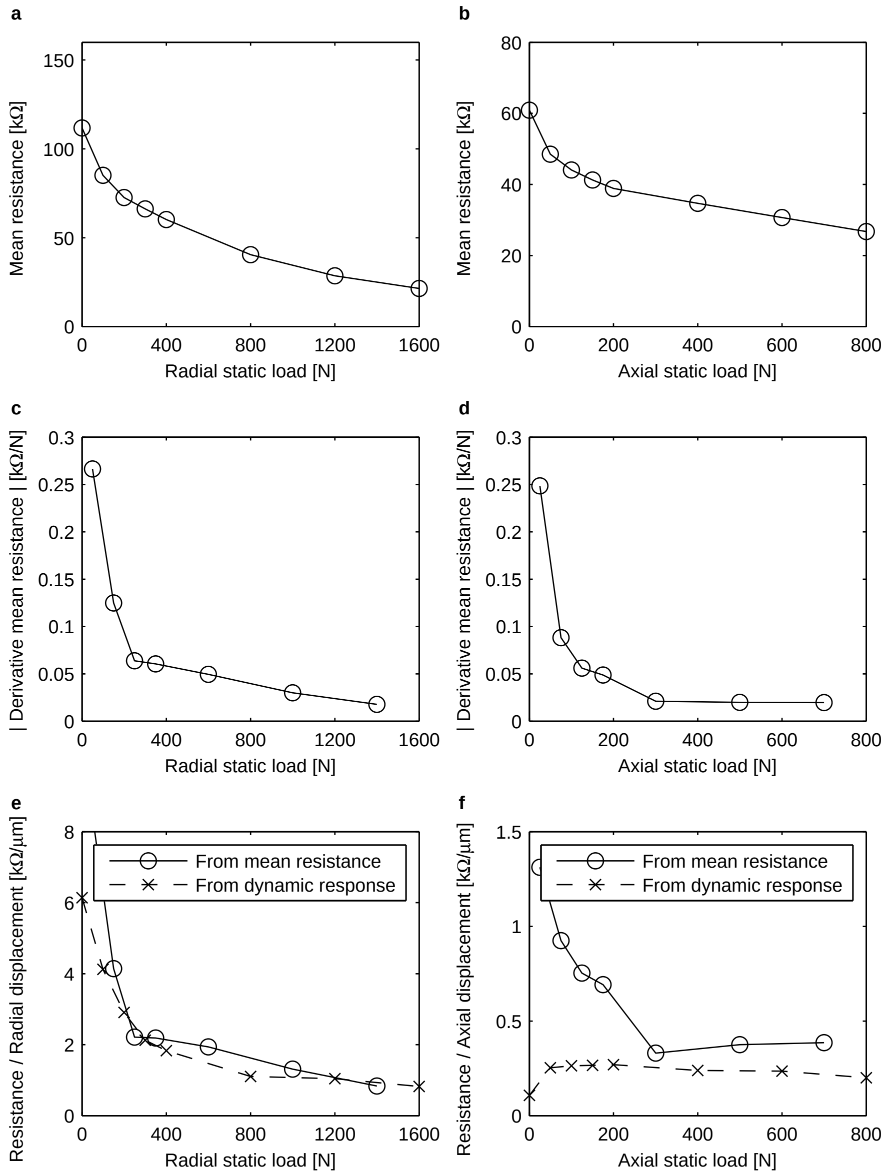

Figure 6.10: Mean electrical resistance during a run-up of the radial (**a**) and axial (**b**) static load. Derivative of the mean electrical resistance w.r.t. the radial (**c**) and axial (**d**) static load. Variation of the resistance w.r.t. the radial (**e**) and axial (**f**) displacement.

2. The influence of the axial static load on the response of a radial excitation.

   The axial static load is increased from 0 to 800 N while a 400 N radial static load is simultaneously applied. A strong sine excitation (F_r = 35 N and f_e = 320 Hz) is added in the radial direction. Fig. 6.9**b**, 6.9**d** and 6.9**f** summarise the results. When increasing the axial load, a stronger lubricant film forms and the response of the electrical resistance decreases.

3. The influence of the radial static load on the response of an axial excitation.

   The radial static load is varied from 0 to 1600 N. A strong sine excitation (F_a = 35 N and f_e = axial rigid body mode) is added in the axial direction. The excitation frequency ranges from 118 to 231 Hz due to an increasing axial bearing stiffness at higher load levels. The axial bearing stiffness is not discussed in chapter 5, but derived in the same way as the radial bearing stiffness. The axial stiffness increases from 1.4x10^6 to 5.5x10^6 N/m when the radial static load increases from 0 to 1600 N. A theoretical zero axial stiffness at 0 N is not seen. When no pressure is applied, the rubber sleeves are stiff and the air springs deliver a small force. Fig. 6.11**a**, 6.11**c** and 6.11**e** show the results of the axial excitation during a run-up of the radial load. Recalling Fig. 6.6, the contact angle α follows the axial displacement. When increasing the radial static load, the variation of the contact angle reduces and the response of the lubricant film becomes more linear. The second and higher harmonics of the lubricant's response reduce. Also when increasing the radial static load, a stronger lubricant film forms. A consequential decrease of the lubricant's response is observed (Fig. 6.11**e**).

4. The influence of the axial static load on the response of an axial excitation.

   The axial static load is increased from 0 to 800 N while a 400 N radial static load is simultaneously applied. A strong sine excitation (F_a = 35 N and f_e = axial rigid body mode) is added in the axial direction. The excitation frequency varies from 162 to 445 Hz. The axial stiffness equals 2.6x10^6 N/m when no axial load is applied. After introducing an axial load of 100 N, the axial stiffness jumps to 13.1x10^6 N/m. A contact angle forms and all rolling elements are loaded. A further increase to 20.3x10^6 N/m is measured when the axial load equals 800 N. Fig. 6.11**b**, 6.11**d** and 6.11**f** show the results of the axial excitation during a run-up of the axial load. Analogous to the results when varying the radial load, the variation of the contact angle reduces and the second and higher harmonics of the lubricant's response reduce at higher load levels. Also, a decrease of the lubricant's response is observed as a stronger lubricant film forms (Fig. 6.11**f**).

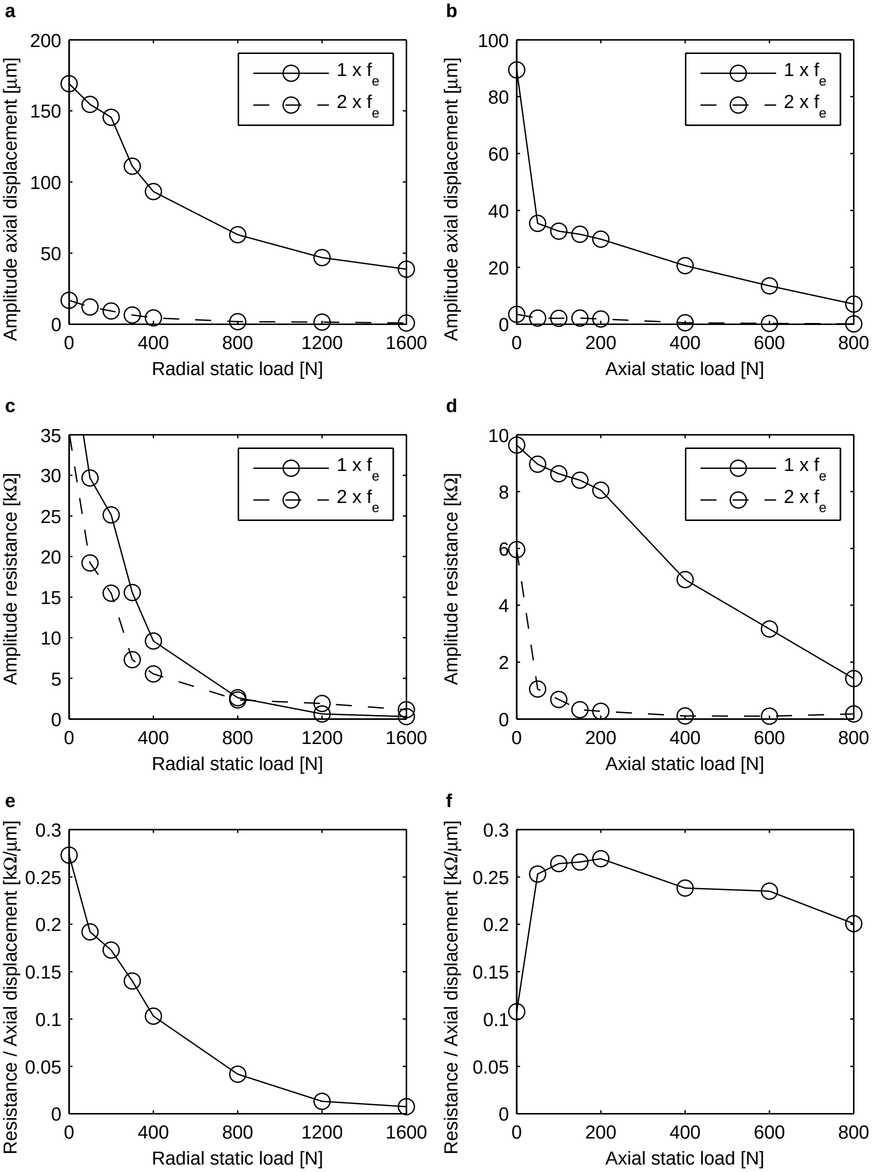

Figure 6.11: Axial excitation: amplitude of the axial displacement (**a**), resistance (**c**) and resistance w.r.t. displacement (**e**) while the radial static load is varied. Amplitude of the axial displacement (**b**), resistance (**d**) and resistance w.r.t. displacement (**f**) while the axial static load is varied.

The variation of the electrical resistance due to a variation of the axial load is also derived from the mean resistance and the static bearing deformation. The mean electrical resistance is shown in Fig. 6.10**b**. The variation of the mean electrical resistance per unit of load is given by the derivative of Fig. 6.10**b**. Fig. 6.10**d** shows the absolute value of this derivative. Using the bearing axial stiffness, the variation of the electrical resistance per unit of displacement is obtained and given in Fig. 6.10**f**. This figure also includes the variation of the electrical resistance derived from the axial excitation. In this way, the variation of the electrical resistance due to an external excitation is compared to the variation due to a change of the static bearing load. Good correspondence is only possible when the lubricant's response is linear. The nonlinear response at low levels of the axial static load (Fig. 6.11**d**) leads to large deviations. At load levels above 300 N axial static load, the response of the electrical resistance due to an external excitation and the variation due to a change of the static bearing load have the same order of magnitude. Similar to the radial excitation, the response of the lubricant film due to a dynamic excitation is linked to the variation of the lubricant film thickness. Breakdown of the lubricant film is not detected, as also concluded from Fig. 6.7.

6.1.6 Lubricant response: influence of the temperature

The influence of the temperature on the response of a dynamic excitation is analysed during the first 40 min of a warm-up. The bearing rotates at 1000 r/min while a 1000 N radial load is applied. The response is measured every 3 min based on a measurement of the electrical resistance of 3 min. Fig. 6.12 shows the results for both a radial ($F_r = 35$ N and $f_e = 320$ Hz) and axial ($F_a = 35$ N and $f_e =$ axial rigid body mode) excitation.

While the outer ring temperature increases (Fig. 6.12**a**), the mean electrical resistance strongly decreases (Fig. 6.12**b**). The relation between the lubricant's temperature and the electrical resistance is discussed in Sect. 4.4.3. The structure's dynamics hardly change during the measurement (Fig. 6.12**c** and 6.12**d**) and should not be taken into account. The response of the electrical resistance to the radial (Fig. 6.12**e**) and axial (Fig. 6.12**f**) excitation shows an increasing trend.

Without external excitation, no metallic contact is observed during the first 10 min of the warm-up (Sect. 4.4.3). The lubricant's viscosity is high and a thick film is formed. The current measurements show a small and constant response to a dynamic excitation during these first 10 min. As the lubricant's viscosity

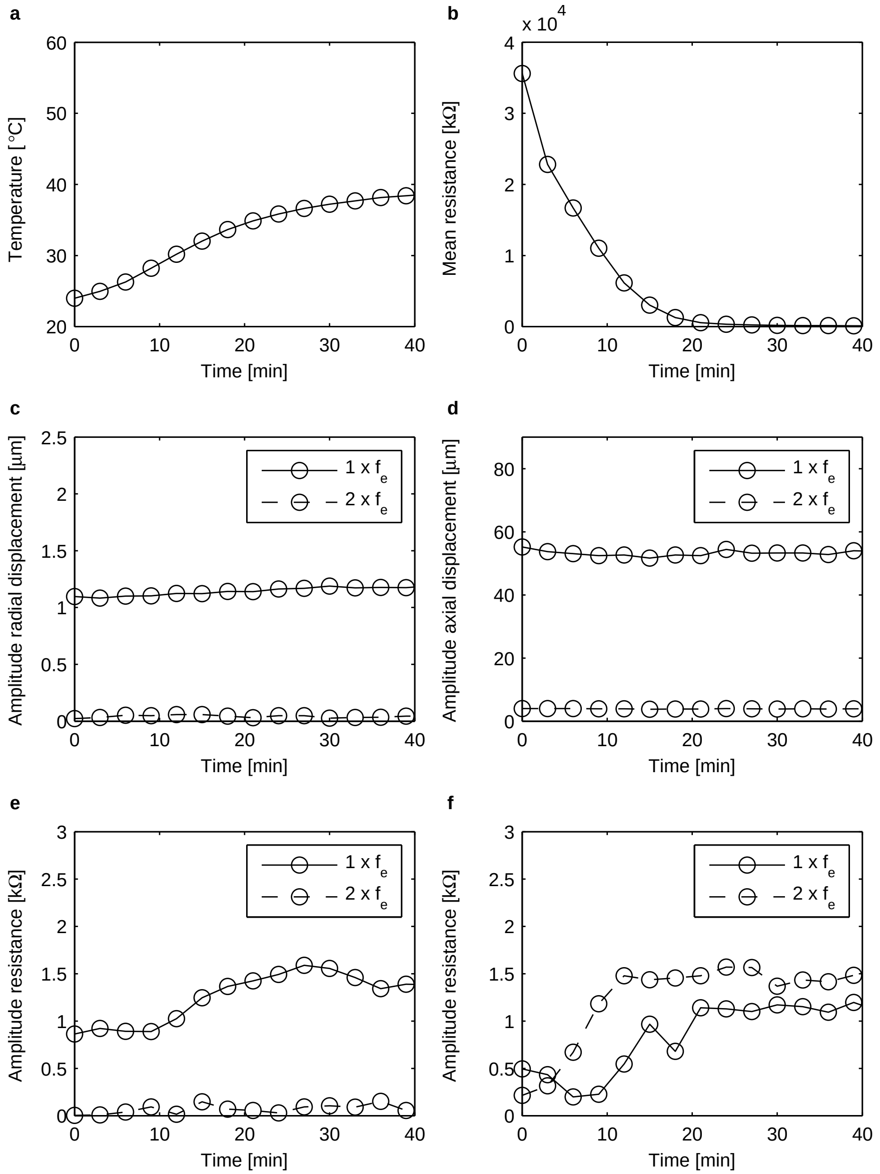

Figure 6.12: Temperature (**a**) and mean electrical resistance (**b**) during a warm-up. Response of the bearing displacement (**c**) and electrical resistance (**e**) due to a radial dynamic excitation and the response of the bearing displacement (**d**) and electrical resistance (**f**) due to an axial dynamic excitation.

further decreases during the warm-up, the lubricant film further weakens and an increase of the response of the electrical resistance is measured.

When repeating the same measurement, the increase of the response is not clearly observed each time. A decrease of the lubricant's resistivity during the warm-up (Sect. 4.4.3) possibly influences the results.

6.1.7 Lubricant response: influence of the speed

The influence of the speed is analysed during a run-up of the speed from 0 to 1500 r/min. A 1000 N radial load is applied. Additionally, a radial ($F_r =$ 35 N and $f_e =$ 320 Hz) and axial ($F_a =$ 35 N and $f_e =$ axial rigid body mode) excitation are separately added. Fig. 6.13 summarises the results, analogous to Fig. 6.12.

The tests are performed in isothermal conditions and the mean resistance reveals the formation of the lubricant film (Sect. 4.4.4). The structure's dynamics hardly change during the measurement and should not be taken into account. Up to 200 r/min, the lubricant is squeezed out of the contacts. As the electrical resistance equals zero, so is the variation of the resistance at the excitation frequency. At speeds from 200 to 600 r/min, the lubricant film is forming. Both the mean resistance and the variation of the resistance increase. When further increasing the speed, the film formation continues. The variation of the electrical resistance is no longer affected by the speed.

The bearing load and temperature are constant during the tests. As the pressure and temperature are fixed, the viscosity of the lubricant is solely determined by the shear rate (Sect. 2.2.1). In Sect. 4.5, cage slip up to 1% is measured. The sliding motion in the contacts during normal bearing operation is thus limited. A consequential constant response of the lubricant film is observed, once the lubricant film is sufficiently formed.

6.2 Frictional power loss under dynamic load

When introducing an external dynamic excitation on the bearing, the lubricant film thickness follows the imposed variations of the load. Variations of the lubricant film thickness are similar to the variations when the magnitude of the static bearing load is changed. An increase of metallic contact or breakdown of the lubricant film is not detected. The bearing temperature however increases during dynamic excitation. This section analyses the frictional power loss

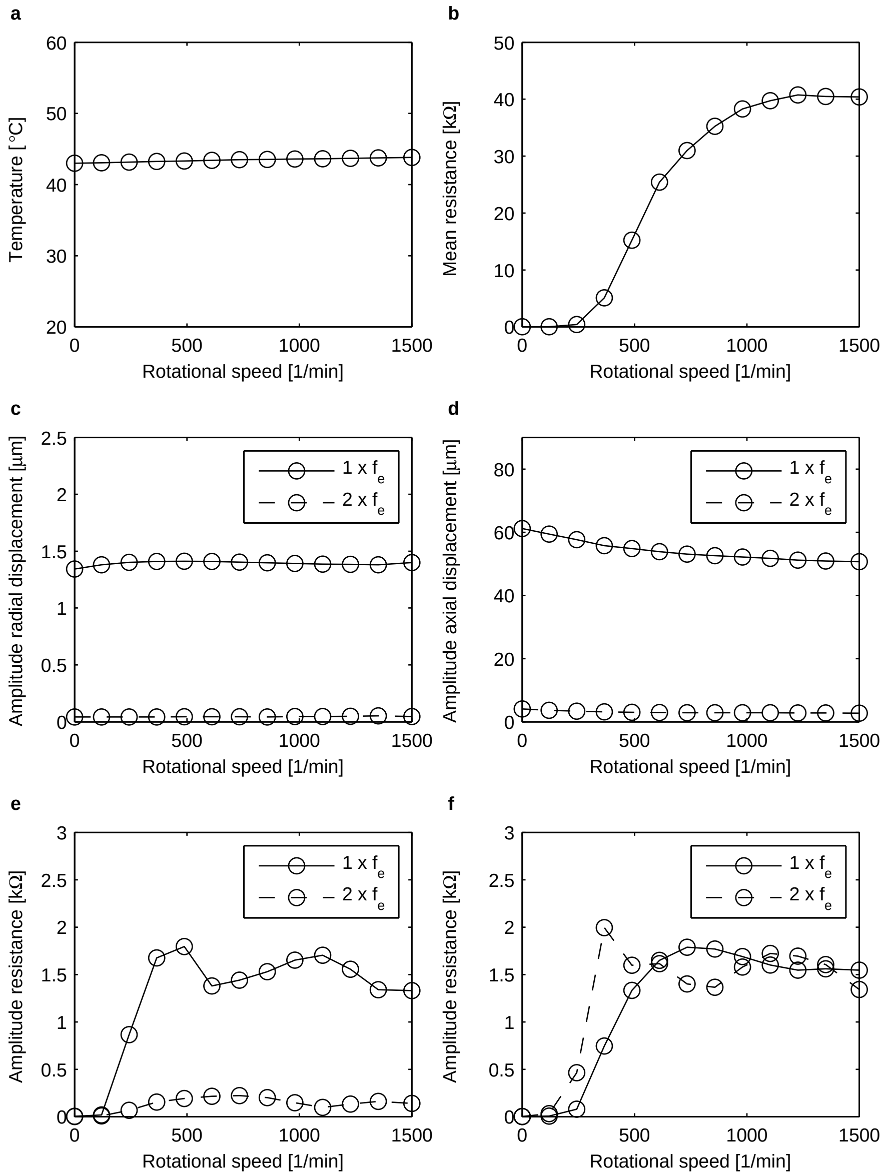

Figure 6.13: Temperature (**a**) and mean electrical resistance (**b**) during a run-up of the speed. Response of the bearing displacement (**c**) and electrical resistance (**e**) due to a radial dynamic excitation and the response of the bearing displacement (**d**) and electrical resistance (**f**) due to an axial dynamic excitation.

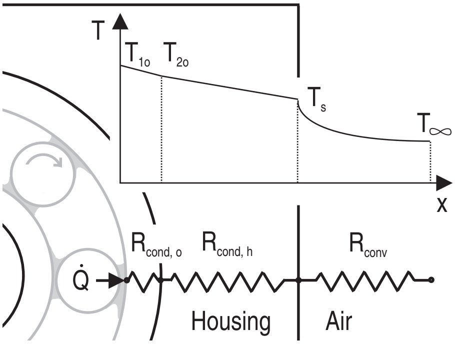

Figure 6.14: Thermal model of the heat transfer from the outer ring to the environment.

proportional to the temperature increase of the bearing. The heat generation mechanism is identified.

6.2.1 Thermal analysis of the test bearing

Frictional heat is generated in the contacts of the bearing. A part of this heat is dissipated by conduction through the outer ring and housing and by convection to the environment. The heat transfer from the outer ring to the environment is described by the model of Fig. 6.14. The frictional power loss $\dot{Q}$ expresses the heat transfer rate. The thermal resistance related to the heat transfer through the outer ring is given by the conduction resistance $R_{cond,o}$. The temperature decreases from T_{1o} at the rolling element side to T_{2o} at the housing side. The heat further passes the conduction resistance of the housing $R_{cond,h}$ and the convection resistance R_{conv}. Through convection, the temperature decreases from T_s at the housing surface to T_∞ (ambient temperature). Such simplified representation is often used to solve steady heat transfer problems. The approach assumes i.e. a constant surface temperature.

The relation between the frictional power loss $\dot{Q}$, the measured outer ring temperature T_{2o} and the temperature of the environment T_∞ is given by:

$$T_{2o} - T_\infty = \dot{Q}\ (R_{cond,h} + R_{conv}) \tag{6.1}$$

While the conduction resistance $R_{cond,h}$ is independent of the temperature (as stated by Fourier's law of conduction), the convection resistance R_{conv} is not. The dependency should be determined experimentally or numerically and is generally given by the Nusselt number w.r.t. the Grashof number. For small variations of the temperature, a constant convection resistance is often assumed.

When introducing an external dynamic excitation while the bearing rotates at 1000 r/min, variations of the outer ring temperature up to 15% are measured (Sect. 6.2.2). A convection resistance independent of the temperature is assumed. The frictional power loss through the outer ring due to the dynamic excitation is then proportional to the outer ring temperature (Eq. 6.1). It should be noted that frictional heat is generated in both the inner and outer ring contacts and dissipated through both the inner and outer ring. The outer ring temperature only reveals the power loss dissipated through the outer ring. A second assumption is made, stating that the power loss dissipated through the outer ring is proportional to the total power loss resulting from friction in the inner and outer ring contacts. This allows evaluating the total power loss based on the measured outer ring temperature.

6.2.2 Analysis of the frictional power loss

The frictional power loss due to an external excitation is analysed based on the outer ring temperature T_{2o}. A thermocouple is mounted to the outer ring and located in the loaded zone of the radial load. When changing the static load, dynamic load or rotational speed, the temperature is recorded after the bearing's temperature has reached its stable value. Random temperature fluctuations over time up to 0.5 °C are observed after the stable value is reached. Consistent trends of the temperature increase due to an external dynamic excitation are found after repeating the same tests three times. Variations of the ambient temperature T_∞ are taken into account as well, by correcting the outer ring temperature when the ambient temperature changes between successive tests.

The effect of a radial, axial and combined radial and axial excitation is analysed. Excitation at the resonance frequencies of the rigid body modes is chosen in order to obtain high bearing displacements. The bearing rotates at 1000 r/min and a 1000 N radial load is applied. The following load cases are separately investigated:

1. A radial sine excitation ($F_r = 35$ N and $f_e =$ radial rigid body mode) is added. The amplitude of the resulting radial displacement equals 6.9 µm. However, no measurable increase of the outer ring temperature is observed.
2. An axial sine excitation ($F_a = 35$ N and $f_e =$ axial rigid body mode) is added. The amplitude of the resulting axial bearing displacement equals 61 µm. After 4 hours, a new stable temperature is reached. The temperature increase due to this dynamic excitation equals 2.7 °C.

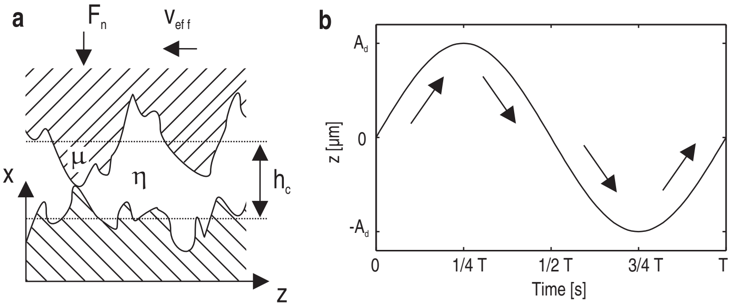

Figure 6.15: Formation of a lubricant film and random metallic contact of asperities (**a**). The sinusoidal displacement of the outer ring under axial excitation (**b**).

3. An axial sine excitation ($F_a = 35$ N and $f_e \neq$ axial rigid body mode) is added. The axial bearing displacement is small and no temperature increase is observed.

4. A combined sine excitation in the radial ($F_r = 35$ N and $f_e =$ radial rigid body mode) and axial ($F_a = 35$ N and $f_e =$ axial rigid body mode) direction is added. A similar increase of the outer ring temperature as seen in the second case is measured. No effect of the radial dynamic load is seen.

5. An axial static load of 35 N is added. No measurable increase of the outer ring temperature is observed.

A significant increase of the bearing temperature is seen when a strong axial excitation is applied. Frictional power loss results from this axial motion under high radial static load. Recalling that $\Lambda \approx 1$, asperities of the rolling element and raceway surfaces make random metallic contact during normal bearing operation. Fig. 6.15**a** sketches this condition of mixed friction [77]. The axial motion leads to an effective shear velocity v_{eff}, while the normal load F_n results from the high radial static load. The power loss is linked to Coulomb friction between the asperities, viscous friction in the lubricant film or a combination of both.

When assuming shear motion between two flat plates with a coefficient of friction μ, the power loss $\dot{Q}_c$ due to Coulomb friction is proportional to the normal load and the effective velocity:

$$\dot{Q}_c = \int \mu \; F_n \; \mathrm{d}v_{eff} = \mu \; F_n \; v_{eff} \tag{6.2}$$

When assuming shear motion between two flat plates separated by a lubricant film with viscosity η, the power loss $\dot{Q}_v$ due to viscous friction is derived using Eq. 2.17. The power loss is proportional to the lubricant's viscosity and the square of the effective velocity:

$$\dot{Q}_v = \int \eta \; A \; \frac{v_{eff}}{h_c} \; \mathrm{d}v_{eff} = \eta \; A \; \frac{v_{eff}^2}{2 \; h_c} \tag{6.3}$$

In these equations, the effective velocity or total travelled distance per unit of time is derived from the displacement imposed by the shaker. The shaker sinusoidally excites the bearing outer ring. The resulting relative motion w.r.t. the inner ring is a sinusoidal displacement with an amplitude A_d and frequency f_e. During one period, the distance A_d is travelled 4 times (Fig. 6.15**b**). As f_e cycles occur per unit of time, the effective velocity of the outer ring equals:

$$v_{eff} = 4 \; A_d \; f_e \tag{6.4}$$

The following sections discuss the frictional power loss for different levels of the axial excitation and different operational conditions. The measured relations reveal that Coulomb friction is the heat generation mechanism.

6.2.3 Frictional power loss: influence of the amplitude

Varying the amplitude of the axial excitation shows the influence of the effective velocity on the frictional power loss. Following Eq. 6.4, the effective velocity is proportional to the amplitude of the axial displacement A_d. A radial load of 1000 N is applied and the bearing rotates at 1000 r/min. An axial excitation at the resonance frequency of the axial rigid body mode is added and the increase of the outer ring temperature is measured. Different amplitudes of the excitation are analysed separately. Fig. 6.16 shows the increase of the temperature for different amplitudes of the axial displacement.

Recalling Coulomb friction due to shear motion between two plates (Eq. 6.2), the power loss is proportional to the effective velocity. When a lubricant film is added between the plates (Eq. 6.3), the power loss is proportional to the square of the effective velocity. The current measurement results of the bearing temperature mostly correspond to the linear trend of ideal Coulomb friction.

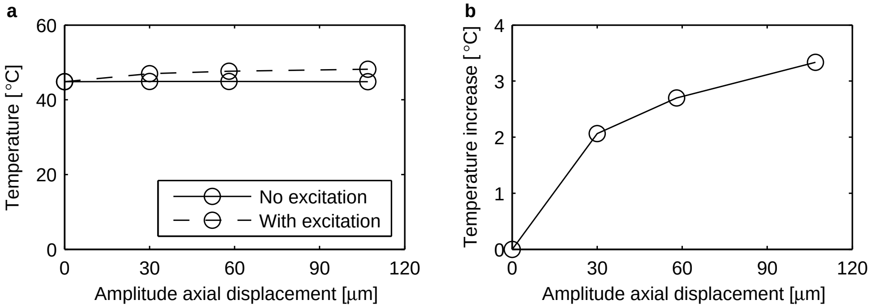

Figure 6.16: Increase of the outer ring temperature w.r.t. the amplitude of the axial excitation. Both the outer ring temperature (**a**) and the temperature increase (**b**) are shown.

During axial excitation, Sect. 6.1.3 shows a nonlinear response of the lubricant film due to the nonlinear motion of the rolling elements and the variation of the EHL film location. The nonlinear motion of the rolling elements possibly explains why the temperature increase veers off the expected linear trend at higher excitation amplitudes.

6.2.4 Frictional power loss: influence of the load

Different levels of the radial static load are investigated while the bearing rotates at 1000 r/min. In order to obtain a strong axial excitation, the excitation frequency corresponds to the frequency of the axial rigid body mode. The amplitude of the excitation is controlled such that the effective velocity v_{eff} is fixed. Fig. 6.17 summarises the temperature increase measured at different load levels.

When increasing the radial static load:

- The rolling element loads increase. Recalling Fig. 4.3, the normal load F_n in each contact increases (approximately) proportionally to the radial static load.
- The contact pressure between the rolling elements and raceways increases. The lubricant's viscosity η subsequently increases.
- The contact surface area A between the rolling elements and raceways increases and the lubricant film thickness h_c decreases. Also, more metallic

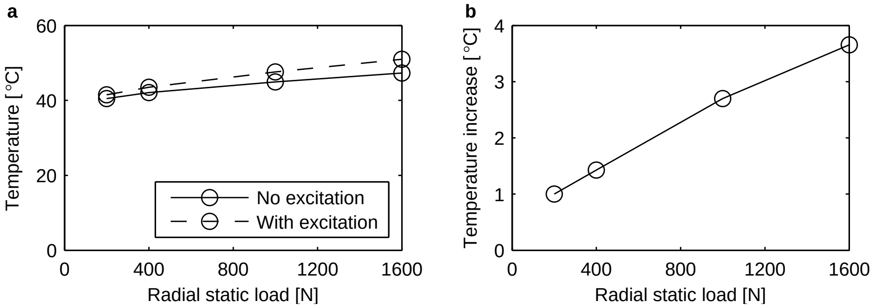

Figure 6.17: Increase of the outer ring temperature w.r.t. the radial static load. Both the outer ring temperature (**a**) and the temperature increase (**b**) are shown.

contact between asperities of the rolling elements and raceways occurs (Sect. 4.4.2).

Recalling Coulomb friction due to shear motion between two plates, the power loss is proportional to the normal load. The power loss is independent of the surface area of metallic contact. When a lubricant film is added between the plates, viscous friction occurs. The power loss is proportional to the lubricant's viscosity and increases thus drastically with the contact pressure (Sect. 2.2.1). The contact surface area and lubricant film thickness further influence the power loss. The current measurement results of the bearing temperature correspond to the linear trend of ideal Coulomb friction.

6.2.5 Frictional power loss: influence of the speed

Different rotational speeds of the bearing are investigated while a radial static load of 1000 N is applied. An axial excitation at the resonance frequency of the axial rigid body mode is added after the bearing reached its stable temperature at a given speed. The effective velocity is fixed for all tests. Fig. 6.18 shows the temperature increase due to the axial excitation.

At 0 r/min, a significant temperature increase of 1.9 °C due to the dynamic excitation is measured. As the lubricant is squeezed out of the contacts leaving pure metal-to-metal contact, Coulomb friction is the heat generation mechanism. When increasing the rotational speed of the bearing, a lubricant film is formed and the amount of metallic contact between asperities reduces (Sect. 4.4.4). The temperature increase initially increases. Above 900 r/min, a decrease is

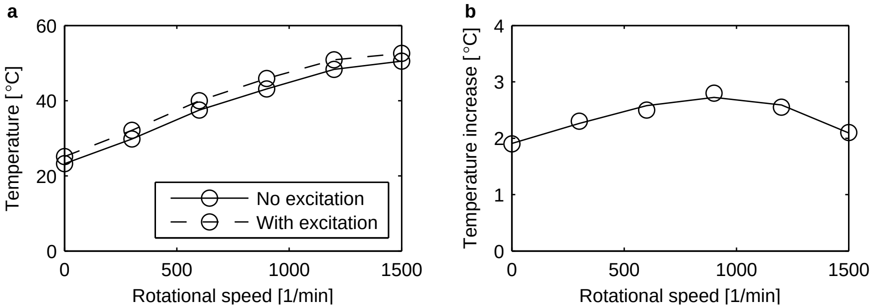

Figure 6.18: Increase of the outer ring temperature w.r.t. the bearing rotational speed. Both the outer ring temperature (**a**) and the temperature increase (**b**) are shown.

observed. Interestingly, Gegner [77] observes the same trend when analysing the increase of temperature of the outer ring of a cylindrical roller bearing. A maximum temperature increase is observed at 1000 r/min.

Recalling Coulomb friction due to shear motion between two plates, the power loss is independent of the surface area of metallic contact. Keeping the effective velocity and normal load constant, a constant power loss is expected. A measured variation of the temperature increase w.r.t. the speed reveals a possible influence of the lubricant film formation. Gegner reasons that the mean coefficient of friction over the contact surfaces decreases when a lubricant film is formed. The mean coefficient of friction takes into account the friction of asperities in contact and friction of the lubricant film. A consequential decrease of the power loss is expected, analogous to the observations of Stribeck for hydrodynamic lubrication. The theory of Stribeck [104] shows a decrease of the coefficient of friction when a lubricant film is introduced between the contacting surfaces.

It should be noted that the steady-state temperature of the outer ring strongly differs between the measurements at different speeds. Variation of the convection resistance between measurements from 0 to 1500 r/min possibly influences the measured temperature increase.

6.3 Accelerated lifetime tests under dynamic load

Under axial excitation, sliding motion between asperities of the contacting surfaces in the bearing occurs. Based on the temperature increase due to Coulomb friction between asperities, the optimal conditions for accelerated lifetime tests under high axial dynamic load can be derived. Accelerated lifetime tests are performed on a series of deep groove ball bearings 6302. This section first introduces the test conditions, the test duration and the transmitted bearing force. After completion, damage of the raceway surfaces due to external dynamic loads is investigated using a scanning electron microscope.

6.3.1 Test conditions

Three bearings are dynamically loaded in three different ways:

- Radial dynamic load applied.
- Axial dynamic load applied.
- Radial and axial dynamic load simultaneously applied.

The operational conditions of the tests are determined such that the influence of external dynamic loads is expected to be maximal.

A fourth bearing is tested under the same operational conditions, but without an external dynamic load applied. This bearing serves as a reference when analysing the influence of the dynamic load.

Rotational speed

The test bearing rotates at 1000 r/min. Recalling Sect. 6.2.5, the frictional power loss due to sliding motion between asperities reaches its maximum at approximately 1000 r/min. The additional tangential loads on the raceway surfaces are maximal and so is the surface wear due to dynamic loads.

Static load

A radial static load of 950 N is applied on the test bearing. A high radial load is desired in order to obtain high tangential loads due to sliding between asperities (Sect. 6.2.4). No axial static load is applied on the test bearing, such that high axial displacements are obtained during shaker excitation. The maximum contact pressure on the outer ring equals approximately 2000 MPa (Sect. 4.4.1). The radial load of 950 N thus represents a high but realistic and common loading condition.

Dynamic load

Sine excitation resulting from a structural resonance or gear meshing is simulated. The frequency of the radial excitation is 536 Hz and corresponds to the frequency of the radial rigid body mode. The frequency of the axial excitation is 191 Hz and corresponds to the frequency of the axial rigid body mode. The amplitude of the load is controlled and fixed to 50 N in both directions. This results in an amplitude of the radial bearing displacement of 9.8 µm during radial excitation. An amplitude of the axial bearing displacement of 90.5 µm is measured during axial excitation.

6.3.2 Test duration

Based on the static bearing load, the ratio of the dynamic load rating w.r.t. the equivalent dynamic load C/P equals 12.5. According to Eq. 2.22, the calculated L_{10} life equals 1365 days. As discussed in Sect. 2.4.3, Gegner [28] already observes the first surface cracks and material delamination after 10^7 inner ring revolutions of the lifetime tests. An equal number of inner ring revolutions is chosen for the current tests. This corresponds to a test duration of 7 days of continuous operation and 0.5% of the calculated L_{10} life.

It should be noted that the dynamic load is applied continuously during the tests. In practical applications, high vibration levels only occur during limited time spans. This, for instance during starting, braking and emergency stops of wind turbines. Also, the operational conditions of the bearing are selected such that surface wear due to sliding between asperities is maximised. The current tests are thus considered being accelerated lifetime tests.

6.3.3 Transmitted force through the bearing

Both for the radial and axial dynamic load, the excitation frequency corresponds to the frequency of a translational rigid body mode. The transmitted force through the test bearing is therefore higher than the shaker force. The spring-mass-damper model of Sect. 5.1.3 allows estimating the transmitted force. The model is derived for both a radial and axial excitation. The transmitted force through the bearing is given by:

$$F_t = k_{TB+MS}\left(x_2 - x_1\right) + c_{TB+MS}\left(\dot{x}_2 - \dot{x}_1\right) \tag{6.5}$$

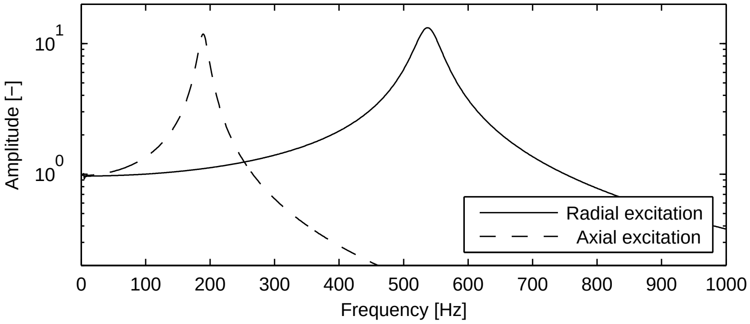

Figure 6.19: FRF of the transmitted force through the test bearing during radial and axial excitation.

Fig. 6.19 shows the ratio of the transmitted force w.r.t. the shaker force. At resonance, an amplification of 12.2 in the radial direction and 11.8 in the axial direction is expected. Recalling that the amplitude of the shaker force equals 50 N in both directions, the radial and axial force through the bearing each exceed 500 N. Due to the axial excitation, a significant contact angle is introduced which varies at the frequency of excitation. Due to the radial excitation, a combined static and dynamically transmitted radial load up to 1560 N is applied. The maximum contact pressure reaches peaks up to 2340 MPa.

The estimation of the transmitted force strongly depends on the identified bearing damping. As explained in Sect. 5.1.4, the identification of the bearing damping is most susceptible to errors. This analysis is only used to roughly estimate the transmitted force.

6.3.4 Analysis of the raceway surfaces

After completion of the accelerated lifetime tests, the raceway surfaces of the tested bearings are analysed. The centre of the inner ring raceway surface is investigated using a light optical microscope (LOM) and a scanning electron microscope (SEM). The PHILIPS SEM XL30 FEG uses a secondary electron detector. The beam accelerating voltage is set at 10 kV. In the microscope images of this manuscript, the overrolling direction equals the vertical direction.

Polishing of the honing structure under axial excitation

Polishing of the honing structure under axial excitation is clearly observed when comparing the raceway surface of bearings tested with and without axial dynamic load. Fig. 6.20 compares the raceway surface of two bearings using a LOM. In Fig. 6.21, the same surfaces are analysed under the same magnification using a SEM. The left (**a**) and right (**b**) images show the surface of a bearing tested respectively without and with axial dynamic load.

Sharp edges appear as white lines in SEM images, as electrons concentrate in these areas. The rough honing marks of the bearing tested without axial dynamic load are consequently highlighted in these images. The honing marks of the bearing tested with axial dynamic load are polished and thus do not appear. In the LOM images, polishing of the honing structure cannot be seen.

Polishing wear of the surfaces, such as surface cracks and material delamination, is not yet observed. As discussed in Sect. 2.4.3, Gegner [28] detects this wear after an equal number of inner ring revolutions when analysing cylindrical roller bearings. Lipless cylindrical roller bearings allow higher axial displacements, such that a higher effect of dynamic loads is expected. The test duration of the current lifetime tests should be increased in order to observe possible polishing wear.

Grey matted surface due to arc discharge in the lubricating gap

Both the LOM and SEM images of the tested bearings show grey matted surfaces along the honing marks and indentations. For instance, the honing mark in the middle of Fig. 6.20**b** and 6.21**b** is surrounded by these surfaces. As identified at the SKF Material Physics laboratory Schweinfurt, they result from arc discharge in the lubricating gap. The resulting shallow remelted craters of a few micron in diameter and depth cover the raceway surfaces. They are mostly observed along the honing marks and indentations, as the lubricant film formation is worse in these areas.

Arc discharge in the lubricating gap is caused by high frequency electric current passage through the test bearing. It is expected to result from leaking motor currents. Grounding of the spindle shaft is later added to the test rig.

Sliding marks under axial excitation

When comparing the raceway surface of bearings tested with and without axial dynamic load, another difference is noted. The raceway surfaces of the bearings

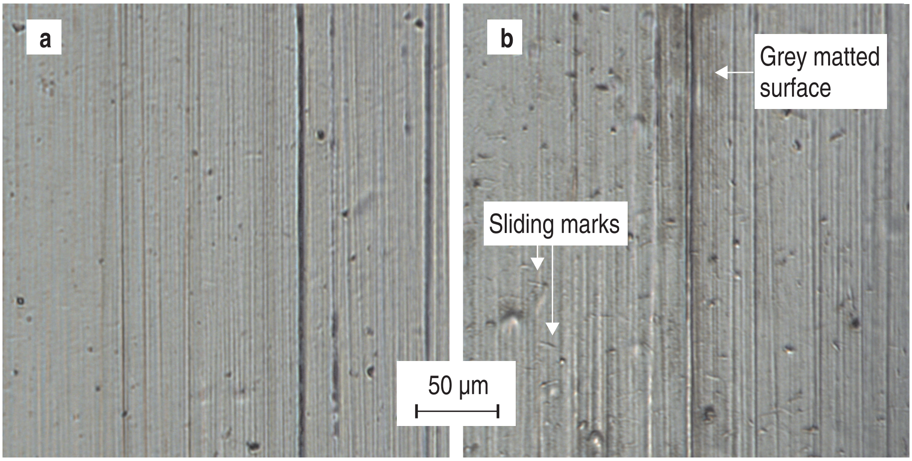

Figure 6.20: LOM images of inner raceway surface (overrolling in the vertical direction): test without (**a**) and with (**b**) axial dynamic load.

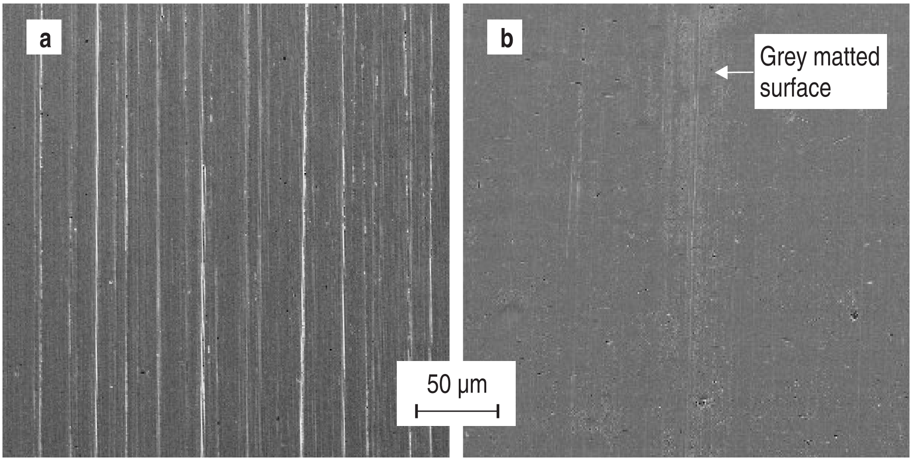

Figure 6.21: SEM images of inner raceway surface (overrolling in the vertical direction): test without (**a**) and with (**b**) axial dynamic load.

tested under high axial dynamic load are covered by sliding marks (Fig. 6.20). These marks are up to 10 μm long and mainly oriented in the axial direction. Fig. 6.22 shows such a sliding mark for two levels of magnification. Shallow remelted craters resulting from arc discharge are observed at the edges of these marks.

The sliding marks are caused by axial sliding of solid particles embedded in the opposing surfaces. While clearly visible on the raceway surfaces, the marks are less important when analysing surface damage. Premature failure under high axial load is caused by polishing wear, rather than the development of these marks.

Indentations due to solid particles in the contacts

The bearing tested with only an axial dynamic load applied reveals indentations on the raceway surfaces. The areas of sharp-edged indentations are up to 100 μm long. Fig. 6.23 shows such indentations for two levels of magnification. As discussed in Sect. 2.4.1, the indentations are formed during overrolling of solid particles. They do not result from the external dynamic loads applied during the test.

Radial versus axial excitation

Due to an axial excitation, polishing of the honing structure and the appearance of axial sliding marks are noted. The effect of a radial excitation is not seen.

When introducing a pure radial dynamic load, the lubricant film thickness varies at the frequency of excitation (Sect. 6.1.3). An effect of the excitation on the condition of the raceway surfaces is neither expected nor seen.

Recalling Sect. 2.4.3, a higher Hertzian pressure amplifies the effect of vibration-induced mixed friction. When adding a radial dynamic load to the axial dynamic load, an increased effect of the axial excitation is expected. This is not seen in the LOM and SEM images of the current tests. XRD analysis of the raceway surfaces is required for further investigation.

6.3.5 Condition monitoring during tests

During the accelerated lifetime tests, the radial bearing acceleration is periodically measured. No dynamic load is applied on the test bearing during these measurements. Fig. 6.24**a** shows the RMS values of the acceleration for

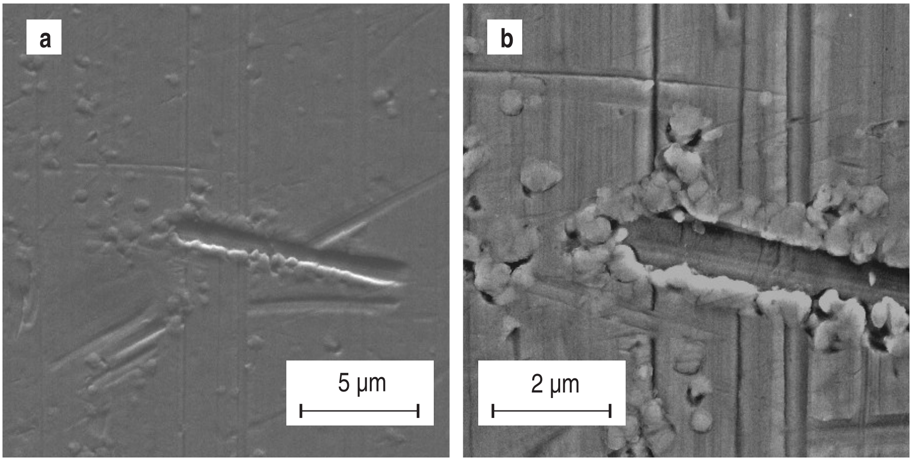

Figure 6.22: SEM images of a sliding mark (overrolling in the vertical direction): two levels of magnification (**a** and **b**).

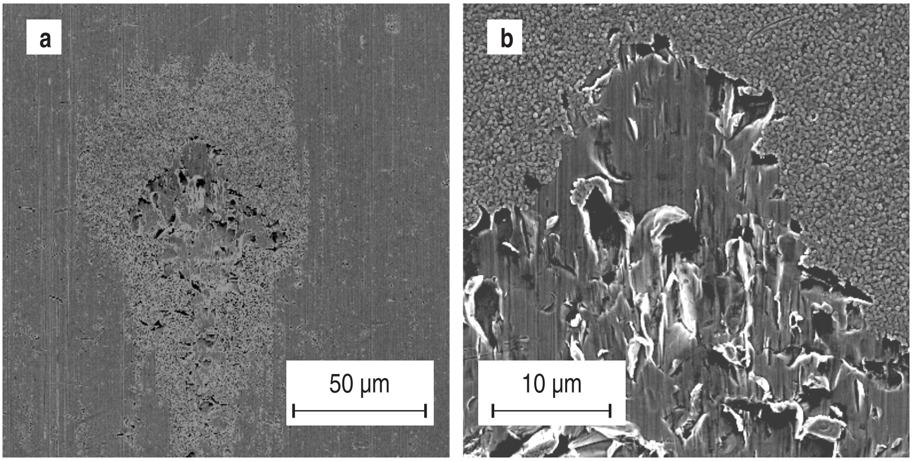

Figure 6.23: SEM images of an area of indentations (overrolling in the vertical direction): two levels of magnification (**a** and **b**).

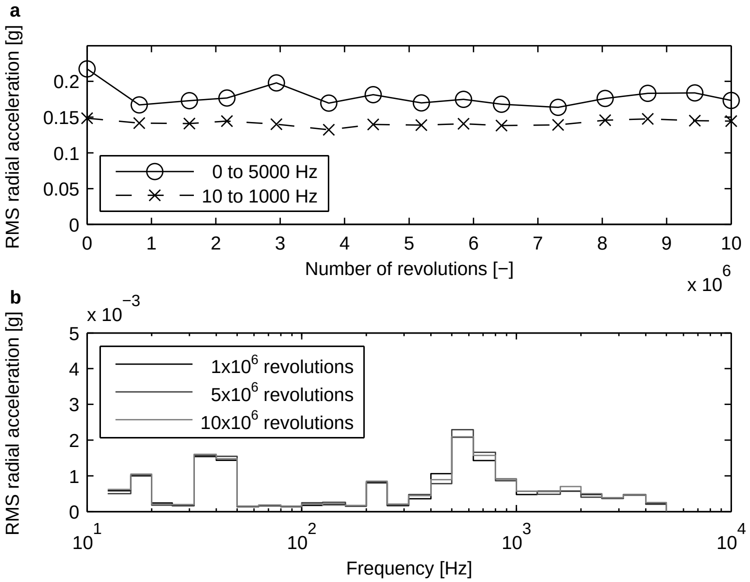

Figure 6.24: RMS of radial bearing acceleration during accelerated lifetime test (**a**) and CPB spectrum comparison for three different acceleration measurements (**b**).

the bearing tested with an axial dynamic load applied. A filtered version of the acceleration is further calculated, according to the ISO 10816-3 [55] standard for evaluation of machine vibrations. The frequency content from 10 to 1000 Hz is used to calculate the filtered RMS value (dashed line).

The overall vibration level is mainly determined by the level of the highest peak in the spectrum. Changes of smaller peaks are not detected. Earlier warning is given by the constant percentage bandwidth (CPB) spectrum comparison. The spectrum is divided into 1/3 octave bands and the RMS value of each band is calculated. Fig. 6.24**b** shows the spectrum comparison for three different acceleration measurements.

While the axial dynamic load has a clear influence on the condition of the raceway surfaces, consistent changes of the RMS acceleration and the CPB spectrum are not observed. Condition monitoring techniques typically detect spalls greater than 1 mm. Incipient bearing faults are not detected.

6.4 Conclusion

The electrical resistance through the bearing reveals the response of the lubricant film to dynamic excitations. When the excitation frequency corresponds to a resonance frequency of the bearing system, a strong bearing displacement and a strong response of the lubricant film are measured. The lubricant film thickness however follows the imposed variations of the load. The lubricant response is similar to the response when the magnitude of the static bearing load is changed. Also, the time fraction of metallic contact is unaffected by the dynamic load. Breakdown of the lubricant film is not detected.

The influence of the lubricant's viscosity on the response to dynamic excitations is analysed. The lubricant's viscosity increases when increasing the static bearing load. Then, a stronger lubricant film is formed and the response of the film to dynamic excitations decreases. The lubricant's viscosity decreases when increasing the bearing temperature. Then, a weaker lubricant film is formed and the response of the film to dynamic excitations increases. Experimental analysis of the lubricant film behaviour under dynamic load is not described in the current literature.

When introducing an axial dynamic load, sliding motion between asperities of the contacting surfaces in the bearing occurs. An increase of the bearing temperature under axial dynamic load is measured. Coulomb friction is identified as the heat generation mechanism. The frictional power loss due to sliding motion between asperities is proportional to the normal load in the bearing contacts. Also, significant power loss is measured during excitation of a stationary dry bearing.

The highest frictional power loss is measured when the excitation amplitude is maximised, the static radial load is maximised and the rotational speed equals approximately 900 r/min. Accelerated lifetime tests are performed in this condition. The additional tangential loads on the raceway surfaces are maximal and so is the surface wear due to dynamic loads.

Due to sliding motion between asperities, the raceway surfaces of bearings tested under high axial dynamic load reveal polishing of the honing structure. This polishing is clearly seen on SEM images of the inner raceway after a test duration of only 0.5% of the calculated L_{10} life. Polishing wear of the surfaces (such as surface cracks and material delamination) is not yet observed. The duration of the lifetime tests should be increased in future tests.

Chapter 7

Conclusion

To conclude the manuscript, the general research results and future perspectives of the presented work are discussed.

7.1 Research results

Being particularly critical components, the serviceability of rolling element bearings is usually essential for the machine's operation. They have been the subject of research for more than a 100 years. The work of this manuscript investigates two aspects of rolling element bearings. Firstly, the dynamic behaviour of a rolling element bearing is analysed. The study emphasises the influence of the lubricant film on the bearing dynamics. Secondly, the lifetime of the bearing is analysed. The study discusses the influence of external dynamic loads on the lubricant film formation and wear of the raceway surfaces.

The bearing dynamics and lifetime are experimentally analysed using an innovative and versatile test rig. The first contribution of the current work consists of the development of this test rig. The test rig is designed and constructed in-house, and characterised by three unique features. Firstly, the test rig allows easy adjustment to test different types and sizes of rolling element bearings. The test bearing is mounted in a modular structure consisting of an auxiliary shaft and an intermediate sleeve. Secondly, the test rig allows applying a multi-axial static and dynamic load on the test bearing. The bearing load is controlled in both the radial and axial direction, and has a static and dynamic component in both directions. Thirdly, the test rig allows simultaneous measurement of the bearing motion, the bearing dynamics and the behaviour of the lubricant film. Relations between the different measurements can be derived experimentally. The radial, axial and tilt motion are measured free from disturbances of the surrounding structure. The bearing dynamics are identified in a frequency range below the resonances of the surrounding structure's flexible modes. The behaviour of the lubricant film is analysed based on the electrical resistance through the bearing.

In the current study, a single row deep groove ball bearing is used as a test bearing. Three operational properties, namely the bearing motion, the behaviour of the lubricant film and cage slip, are analysed. Understanding these properties is needed when discussing the bearing dynamics and lifetime. The properties are analysed using techniques which can be applied in most rotating machinery: measurement of the radial bearing displacement and the electrical resistance through the bearing. Exploring the possibilities to easily and accurately identify them is the second contribution of this work. The bearing motion, the behaviour of the lubricant film and cage slip are analysed for different operational conditions of the bearing. Clear trends w.r.t. the bearing load, temperature and speed are obtained. Clean analysis of the bearing motion and cage slip further proves precise operation of the test rig. The electrical resistance reveals the formation of the lubricant film during a run-up of the bearing speed. Estimation of the lubricant film thickness based on the electrical resistance is validated using an analytical model.

Accurate knowledge on the bearing dynamic properties is essential during the design of rotating machinery. They determine the machine's critical speeds, the forces acting on the different components, etc. This work investigates two dynamic properties of the test bearing: the radial stiffness and damping in the direction of the static load. Variation of the bearing temperature and speed reveals the influence of the lubricant film. During a warm-up of the bearing, the lubricant film thickness strongly decreases and the internal bearing clearance increases. The identified stiffness and damping consequently reduce. During a run-up of the speed, the electrical resistance through the bearing shows the formation of a lubricant film. In isothermal conditions, the stiffness and damping increase due to the formation of the lubricant film. In practice, a higher rotational speed of the bearing implies a higher operational temperature of the bearing components. The influence of the film formation is analysed for different speeds at a stable bearing temperature. A combined effect of both the temperature and speed is observed. Whether the lubricant film leads to an increase or decrease of the bearing stiffness is determined by the temperature conditions. In the literature, no experimental measurements showing the relations between the film formation and the dynamic properties are reported. Revealing these relations is the third contribution of the current study. The results help to evaluate the significance of modelling the lubricant film when numerically analysing the vibrations of a bearing system.

Precise prediction of the lifetime of rolling element bearings is a crucial step towards a reliable design of many rotating machines. For bearings subjected to highly varying loads, a strong reduction of the actual bearing lifetime w.r.t. the classically calculated bearing lifetime is observed. This work investigates the effect of external dynamic loads on the lubricant film formation and surface wear of the test bearing. When introducing a radial or axial excitation on the bearing, the lubricant film thickness follows the imposed variations of the load. Variations of the lubricant film thickness are similar to the variations when the magnitude of the static bearing load is changed. An increase of metallic contact or breakdown of the lubricant film is not detected. Under axial excitation, sliding motion between asperities of the contacting surfaces in the bearing does occur. Based on the temperature increase due to Coulomb friction between asperities, the optimal conditions for accelerated lifetime tests under high axial dynamic load are derived. Accelerated lifetime tests reveal polishing of the raceway honing structure. This polishing is clearly observed on SEM images of the inner raceway after a test duration of only 0.5% of the calculated L_{10} life. When the bearing is further exposed to the high axial dynamic load, polishing wear of the surfaces is expected. Analysis of the lubricant film behaviour under dynamic load is not described in the current literature and is considered to be the fourth contribution of this work. Also, the study promotes further research to analyse surface wear due to external dynamic loads.

7.2 Future perspectives

The presented test rig is a valuable tool for several studies. The main potential applications are:

- analysis of the lifetime and failure modes of rolling element bearings through lifetime tests;
- validation of algorithms for condition monitoring of rolling element bearings;
- characterisation of the bearing motion and slip behaviour of both healthy and aged rolling element bearings;
- analysis of the dynamic properties of rolling element bearings (radial and axial stiffness and damping characteristics);

- analysis of the formation and behaviour of the lubricant film inside rolling element bearings;
- validation of numerical models describing rolling element bearing behaviour (dynamic behaviour, bearing motion, bearing aging);
- validation of load identification techniques based on the known bearing load.

The modular mounting system allows analysis of a wide range of bearings and validation on a wide range of bearings. Furthermore, it allows adjustment of the fits applied between the inner ring and shaft and between the outer ring and housing. The operational conditions of the bearing (its rotational speed, radial and axial static load and radial and axial dynamic load) are also easily adjusted. The influence of the bearing type, the fits and/or the operational conditions can be investigated in each study.

The test rig allows applying a static and dynamic load in both the radial and axial bearing direction. The different loading conditions can be further extended. Misalignment of the test bearing is simulated when introducing a difference between the air pressure of both axial air springs. The resulting tilt angle is measured by the axial capacitive probes. An unbalance can be simulated when adding a third shaker, in the radial direction perpendicular to the current radial shaker. The third shaker is mounted below the test rig and its stinger is fitted through a hole in the frame.

As stated by different industrial partners, one particularly interesting application of the test rig is the validation of load identification techniques. Knowledge on the bearing load or detection of overloading during operation can significantly improve the evaluation of the bearing's remaining life. The load can be directly identified based on sensors (i.e. strain gauges) or indirectly estimated based on bearing responses (i.e. vibrations). In the current test rig, the actual static and dynamic bearing load are known such that the real and estimated load can be compared. Chapter 4 shortly reviews the potential to estimate the static bearing load based on the BPF, the amplitude of the BPF and the electrical resistance. More research on the applicability is required.

The current study shows the relations between the film formation and the bearing dynamic properties for the tested deep groove ball bearing. The results can be generalised by testing different types and sizes of rolling element bearings and different types of lubricants. Furthermore, numerical models describing the bearing dynamics can be validated using the obtained results. A first attempt was made by Fábio Nonato (University of Campinas, Brasil), who developed a model of the tested bearing. The model takes into account the EHL film using the properties of the base oil. A similar trend of the stiffness increase due to the film formation is proven. Full comparison of the experimental and numerical results is not possible, as the complex rheology of grease is not included in the model.

Advanced numerical bearing models take into account the behaviour of the lubricant film. Accurate identification of the film thickness allows further validation of the models. The behaviour of the lubricant film is analysed using the electrical resistance through the bearing. In isothermal conditions, variations of the lubricant film thickness are detected. Due to random metallic contact of asperities, the identification of thickness variations is hampered. Fluctuations of the lubricant's temperature further disturb the measurements. Load identification based on the electrical resistance is proven to be difficult. The R-C oscillation technique proposed by Zhang [81] allows identification of the film thickness at low levels of the film thickness parameter. This technique should be tested using the presented test rig.

Longer accelerated lifetime tests are required to analyse polishing wear due to external dynamic loads. Reduction of the lubricant film thickness also promotes mixed friction and surface wear. Controlling the film thickness is done using oil spray lubrication of the test bearing. XRD analysis allows objectifying the occurrence of polishing wear. Furthermore, the influence of an increased Hertzian pressure due to an additional radial dynamic load can be investigated.

The potential of the presented test rig to analyse the dynamic characteristics and lubricant film of a rolling element bearing under combined static and dynamic load is strongly emphasised in this manuscript. Several gaps in the current literature are filled. Nevertheless, it is clear that this study is just a start to many interesting and challenging future research tracks.

Appendix A

Specifications of the actuators and motor

Static load	
Air spring type	Sleeve
Air spring model	Contitech SZ 70-11
Regulator type	Electro-pneumatic
Regulator model	SMC ITV 2050-31f3n
Pressure range	0.005 to 0.9 MPa
Repeatability	-0.5% to 0.5% full span
Main line filter	SMC AFF 8C
Water separator	SMC AMG 350C

Dynamic load	
Shaker type	Electrodynamic
Shaker model	Modal Shop 2100E11
Amplifier model	QSC ISA750
Output force (sine peak)	0 to 220 N
Stroke length	25.4 mm
Frequency range	0 to 5400 Hz

Motor	
Drive model	Lenze E94 ASHE0244
Motor type	Synchronous servo
Motor model	MCS 19J30-RS0B0
Rated power	9.1 kW
Rated torque	29 Nm
Rated speed	3000 r/min
Encoder type	Resolver
Encoder resolution	0.8’
Encoder accuracy	-10’ to 10’

Appendix B

Specifications of the sensors

Accelerometers	
Type	ICP triaxial ceramic shear
Conditioner	PCB 442A104
Sensor	PCB 356A15
Sensitivity	100 mV/g
Measurement range	-50 to 50 g peak
Frequency range	2 to 5000 Hz

Load cells	
Type	ICP impedance head
Conditioner	PCB 442A104
Sensor	PCB 288D01
Sensitivity	22.4 mV/N
Measurement range	-222 to 222 N peak

Temperature probes	
Type	K-type thermocouple
Measurement range	-50 to 250 °C

Proximity probes	
Type	Capacitive
Drive	Lion Precision Elite CPL190-3-3
Probes	Lion Precision C23-B
Resolution	10 nm RMS
Sensitivity	40 mV/µm
Measurement range	250 to 750 µm
Frequency range	0 to 10000 Hz

Optical trigger	
Type	Diffuse proximity switch
Model	Omron EE-SY671
Detection type	Retro-reflective
Detection range	1 to 5 mm
Light source	Infrared LED

Appendix C

Specifications of the mechanical components

Bearing housing

Material	DIN 1.2311 prehardened mould steel
Material yield strength	821 MPa
Material ultimate tensile strength	1014 MPa
Mass	1.7 kg

Spindle shaft

Material	Chromium-nickel-molybdenum alloyed steel IMPAX P20
Material yield strength	800 MPa
Material ultimate tensile strength	1010 MPa
Mass	9.8 kg
Mass moment of inertia	0.0081 kgm^2

Spindle housing

Material	C45 steel
Material yield strength	310 MPa
Material ultimate tensile strength	565 MPa
Mass	15.9 kg

Frame	
Material	2011-T3 aluminium Alcoa
Material yield strength	262 MPa
Material ultimate tensile strength	310 MPa
Mass	320 kg

Bearings	
Type	SKF TRB T7FC 070
Contact angle	30 °
Fatigue load limit	27.5 kN
Static load rating	240 kN
Dynamic load rating	176 kN
Limiting speed	4500 r/min
Type	SKF TRB 31313 J2
Contact angle	30 °
Fatigue load limit	27.5 kN
Static load rating	228 kN
Dynamic load rating	194 kN
Limiting speed	4800 r/min

Bushings	
Type	Cylindrical type A 75/50
Compression stiffness	685000 N/m
Shear stiffness	95000 N/m
Maximum compression load	3065 N
Maximum shear load	1300 N

Coupling	
Type	Backlash-free jaw-type KTR ROTEX GS42
Spider	KTR 98 Sh A-GS
Torsional stiffness	21600 Nm/rad
Rated torque	450 Nm
Maximum torque	900 Nm
Mass	4.8 kg
Mass moment of inertia	0.0056 kgm^2

Appendix D

Properties of the test bearing

Bearing geometric data	
Bearing type	SKF DGBB 6302
Cage type	Pressed ribbon
Inner ring diameter	15 mm
Outer ring diameter	42 mm
Width	13 mm
Inner raceway diameter	20.762 mm
Outer raceway diameter	36.638 mm
Pitch diameter	28.7 mm
Rolling element diameter	7.938 mm
Inner raceway osculation	1.02
Outer raceway osculation	1.06
Number of elements	7

Lubricant data	
Type	SKF LGMT 2 All purpose / industrial
Base oil type	Mineral
Soap type	Lithium
NLGI consistency class	2
Base oil viscosity at 40 °C	110 mm^2/s

Mounting and clearance	
Fit at inner ring	j5
Fit at outer ring	H7
Inner ring temperature during operation	50 °C
Outer ring temperature during operation	40 °C
Radial clearance before mounting	3 to 18 µm
Radial clearance after mounting	0 to 18 µm
Radial clearance during operation	-4 to 14 µm

Loads and speeds	
Fatigue load limit	0.228 kN
Static load rating	5.4 kN
Dynamic load rating	11.9 kN
Limiting speed	24000 r/min

Appendix E

Kinematics of a single rolling element

The two-dimensional kinematics of a single rolling element are analysed in the moving coordinate system x′y′ of Fig. 4.17. The coordinate system is fixed to the cage. Slip occurring at the inner and outer ring is linked to both the angular velocity of the cage ω_c and the angular velocity of the rolling elements ω_r.

The grey arrows in Fig. 4.17 represent the velocity of the moving frame. The velocity is defined in three locations, the cage v_c, the inner ring contact v_{ci} and the outer ring contact v_{co}:

$$v_c = \omega_c \, \frac{d_m}{2} \tag{E.1}$$

$$v_{ci} = \omega_c \, \frac{d_m - D}{2} = \frac{v_c}{d_m} \, (d_m - D) \tag{E.2}$$

$$v_{co} = \omega_c \, \frac{d_m + D}{2} = \frac{v_c}{d_m} \, (d_m + D) \tag{E.3}$$

Considering a stationary outer ring, the absolute velocity of the outer ring contact v_o equals zero. The absolute velocity of the inner ring contact v_i equals:

$$v_i = \omega_i \, \frac{d_m - D}{2} \tag{E.4}$$

The relative velocity of the contact on the inner ring v'_i and outer ring v'_o is derived from the absolute velocity and moving frame velocity at both contacts. From Fig. 4.17, it is seen that:

$$\vec{v_i} = \vec{v'_i} + \vec{v_{ci}} \tag{E.5}$$

$$\vec{v_o} = \vec{v'_o} + \vec{v_{co}} \tag{E.6}$$

Projection on the y′-axis gives:

$$v'_i = v_i - v_{ci} \tag{E.7}$$

$$v'_o = v_o + v_{co} = v_{co} \tag{E.8}$$

Due to slip, the relative velocity of the rolling element at the inner ring contact v'_{ri} and the outer ring contact v'_{ro} deviates from respectively v'_i and v'_o. The slip in the contacts is defined as the difference between the relative velocity on the raceway and the rolling element. This slip at the inner and outer ring is always positive and given by:

$$s_i = v'_i - v'_{ri} \tag{E.9}$$

$$s_o = v'_o - v'_{ro} \tag{E.10}$$

The relation between v'_{ri} and v'_{ro} is used to derive the BPF when slip occurs:

$$\vec{v'_{ro}} + \vec{v'_{ri}} = 0 \tag{E.11}$$

Projection on the y′-axis gives:

$$v'_{ro} = v'_{ri} \tag{E.12}$$

Using Eq. E.7, E.8, E.9 and E.10:

$$v_{co} - s_o = v_i - v_{ci} - s_i \tag{E.13}$$

Using Eq. E.2 and E.3:

$$v_c \ \frac{d_m + D}{d_m} - s_o = v_i - v_c \ \frac{d_m - D}{d_m} - s_i \tag{E.14}$$

This equation is simplified to:

$$v_c = \frac{v_i}{2} + \frac{s_0 - s_i}{2} \tag{E.15}$$

Using Eq. E.1 and E.4:

$$\omega_c = \frac{\omega_i}{2} \ \frac{d_m - D}{d_m} + \frac{s_0 - s_i}{d_m} \tag{E.16}$$

The resulting expression for ω_c consists of two terms. The first term represents ω_c in the absence of slip, as derived in [46]. The second term represents the deviation of ω_c due to slip.

In the moving coordinate system x′y′, the following relations are fulfilled:

$$v_i' = (\omega_i - \omega_c) \ \frac{d_m - D}{2} \tag{E.17}$$

$$v_{ri}' = v_{ro}' = \omega_r \ \frac{D}{2} \tag{E.18}$$

These relations are used in Eq. E.9 to obtain an expression for ω_r:

$$\omega_r = (\omega_i - \omega_c) \ \frac{d_m - D}{D} - \frac{2 \ s_i}{D} \tag{E.19}$$

Using Eq. E.4 and E.16:

$$\omega_r = \frac{d_m \ \omega_i}{2 \ D} \left(1 - \left(\frac{D}{d_m} \right)^2 \right) - \left(\frac{s_o - s_i}{d_m} \ \frac{d_m - D}{D} + \frac{2 \ s_i}{D} \right) \tag{E.20}$$

The first term of this expression represents ω_r in the absence of slip, as derived in [46]. The second term represents the deviation of ω_r due to slip.

Bibliography

[1] Adams, V., and Askenazi, A. *Building better products with finite element analysis.* OnWord Press, 1999.

[2] Akturk, N., and Gohar, R. The effect of ball size variation on vibrations associated with ball-bearings. *Proceedings of the Institution of Mechanical Engineers, Part J: Journal of Engineering Tribology 212* (1998), 101–110.

[3] Akturk, N., Uneeb, M., and Gohar, R. The effects of number of balls and preload on vibrations associated with ball bearings. *Journal of Tribology 119* (1997), 747–753.

[4] Batrack, F., Kuhlmann, E., Lokar, A., Pohlman, C., and Wheeler, C. Test apparatus for determination of roller element bearing stiffness. In *Gearbox Reliability Collaborative* (November 2013).

[5] Bhushan, B. *Modern tribology handbook.* Taylor and Francis Group, 2010.

[6] Boness, R. Cage and roller slip in high-speed roller bearings. *Journal of Mechanical Engineering Science 11* (1969), 181–188.

[7] Brandlein, J., Eschmann, P., Hasbargen, L., and Weigand, K. *Ball and roller bearings: Theory, design and application.* Wiley, 1999.

[8] Brewe, D., and Hamrock, B. Simplified solution for elliptical-contact deformation between two elastic solids. *ASME Transactions Journal of Lubrication Technology 101*, 2 (1977), 231—-239.

[9] Cakmak, O., and Sanliturk, K. A dynamic model of an overhung rotor with deep-groove ball bearings. In *The First Joint International Conference on Multibody System Dynamics* (May 2010).

[10] Cameron, A., and Gohar, R. Theoretical and experimental studies of the oil film in lubricated point contacts. *Proceedings of the Royal Society A 291* (1966), 520–536.

[11] Cann, P. Starvation and reflow in a grease-lubricated elastohydrodynamic contact. *Tribology Transactions 39*, 3 (1996), 698–704.

[12] Cann, P. Starved grease lubrication in rolling contacts. *Tribology Transactions 42*, 4 (1999), 867–873.

[13] Cann, P. Thin-film grease lubrication. *Proceedings of the Institution of Mechanical Engineers Part J 213* (1999), 405–416.

[14] Castejón, C., Lara, O., and García-Prada, J. Automated diagnosis of rolling bearings using MRA and neural networks. *MSSP 24*, 1 (2010), 289–299.

[15] Christensen, H. The oil film in a closing gap. *Proceedings of the Royal Society: Series A 266* (1962).

[16] Ciulli, E., Stadler, K., and Draexl, T. The influence of the slide-to-roll ratio on the friction coefficient and film thickness of EHD point contacts under steady state and transient conditions. *Tribology International 42*, 4 (2009).

[17] Crook, A. The lubrication of rollers. *Philosophical Transactions of the Royal Society of London Series A 250* (1958).

[18] Dempsey, P., Certo, J., Handschuh, R., and Dimofte, F. Hybrid bearing prognostic test rig. *NASA/TM—2005-213597*, ARL–TR–3454 (2005).

[19] Dietl, P., Wensing, J., and van Nijen, G. Rolling bearing damping for dynamic analysis of multi-body systems: experimental and theoretical results. In *Proceedings of the Institution of Mechanical Engineers, Part K: Journal of Multi-body Dynamics* (June 2000).

[20] DIN. *DIN 623-1: Rolling bearings – fundamental principles, designation and marking.* DIN, Berlin, Germany, 1993.

[21] DIN. *DIN 69871-1: Tool shanks with 7/24 taper for automatic tool exchange.* DIN, Berlin, Germany, 1995.

[22] Dowson, D. Recent developments in studies of fluid film lubrication. In *Proceedings of the International Tribology Conference* (December 1987).

[23] Dowson, D., and Higginson, G. Theory of roller bearing lubrication and deformation. *Proceedings of the Institution of Mechanical Engineers 117* (1963), 216–222.

[24] Dowson, D., and Higginson, G. *Elasto-hydrodynamic lubrication.* Pergamon Press, 1977.

[25] Dyson, A., Naylor, H., and Wilson, A. The measurement of oil film thickness in elastohydrodynamic contacts. *Proceedings of the Institution of Mechanical Engineers 180* (1965), 119–134.

[26] Elsermans, M., Hongerloot, M., and Snoeys, R. Damping in taper roller bearings. In *MTDR Conference* (May 1976).

[27] Fujii, T., Ogata, M., and Shimotsuma, Y. Study on lubrication in a ball bearing. *Fluid Film Lubrication – Osborne Reynolds Centenary Proceedings of the 13th Leeds–Lyon Symposium on Tribology 11* (1987), 643–650.

[28] Gegner, J. Tribological aspects of rolling bearing failures. *Tribology - Lubricants and Lubrication Chapter 2* (2011), 33–94.

[29] Gegner, J., and Nierlich, W. Operational residual stress formation in vibration-loaded rolling contact. *Advances in X-ray Analysis 52* (2008), 722–731.

[30] Gegner, J., and Nierlich, W. Service loading analysis of wind turbine gearbox rolling bearings based on X-ray diffraction residual stress measurements. In *International Conference on Residual Stresses 9 (ICRS 9)* (November 2014).

[31] Gershuni, L., Larson, M., and Lugt, P. Lubricant replenishment in rolling bearing contacts. *Tribology Transactions 51* (2008).

[32] Gohar, R. *Elastohydrodynamics.* World Scientific, 1988.

[33] Grubin, A. *Fundamentals of the hydrodynamic theory of lubrication of heavily loaded cylindrical surfaces.* Central Scientific Institute for Technology and Mechanical Engineering, 1949.

[34] Gunduz, A., Dreyer, J., and Singh, R. Effect of bearing preloads on the modal characteristics of a shaft-bearing assembly: Experiments on double row angular contact ball bearings. *Mechanical Systems and Signal Processing 31* (2012).

[35] Gupta, P. Transient ball motion and skid in ball bearings. *ASME Journal of Lubrication Technology 97* (1975), 261–269.

[36] Gupta, P. Dynamics of rolling element bearings. I. Cylindrical roller bearing analysis. *ASME Journal of Lubrication Technology 101* (1979), 293–304.

[37] Gupta, P. Dynamics of rolling element bearings. II. Cylindrical roller bearing analysis. *ASME Journal of Lubrication Technology 101* (1979), 305–311.

[38] Gupta, P. Dynamics of rolling element bearings. III. Ball bearing analysis. *ASME Journal of Lubrication Technology 101* (1979), 312–318.

[39] Gupta, P. Dynamics of rolling element bearings. IV. Ball bearings results. *ASME Journal of Lubrication Technology 101* (1979), 319–326.

[40] Hamrock, B., and B.O., J. Elastohydrodynamic lubrication of line contacts. *Tribology Transactions 27* (1984), 275–287.

[41] Hamrock, B., and Dowson, D. Isothermal elastohydrodynamic lubrication of point contacts: Part III - Fully flooded results. *ASME Journal of Lubrication Technology 99*, 2 (1977).

[42] Hamrock, B., and Dowson, D. *Ball bearing lubrication.* Wiley, 1981.

[43] Harris, T. An analytical model to predict skidding in high speed roller bearings. *ASLE Transactions 9* (1966), 229–241.

[44] Harris, T. Analytical method to predict skidding in thrust-loaded, angular-contact ball bearings. *ASME Journal of Lubrication Technology 93* (1971), 17–24.

[45] Harris, T. Ball motion in thrust-loaded, angular-contact bearings with Coulomb friction. *ASME Journal of Lubrication Technology 93* (1971), 32–38.

[46] Harris, T. A., and Kotzalas, M. N. *Rolling bearing analysis.* Taylor and Francis Group, 2006.

[47] Hatch, C. Improved wind turbine condition monitoring using acceleration enveloping. *Orbit* (2004), 58–61.

[48] Heemskerk, R., Vermeiren, K., and Dolfsma, H. Measurement of lubrication condition in rolling element bearings. *ASLE Transactions 25*, 4 (1982), 519–527.

[49] Helsen, J., Vanhollebeke, F., Marrant, B., Berckmans, D., Vandepitte, D., and Desmet, W. Experimental assessment of gear meshing excitation propagation thoughout multi megawatt gearboxes. In *International Modal Analysis Conference* (January 2011).

[50] Heylen, W., Lammens, S., and Sas, P. *Modal analysis theory and testing.* KU Leuven, 2008.

[51] Hoagg, J., Lacy, S., Babuska, V., and Bernstein, D. Sequential multisine excitation signals for system identification of large space structures. In *American Control Conference* (July 2006).

[52] Holweger, W. Influence on bearing life by new material phenomena. In *NREL workshop* (November 2011).

[53] Hoshi, T. Damage monitoring of ball bearing. *Annals of the CIRP 55*, 1 (2006), 427–430.

[54] Inman, D., Farrar, C., Lopes, V., and Steffen, V. *Damage prognosis: for aerospace, civil and mechanical systems.* Wiley, 2005.

[55] ISO. *ISO 10816-3: Mechanical vibration – Evaluation of machine vibration by measurements on non-rotating parts.* ISO, Geneva, Switzerland, 1998.

[56] ISO. *ISO 281: Rolling bearings – Dynamic load ratings and rating life.* ISO, Geneva, Switzerland, 2007.

[57] Johnson, K., Greenwood, J., and Poon, S. A simple theory of asperity contact in elastohydrodynamic lubrication. *Journal of Wear 19* (1972), 91–108.

[58] Jones, A. Analysis of stresses and deflections. *New Departure Engineering Data 1* (1946), 12–22.

[59] Jorgensen, B., and Shin, Y. Dynamics of spindle-bearing systems at high speeds including cutting load effects. *Journal of Manufacturing Science and Engineering 120* (1998), 387–394.

[60] Kang, J., and Hadfield, M. Comparison of four-ball and five-ball rolling contact fatigue tests on lubricated Si3N4 steel contact. *Materials and Design 24*, 8 (2003), 595–604.

[61] Kawakita, K. The actual motion and the contact angle of a ball in a deep groove ball-bearing I: Shaft speed Ni = 100 rev/min; thrust load Fa = 0, 200 and 400 N. *Wear 95*, 3 (1984), 231–240.

[62] Kawakita, K., and Ariyoshi, S. The actual motion and the contact angle of a ball in a deep groove ball-bearing II: Shaft speed Ni = 100 rev/min; thrust load Fa = 600, 800 and 1000 N. *Wear 117*, 2 (1987), 251–262.

[63] Khonsari, M., and Booser, E. Proper film thickness key to bearing survival. *Machine Design* (2006).

[64] Kirk, A. Hydrodynamic lubrication of perspex. *Nature 194* (1962), 965–966.

[65] Kraus, J., Blech, J., and Braun, S. In situ determination of rolling bearing stiffness and damping by modal analysis. *Journal of Vibration, Acoustics, Stress and Reliability in Design 109* (1987).

[66] Kudish, I., and Covitch, M. *Modeling and analytical methods in tribology.* Chapman and Hall, CRC Press, 2010.

[67] Li, Y., Billington, S., Kurfess, C., Danyluk, T., and Liang, S. Adaptive prognostics for rolling element bearing condition. *MSSP 13*, 1 (1999), 103–113.

[68] Link, H., LaCava, W., van Dam, J., McNiff, B., Sheng, S., Wallen, R., McDade, M., Lambert, S., Butterfield, S., and Oyague, F. Gearbox reliability collaborative project report: findings from phase 1 and phase 2 testing. In *Technical Report NREL/TP-5000-51885* (November 2011).

[69] Lugt, P. A review on grease lubrication in rolling bearings. *Tribology Transactions 52* (2009).

[70] Magdun, O., and Binder, A. Calculation of roller and ball bearing capacitances and prediction of edm currents. In *Industrial Electronics IECON 09* (November 2009).

[71] Manoj, V., Manohar, K., and Gopinath, K. Developmental studies on rolling contact fatigue test rig. *Wear 264*, 7-8 (2008), 708–718.

[72] Marsh, E. *Precision spindle metrology.* DEStech Publications, 2008.

[73] Matharu, S., Sanyal, S., and Bal, D. Development of a multipurpose, effecient and inexpensive bearing test rig. *Journal of Engineering and Technology Research 2*, 3 (2010), 44–49.

[74] Meyer, D. R., and Wilson, C. C. Measurement of elastohydrodynamic oil-film thickness and wear in a ball bearing by the strain gauge method. *Journal of Lubrication Technology 93* (1971), 224–230.

[75] Mitsuya, Y., Sawai, H., Shimizu, M., and Aono, Y. Damping in vibration transfer through deep-groove ball bearings. *Journal of Tribology 120* (1998).

[76] Muro, H., and Tsushima, N. Microstructural, microhardness and residual stress changes due to rolling contact. *Journal of Wear 15* (1970), 309–330.

[77] Nierlich, W., and Gegner, J. Material response bearing testing under vibration loading. In *Bearing Steel: Advances in Rolling Contact Fatigue Strength Testing and Related Substitute Technologies* (November 2011).

[78] Nkuna, J., and Enslin, J. Self-organising feature maps for automated rolling element bearing vibration monitoring. In *The Seventh International Conference on Condition Monitoring and Machinery Failure Prevention Technologies* (June 2010).

[79] Nonato, F., and Cavalca, K. Investigation on the damping characteristics of elastohydrodynamic lubricated point contacts under dynamic loading. In *Proceedings of the 10th International Conference on Vibrations in Rotating Machinery* (September 2012).

[80] Nonato, F., and Cavalca, K. Local linear approximation for the stiffness characteristics of elastohydrodynamic point contacts. In *Proceedings of the 10th International Conference on Vibrations in Rotating Machinery* (September 2012).

[81] Peng-shun, Z., Shu-guang, L., and Wen-jie, Z. A new measurement method of oil film thickness in the EHL condition: the R-C oscillation technique. *Journal of Wear 148* (1991), 39–46.

[82] Pennacchi, P., Borghesani, P., Chatterton, S., and Ricci, R. An experimental based assessment of the deviation of the bearing characteristic frequencies. In *Proceedings of Surveillance 6* (October 2011).

[83] Perret, H. Die Lagerluft als Bestimmungsgröbe für die Beanspruchung eines Wälzlagers. *Werkstatt Betrieb 83* (1950), 131–134.

[84] Perret, H. Elastische Spielschwingungen konstant belasterer Wälzlager. *Werkstatt Betrieb 83* (1950), 354–358.

[85] Popa, L., Jensen, B., Ritchie, E., and Boldea, I. Condition monitoring of wind generators. In *Proceedings of the IAS Annual Meeting* (August 2003).

[86] Poplawski, J. Slip and cage forces in a high-speed roller bearing. *Journal of Tribology 94* (1972), 143–150.

[87] Prashad, H. *Tribology in electrical environments*. Elsevier, 2005.

[88] Randall, R. Detection and diagnosis of incipient bearing failure in helicopter gearboxes. *Engineering Failure Analysis 11*, 2 (2004), 177–190.

[89] Randall, R. B. *Vibration-based condition monitoring: Industrial, aerospace and automotive applications.* Wiley, 2011.

[90] Renaudin, L., Bonnardot, F., Musy, O., Doray, J., and Rémond, D. Natural roller bearing fault detection by angular measurement of true instantaneous angular speed. *MSSP 24*, 7 (2010), 1998–2011.

[91] Rico, J., Battez, A., and Cuervo, D. Rolling contact fatigue in lubricated contacts. *Tribology International 36*, 1 (2003), 35–40.

[92] Royston, T., and Basdogan, I. Vibration transmission through self-aligning (spherical) rolling element bearings: theory and experiment. *Journal of Sound and Vibration 215*, 5 (1998), 997–1014.

[93] Sarangi, M., Majumdar, B., and Sekhar, A. Stiffness and damping characteristics of lubricated ball bearings considering the surface roughness effect. Part 2: numerical results and applications. In *Proceedings of the Institution of Mechanical Engineers, Part J: Journal of Engineering Tribology* (May 2004).

[94] Sawalhi, N., and Randall, R. Simulating gear and bearing interactions in the presence of faults - Part I. The combined gear bearing dynamic model and the simulation of localised bearing faults. *MSSP 22*, 8 (2008), 1952–1966.

[95] Selvaraj, A., and Marappan, R. Experimental analysis of factors influencing the cage slip in cylindrical roller bearings. *The International Journal of Advanced Manufacturing Technology 53* (2011), 635–644.

[96] Sheng, S. Wind turbine micropitting workshop: a recap. In *Technical Report NREL/TP-500-46572* (February 2010).

[97] Sibley, L., and Austin, A. An X-Ray method for measuring thin lubricant films between rollers. *ISA Transactions 3* (1962), 237–243.

[98] Sibley, L., Bell, J., Orcutt, F., and Allen, C. A study of the influence of lubricant properties on the performance of aircraft gas engine rolling contact bearings. *WADD Technical Report* (1960), 60–189.

[99] SKF. *SKF general catalogue.* SKF Group, 2008.

[100] Smith, C. Some aspects of the performance of high-speed lightly-loaded cylindrical roller bearings. *Proceedings of the Institution of Mechanical Engineers 176* (1962), 566–601.

[101] So, B., and Klaus, E. Viscosity-pressure correlation of liquids. *ASLE Transactions 23* (1980).

[102] Sopanen, J., and Mikkola, A. Dynamic model of a deep-groove ball bearing including localized and distributed defects. Part 1: theory. *Proceedings of the Institution of Mechanical Engineers, Part K: Journal of Multi-body Dynamics 217*, 3 (2003), 201–211.

[103] Springer, C. The effects of internal geometry changes on the frequencies generated by deep groove ball bearings. *Tappi Journal 73*, 5 (1990), 101–105.

[104] Stachowiak, G. W., and Batchelor, A. *Engineering tribology.* Butterworth-Heinemann, 2005.

[105] Stacke, L.-E., Fritzson, D., and Nordling, P. BEAST - a rolling bearing simulation tool. *Proceedings of the Institution of Mechanical Engineers, Part K: Journal of Multi-body Dynamics 213* (1999), 63–71.

[106] Stadler, K., and Stubenrauch, A. Premature bearing failures in wind gearboxes and white etching cracks (WEC). *SKF Evolution* (2013).

[107] Stone, B. The state of the art in the measurement of the stiffness and damping of rolling element bearings. In *Annals of CIRP* (June 1982).

[108] Strackeljan, J., and Goreczka, S. Requirements for wheel bearing diagnostics. In *The Seventh International Conference on Condition Monitoring and Machinery Failure Prevention Technologies* (June 2010).

[109] Swahn, H., Becker, P., and Vingsbo, O. Martensite decay during rolling contact fatigue in ball bearings. *Metallurgical Transactions 7A* (1976), 1099–1110.

[110] Tandon, N., and Choudhury, A. A review of vibration and acoustic measurement methods for the detection of defects in rolling element bearings. *Tribology International 32* (1999), 469–480.

[111] Tao, B., Zhu, L., Ding, H., and Xiong, Y. An alternative time-domain index for condition monitoring of rolling element bearings - A comparison study. *Reliability Engineering and System Safety 92*, 5 (2007), 660–670.

[112] Tassone, B. Roller bearing slip and skidding damage. *Journal of Aircraft 12* (1975), 281–287.

[113] Totten, G., Westbrook, S., and Shah, R. *Fuels and lubricants handbook: Technology, properties, performance, and testing.* ASTM International, 2003.

[114] van Leeuwen, H. Discussion to the paper by L.B. Sargent on pressure-viscosity coefficients of liquid lubricants. *ASLE Transactions 26* (1983).

[115] Voskamp, A. Material response to rolling contact loading. *Journal of Tribology 107* (1985), 359–364.

[116] Walford, T., and Stone, B. The measurement of the radial stiffness of rolling element bearings under oscillating conditions. *JMES 22*, 4 (1980).

[117] Weck, M., and Ophey, L. Experimentelle Ermittlung der Dämfung Radial Belasteter Wälzlager. *Industrie Anzeiger 79*, 30.9.81/103 (1981).

[118] Wensing, J. *On the dynamics of ball bearings.* University of Twente, 1998.

[119] White, M. Rolling element bearing vibration characteristics: effect of stiffness. *Journal of Applied Mechanics 46* (1979), 677–684.

[120] Wijnant, Y. *Contact dynamics in the field of elastohydrodynamic lubrication.* University of Twente, 1998.

[121] Wijnant, Y., Wensing, J., and van Nijen, G. The influence of lubrication on the dynamic behaviour of ball bearings. *Journal of Sound and Vibration 222* (1999).

[122] Williams, J. *Engineering tribology.* Cambridge University Press, 2005.

[123] Wilson, J. S. *Sensor technology handbook.* Elsevier, 2005.

[124] Wood, R. Tribology and corrosion aspects of wind turbines. In *Wind Energy - Challenges for Materials, Mechanics and Surface Science* (October 2010).

[125] Worden, K., and Tomlinson, G. *Nonlinearity in structural dynamics: Detection, identification and modelling.* Institute of Physics Publishing, 2001.

[126] Zaretsky, E., Parker, R., and Anderson, W. NASA five-ball fatigue tester: Over 20 years of research. *ASTM special technical publication*, 771 (1982), 5–45.

[127] Zwirlein, O., and Schlicht, H. Werkstoffanstrengung bei Wälzbeanspruchung - Einfluss von Reibung und Eigenspannungen. *Werkstofftechnik 11* (1980), 1–14.

Curriculum Vitae

Personal data

- **Name:** William Jacobs
- **E-mail:** williamjacobs@skynet.be
- **Date of birth:** 3 March 1986
- **Place of birth:** Antwerp, Belgium

Professional Experience

- **2009 - 2014:** PhD research at KU Leuven
- **2008 - 2009:** Master thesis at Ford Lommel Proving Ground
- **Summer 2008:** Internship at FIZ BMW AG München

Education

- **2009 - 2014:** PhD researcher at the Department of Mechanical Engineering, KU Leuven
- **2007 - 2009:** Master in Mechanical Engineering - Vehicle technology, Graduated Magna cum laude, KU Leuven
- **2004 - 2007:** Bachelor in Electrical - Mechanical Engineering, Graduated Cum laude, KU Leuven

Publications

Articles in international journals

- Jacobs, W., Van Hooreweder, B., Boonen, R., Sas, P., and Moens, D., The influence of external dynamic loads on the lifetime of rolling element bearings: analysis of the lubricant film and surface wear. *Mechanical Systems and Signal Processing* (submitted).
- Jacobs, W., Boonen, R., Sas, P., and Moens, D., The influence of the lubricant film on the stiffness and damping characteristics of a deep groove ball bearing. *Mechanical Systems and Signal Processing 42 (1 - 2)* (2014), 335 - 350.

Articles in international conference proceedings

- Jacobs, W., Boonen, R., Sas, P., and Moens, D., The effect of external dynamic loads on the lifetime of rolling element bearings: SEM analysis of raceway surface wear. In *Proceedings of the International Conference on Noise and Vibration Engineering (ISMA2014 - USD2014)*, Leuven, Belgium, 15 - 17 September 2014.
- Jacobs, W., Boonen, R., Sas, P., and Moens, D., The effect of external dynamic loads on the lifetime of rolling element bearings: results of accelerated lifetime tests. In *Proceedings of the International Conference on Condition Monitoring and Machinery Failure Prevention Technologies (CM2014 - MFPT2014)*, Manchester, United Kingdom, 10 - 12 June 2014.
- Jacobs, W., Boonen, R., Sas, P., and Moens, D., Measuring the lubricant film behaviour of rolling element bearings under different operational conditions. In *Proceedings of the International Congress on Condition Monitoring and Diagnostic Engineering Management (COMADEM2013)*, Helsinki, Finland, 11 - 13 June 2013.

- Zhao, G., Jacobs, W., Depraetere, B., Alujevic, N., Pinte, G., and Sas, P., Modal analysis of a piezo based axisymmetric rotational vibration absorber. In *Proceedings of the International Operational Modal Analysis Conference (IOMAC2013)*, Guimarães, Portugal, 13 - 15 May 2013.
- Brandolisio, D., Jacobs, W., Devos, S., Desmet, W., and Moens, D., TPA for internal force identification in a mechanical system. In *Proceedings of the International Operational Modal Analysis Conference (IOMAC2013)*, Guimarães, Portugal, 13 - 15 May 2013.
- Jacobs, W., Boonen, R., Sas, P., and Moens, D., Estimating rolling element bearing stiffness under different operational conditions through modal analysis. In *Proceedings of the International Conference on Condition Monitoring of Machinery in Non-Stationary Operations (CMMNO2013)*, Ferrara, Italy, 8 - 10 May 2013.
- Jacobs, W., Boonen, R., Sas, P., and Moens, D., Measuring the rigid body behaviour of a deep groove ball bearing setup. In *Proceedings of the International Conference on Noise and Vibration Engineering (ISMA2012 - USD2012)*, Leuven, Belgium, 17 - 19 September 2012.
- Jacobs, W., Boonen, R., Sas, P., and Moens, D., The effect of external dynamic loads on the lifetime of rolling element bearings: experimental study. In *Proceedings of the International Conference on Experimental Mechanics (ICEM15)*, Porto, Portugal, 22 - 27 July 2012.
- Jacobs, W., Boonen, R., Sas, P., and Moens, D., The effect of external dynamic loads on the lifetime of rolling element bearings: accurate measurement of the bearing behaviour. In *Journal of Physics - Conference Series: International Congress on Condition Monitoring and Diagnostic Engineering Management (COMADEM2012)*, Huddersfield, United Kingdom, 18 - 20 June 2012.
- Jacobs, W., Malagó, M., Boonen, R., Moens, D., and Sas, P., Analysis of bearing damage using a multibody model and a test rig for validation purposes. In *International Workshop on Structural Health Monitoring (IWSHM2011)*, Stanford, USA, 13 - 15 September 2011.
- Malagó, M., Jacobs, W., Moens, D., and Sas, P., Multibody modelling of spalled rolling bearings: effectiveness of different contact algorithms. In *Proceedings of the ASME 2011 International Design Engineering Technical Conferences & Computers and Information in Engineering Conference: Multibody Systems, Nonlinear Dynamics and Control (IDETC CIE MSNDC)*, Washington D.C., USA, 28 - 31 August 2011.

- Jacobs, W., Malagó, M., Boonen, R., Sas, P., and Moens, D., Development of a test rig for multi-axial static and dynamic loading of bearings. In *Proceedings of the ASME 2011 International Design Engineering Technical Conferences & Computers and Information in Engineering Conference: Mechanical Vibration and Noise (IDETC CIE VIB)*, Washington D.C., USA, 28 - 31 August 2011.

Articles in national conference proceedings

- Jacobs, W., Brandolisio, D., Boonen, R., Sas, P., and Moens, D., Investigating the effect of external dynamic loads on the lifetime of rolling element bearings. In *National Congress on Theoretical and Applied Mechanics (NCTAM2012)*, Brussels, Belgium, 9 - 11 May 2012.

FACULTY OF ENGINEERING SCIENCE
DEPARTMENT OF MECHANICAL ENGINEERING
NOISE AND VIBRATION RESEARCH GROUP
Celestijnenlaan 300
B-3001 Heverlee
williamjacobs@skynet.be
http://www.mech.kuleuven.be